

THE EVOLUTION OF WATER IN CARBONACEOUS MAIN BELT ASTEROIDS

A DISSERTATION SUBMITTED TO THE GRADUATE DIVISION OF THE
UNIVERSITY OF HAWAII IN PARTIAL FULFILLMENT OF THE
REQUIREMENTS FOR THE DEGREE OF

DOCTOR OF PHILOSOPHY

IN

ASTRONOMY

July 2015

By

Heather Maria Kaluna

Dissertation Committee:

K. Meech, Chairperson

S. Bus

N. Haghighipour

D. Tholen

J. Gillis-Davis

We certify that we have read this dissertation and that, in our opinion, it is satisfactory in scope and quality as a dissertation for the degree of Doctor of Philosophy in Astronomy.

DISSERTATION COMMITTEE

Chairperson

© Copyright 2015
by
Heather M. Kaluna
All Rights Reserved

This work is dedicated to my father and mother, Clement Kahele Kaluna and Cathy Georgia Spirz Kaluna, you will be with me always.

Acknowledgements

First and foremost, I would like to extend a big mahalo to my mentors Henry Hsieh and Joseph Masiero. Without their guidance and listening to my many hours of scientific mumblings, I would never have formulated and developed the science topics that are the focus of this dissertation. The many impromptu conversations and the mana'o we have shared were so very critical to my development as a scientist.

I also wish to acknowledge my two advisors, Karen Meech and Jeffrey Gillis-Davis. Their training and expertise have been critical in developing the skills I needed to complete this dissertation. Karen has supported my graduate career from the very beginning and was amazingly patient with me as I struggled through some of life's hardest trials. For that, I will be forever grateful. I would also like to say a special mahalo to Jeffrey Gillis-Davis for welcoming the opportunity to work with me and taking me onto his space weathering team. It was through the work in his space weathering lab where I re-discovered my passion for science. In addition, I would also like to extend a very large mahalo to my committee members (current and past), Bobby Bus, Nader Haghighipour, David Tholen, Paul Lucey and Norbert Schorghofer. Each played an important role in the development and completion of this dissertation.

I want to also acknowledge the NASA Astrobiology faculty, postdocs and graduate students. Their diverse expertise has played a large role in shaping my scientific thinking and helping me to look at dissertation topic from a variety of perspectives. I would like to extend a special mahalo to Stephen Freeland, who has been such an inspiration in so many aspects, most especially in the realm of interdisciplinary science.

Next I would like to say thank you to the Institute for Astronomy faculty, staff, postdocs and graduate students. They have each supported me in various ways and without their various contributions, this work would not have been possible. A special thanks must be given to Mary Kadooka, for she is an amazing inspiration and has done so much to enrich the keiki of Hawai'i.

Most importantly, I want to say mahalo nui loa to my ohana for their amazing support of my graduate career. Their faith and love gave me the courage and strength to continue when times were hardest. Most especially, I want to acknowledge my ku'uipo Garvin Freitas and my dear brother and his beautiful family. I truly would not have made it this far without their unwaivering love and support.

Abstract

Astronomical signatures of water in the asteroid belt are found in the form of aqueously altered minerals and main-belt comets (MBCs). When paired with cosmochemical studies of meteorites, observations of aqueously altered minerals and MBCs may provide us with a way to constrain the availability of water during asteroid parent body accretion and thus constrain the position of the snow line in the early solar system. However, space weathering processes reduce our ability to accurately characterize asteroid compositions and match them with meteorite analogs. The goal of this dissertation is to study the role of water in space weathering processes, search for space weathering trends among C-complex asteroids, and characterize the mineralogy of two C-complex asteroid families.

We simulate micrometeorite bombardment of C-complex minerals through the laser irradiation of Mg and Fe-end member phyllosilicates. We find that the minerals lizardite and cronstedtite show both an increase and decrease in spectral slopes as a function of irradiation. However, the overall spectral trends of these two minerals are notably different, and space weathering trends may vary with the degree of aqueous alteration experienced by an asteroid parent body. Our data show that dehydration of hydrous minerals is not necessary for space weathering processes to be effective.

We conducted an extensive telescopic survey of the Beagle and Themis asteroid families, and obtained one of the most comprehensive visible and near-infrared data sets on these asteroids to date. Our data suggest space weathering of C-complex asteroids occurs primarily at visible wavelengths, and results in an increase in spectral slopes and a decrease in albedo with age.

Lastly, we explore the evolution of water ice in the main belt comet 133P/Elst-Pizarro. We use photometry data along with lightcurve inversion to constrain the pole orientation of 133P/Elst-Pizarro. We use the resulting obliquity ($\geq 75^\circ$) to model the evolution of subsurface ice for a variety of grain sizes and dynamical ages.

This dissertation utilizes the strength of observational, experimental, and model data to provide valuable insights on the thermal and aqueous evolution of carbonaceous main belt asteroids.

Table of Contents

Acknowledgements	v
Abstract	vii
List of Tables	xi
List of Figures	xiii
Chapter 1: Introduction	1
1.1 The Origin of Terrestrial Water	1
1.2 Dissertation Components	3
Chapter 2: Experimental Space Weathering of Fe and Mg-end Member Phyllosilicates	8
2.1 Introduction	8
2.2 Sample Preparation	11
2.3 Experimental Method	13
2.4 Spectral Analysis	14
2.5 Radiative Transfer Modeling	15
2.6 Results	18
2.6.1 Spectral Variation	18
2.6.2 Volatile Production	20
2.6.3 Radiative Transfer Models	21
2.7 Discussion	24
2.7.1 The Role of Water	24
2.7.2 Space Weathering Trends in Phyllosilicates	26

2.7.3	Space Weathering Trends in Meteorites	28
2.8	Summary	30
Chapter 3: Optical Space Weathering Trends Among Carbonaceous Asteroids		37
3.1	Introduction	37
3.2	Observations	38
3.3	Data Reduction and Analysis	39
3.4	Results	47
3.4.1	Spectral Slopes	48
3.4.2	Hydration Features	50
3.4.3	Albedo Variations	54
3.5	Discussion	57
3.5.1	C-type Space Weathering Trends	58
3.5.2	Regolith Effects on Spectral Characteristics	58
3.5.3	Aqueous Alteration in the Themis Parent Body	60
3.6	Summary	61
Chapter 4: Visible/Near-Infrared Color Trends in the Themis and Beagle Asteroid Families		66
4.1	Introduction	66
4.2	Observations	67
4.3	Data Reduction and Analysis	68
4.4	Results	70
4.4.1	Spectral Features	70
4.4.2	Color Trends	76
4.5	Discussion	79
4.5.1	NIR Space Weathering Trends of B-type Asteroids	79
4.5.2	Spectral Features of B-type Asteroids	80
4.5.3	Aqueous Alteration in the Beagle Parent Body	82
4.6	Summary	83

Chapter 5: The Spin Pole Orientation of the Main Belt Comet 133P/Elst-Pizarro . .	92
5.1 Introduction	92
5.2 Observations and Reductions	93
5.3 Analysis and Results	96
5.3.1 Lightcurve Inversion	96
5.3.2 Rotation Period	98
5.3.3 Pole Orientation	101
5.3.4 Model calculations of ice loss	104
5.3.5 Ice Depth in 133P/Elst-Pizarro	107
5.4 Discussion	111
5.4.1 Spin State of 133P/Elst-Pizarro	111
5.4.2 Water Ice in 133P/Elst-Pizarro	112
5.4.3 Detecting New MBCs	113
5.5 Summary	114
Chapter 6: Conclusion	119
6.1 Results from space weathering experiments	120
6.2 Results from visible and near-infrared observations	120
6.3 Results from photometric studies of the MBC 133P/Elst-Pizarro	122
6.4 Summary	122
Chapter 7: Future Work	127
7.1 Space Weathering Experiments	127
7.2 Observations	128
7.2.1 Spectral trends as function of diameter	128
7.2.2 Mineralogical maps of main belt asteroids	129
Appendix: Complete Set of Chapter 2 Figures and Tables	131

List of Tables

2.1	Aqueously Altered Carbonaceous Chondrite Compositions	10
2.2	Previously Published Space Weathering Experiments	10
2.3	Microprobe Analyses	12
2.4	Radiative Transfer Model Inputs	17
2.5	Summary of Model Results	22
3.1	Observing Geometry and Conditions: Themis Family Asteroids	40
3.1	Observing Geometry and Conditions: Themis Family Asteroids	41
3.2	Observing Geometry and Conditions: Beagle Family Asteroids	42
3.2	Observing Geometry and Conditions: Beagle Family Asteroids	43
3.3	Observing Geometry and Conditions: Veritas Family Asteroids	44
3.4	Spectral Characteristics: Themis Family Asteroids	51
3.5	Spectral Characteristics: Beagle Family Asteroids	52
3.6	Spectral Characteristics: Veritas Family Asteroids	53
3.7	Summary of Asteroid Family Slope and Albedo Distributions	54
4.1	IRTF Observations	84
4.1	IRTF Observations	85
4.2	IRTF Themis Asteroid Colors	86
4.3	IRTF Beagle Asteroid Colors	87
5.1	133P/Elst-Pizarro Observations and Geometry	94

5.2	Convexinv Input Parameters	97
5.3	Physical Characteristics as a Function of Observing Epochs	99
5.4	133P/Elst-Pizarro Rotation Periods from Period Scan	99
5.5	Thermal and Vapor Model Parameters	105
A.1	Spectral Slope Measurements	141
A.1	Spectral Slope Measurements	142
A.1	Spectral Slope Measurements	143
A.2	Spectral Reflectance Measurements	144
A.2	Spectral Reflectance Measurements	145
A.2	Spectral Reflectance Measurements	146
A.2	Spectral Reflectance Measurements	147
A.2	Spectral Reflectance Measurements	148
A.2	Spectral Reflectance Measurements	149
A.3	Spectral Band Depth Measurements	149
A.3	Spectral Band Depth Measurements	150
A.3	Spectral Band Depth Measurements	151

List of Figures

2.1	Olivine, lizardite and cronstedtite reflectance and normalized spectra as a function of irradiation time	16
2.2	Visible and NIR slope variations as a function of irradiation time	18
2.3	Visible and NIR reflectance variations as a function of irradiation time . . .	19
2.4	Band depth changes for olivine, lizardite and cronstedtite	20
2.5	Emitted H ₂ O gas measurements	21
2.6	Olivine radiative transfer models	23
2.7	Lizardite radiative transfer models	24
2.8	Cronstedtite radiative transfer models	25
2.9	Hapke absorption and scattering efficiencies	27
3.1	Continuum removed spectra of Themis asteroids	46
3.2	Continuum removed spectra of Themis and Beagle asteroids	47
3.3	Continuum removed spectra of Beagle and Veritas asteroids	48
3.4	Continuum removed spectra of Veritas asteroids	49
3.5	Spectral slope gradients for Themis and Beagle members	50
3.6	WISE albedo versus diameter distributions for Themis, Beagle and Veritas family asteroids	55
3.7	WISE albedo distributions for Beagle family asteroids	55
3.8	WISE albedo distributions for Themis family asteroids	56
3.9	WISE albedo distributions for Veritas family asteroids	56

3.10 Gaussian distributions of WISE albedos for Themis, Beagle and Veritas family asteroids	57
4.1 Themis 4-color spectra	71
4.2 Beagle 4-color spectra	72
4.3 Themis and Beagle PC1 vs PC2	74
4.4 Comparison of Themis and Beagle Colors	75
4.5 Themis and Beagle visible and NIR color comparison to solar system bodies	77
4.6 Themis and Beagle NIR color comparison to solar system bodies	78
4.7 Visible and NIR spectra of B-type asteroids from Clark et al. (2010) . . .	81
5.1 133P/Elst-Pizarro phased lightcurves	95
5.2 133P/Elst-Pizarro ecliptic longitude (λ_{ecl}) and ecliptic latitude (β_{ecl})	102
5.3 133P/Elst-Pizarro Shape Model	103
5.4 Depth to ice as a function of planetodetic latitude for 133P/Elst-Pizarro after 10 Myr	108
5.5 Surface temperature as a function of planetodetic latitude for 133P/Elst-Pizarro	109
5.6 Burial depth of ice as a function of time for 133P/Elst-Pizarro	109
5.7 Depth to ice as a function of planetodetic latitude for 133P/Elst-Pizarro after 2 Gyr	110
A.1 Olivine reflectance spectra and reflectance variations for each experiment .	132
A.2 Normalized olivine spectra and slope variations for each experiment	133
A.3 Continuum removed spectra of olivine and band depth variations for each experiment	134
A.4 Lizardite reflectance spectra and reflectance variations for each experiment	135
A.5 Normalized lizardite spectra and slope variations for each experiment	136
A.6 Continuum removed spectra of lizardite and band depth variations for each experiment	137

A.7 Cronstedtite reflectance spectra and reflectance variations for each experiment	138
A.8 Normalized cronstedtite spectra and slope variations for each experiment .	139
A.9 Continuum removed spectra of cronstedtite and band depth variations for each experiment	140

Chapter 1

Introduction

1.1 The Origin of Terrestrial Water

Perhaps the most important volatile in planetary and cosmochemistry studies is water due to its significant role in Jovian planet formation and its importance for life and habitability. The origin of terrestrial water is a key, unsolved issue in solar system studies, however, understanding the initial distribution and transport of volatiles in the early solar nebula can place significant constraints on the source of Earth's oceans.

Theoretical models of the position of the snow-line, the region beyond which volatiles condense, have placed it at distances of 1.6-1.8 AU (Lecar et al. 2006), implying Earth's volatiles were delivered exogenously. Aqueous alteration is the process that results in the production of secondary minerals (e.g. phyllosilicates, oxides) through reactions of primary minerals (e.g. olivine, pyroxene) with liquid water. The location of the carbonaceous C-complex asteroids, which are found in the asteroid belt and known to contain aqueously altered minerals (DeMeo & Carry 2014; Fornasier et al. 2014), provide evidence that the position of the snow line was located near 2.7 AU (Lecar et al. 2006). Morbidelli et al. (2000) use estimates of the water content in carbonaceous chondrite (CC) meteorites along with dynamical models to show that large planetary embryos from the outer asteroid belt likely played an important role in the delivery of volatiles to the terrestrial planets and the early proto-Earth. Indeed, D/H ratios in carbonaceous chondrite meteorites are found to

contain water with deuterium to hydrogen (D/H) ratios similar to that of Earth's oceans (Robert 2006, and references within).

However, the Grand Tack model suggests the carbonaceous C-complex asteroids, which are the predicted parent bodies of CC meteorites (Burbine et al. 2002), formed in the region between and beyond the Jovian planets (Walsh et al. 2011). Through dynamical models, Walsh et al. (2011) show that C-complex asteroids become implanted in the asteroids belt due to interactions with Jupiter as the planet migrates out to its current position. This model implies C-complex asteroids may come from a similar reservoir as comets. Supporting this hypothesis are recent measurements of the D/H ratios in the Jupiter-family comets 103P/Hartley 2 (Hartogh et al. 2011) and 45P/Honda-Mrkos-Pajdusakova (Lis et al. 2013), which show similar D/H ratios as CC meteorites and terrestrial water. However, most comets have higher D/H ratios (e.g. Eberhardt et al. 1995; Meier et al. 1998), thus it is unclear whether C-complex asteroids formed beyond Jupiter or in-situ within the asteroid belt.

The Grand Tack model predicts that C-complex objects should still be located in the regions between the Jovians (e.g. among the Trojan asteroids) as well as further out in the Kuiper belt (Walsh et al. 2011). Large heliocentric and geocentric distances and small sizes can make it difficult to obtain high signal to noise ratio spectra of outer solar system objects, but improvements in astronomical instrumentation have led to increased and refined observations of these small bodies. While there have been a few detections of Centaurs and Trans-Neptunian objects (TNOs) with spectral features similar to those observed on C-complex asteroids (Lazzarin et al. 2003; Fornasier et al. 2009; de Bergh et al. 2004; Alvarez-Candal et al. 2008), most small, outer solar system bodies lack the spectral features commonly seen in C-complex asteroids (Fornasier et al. 2014).

Further studies are needed of C-complex asteroids and outer solar system bodies to improve our understanding of the relationship between these two populations and further constrain models (e.g. Grand Tack) that describe the initial distribution and transport of

volatiles in the solar system. For this dissertation, we have chosen to focus on developing a comprehensive study of the C-complex asteroids.

1.2 Dissertation Components

Perhaps one of the best tools for assessing C-complex asteroid compositions derives from linking their spectra with CC meteorite spectra, for which detailed chemical and petrographic studies have been conducted. Several CC meteorite subgroups (e.g. CI, CM and CR) contain aqueously altered minerals, such as phyllosilicates, magnetite, and tochilinite (Rubin 1997; Burbine et al. 2002; Weisberg et al. 2006), that broadly match the absorption features seen in C-complex asteroid spectra (Gaffey & McCord 1978; Burbine 1998; Hiroi et al. 1996). While the absorption features of C-complex asteroids can be matched to minerals in CC meteorites, space weathering processes, which modify an airless bodies surface with time and induce spectral variations, introduces significant uncertainties in linking meteorites directly with asteroid parent bodies (Chapman 2004).

At present, the number of space weathering experiments on aqueously altered CC meteorites and minerals is relatively small when compared to the large diversity of CC meteorites (Burbine et al. 2002). In Chapter 2, we explore the effects of laser irradiation experiments on phyllosilicates to study the effects of space weathering on one of the major minerals found in CI and CM meteorites (Cloutis et al. 2011b,a).

In Chapters 3 and 4, we use visible and near-infrared data to study the albedo and spectral trends of the C-complex Themis and Beagle asteroid families. These two asteroid families originated from the same parent body, thus provide a unique tool to resolve contrasting space weathering trends observed in the C-complex asteroids (Nesvorný et al. 2005; Lazzarin et al. 2006).

In addition to aqueously altered minerals, direct observations of water ice (Rivkin & Emery 2010) and the discovery of a new class of objects called the ‘active asteroids’ (Boehnhardt et al. 1996; Hsieh et al. 2006; Jewitt 2012) suggest water ice is still present in

the asteroid belt. In Chapter 5, we use photometric data and lightcurve inversion to study the physical characteristics of the main belt comet 133P/Elst-Pizarro to assess the ability of small bodies to retain buried water ice over the age of the solar system. In Chapter 6, we evaluate and synthesize the experimental, observational and thermal results presented in this dissertation to provide a comprehensive view of the evolution of water in carbonaceous main belt asteroids.

References

- Alvarez-Candal, A., Fornasier, S., Barucci, M. A., de Bergh, C., & Merlin, F. 2008, *A&A*, 487, 741
- Boehnhardt, H., Schulz, R., Tozzi, G. P., Rauer, H., & Sekanina, Z. 1996, *IAU Circ.*, 6495, 2
- Burbine, T. H. 1998, *Meteoritics and Planetary Science*, 33, 253
- Burbine, T. H., McCoy, T. J., Meibom, A., Gladman, B., & Keil, K. 2002, *Asteroids III*, 653
- Chapman, C. R. 2004, *Annual Review of Earth and Planetary Sciences*, 32, 539
- Cloutis, E. A., Hiroi, T., Gaffey, M. J., Alexander, C. M. O. ., & Mann, P. 2011a, *Icarus*, 212, 180
- Cloutis, E. A., Hudon, P., Hiroi, T., Gaffey, M. J., & Mann, P. 2011b, *Icarus*, 216, 309
- de Bergh, C., Boehnhardt, H., Barucci, M. A., Lazzarin, M., Fornasier, S., Romon-Martin, J., Tozzi, G. P., Doressoundiram, A., & Dotto, E. 2004, *A&A*, 416, 791
- DeMeo, F. E. & Carry, B. 2014, *Nature*, 505, 629
- Eberhardt, P., Reber, M., Krankowsky, D., & Hodges, R. R. 1995, *A&A*, 302, 301

- Fornasier, S., Barucci, M. A., de Bergh, C., Alvarez-Candal, A., DeMeo, F., Merlin, F., Perna, D., Guilbert, A., Delsanti, A., Dotto, E., & Doressoundiram, A. 2009, *A&A*, 508, 457
- Fornasier, S., Lantz, C., Barucci, M. A., & Lazzarin, M. 2014, *Icarus*, 233, 163
- Gaffey, M. J. & McCord, T. B. 1978, *Space Sci. Rev.*, 21, 555
- Hartogh, P., Lis, D. C., Bockelée-Morvan, D., de Val-Borro, M., Biver, N., Küppers, M., Emprechtinger, M., Bergin, E. A., Crovisier, J., Rengel, M., Moreno, R., Szutowicz, S., & Blake, G. A. 2011, *Nature*, 478, 218
- Hiroi, T., Zolensky, M. E., Pieters, C. M., & Lipschutz, M. E. 1996, *Meteoritics and Planetary Science*, 31, 321
- Hsieh, H. H., Jewitt, D., & Pittichova, J. 2006, *IAU Circ.*, 8704, 3
- Jewitt, D. 2012, *AJ*, 143, 66
- Lazzarin, M., Barucci, M. A., Boehnhardt, H., Tozzi, G. P., de Bergh, C., & Dotto, E. 2003, *AJ*, 125, 1554
- Lazzarin, M., Marchi, S., Moroz, L. V., Brunetto, R., Magrin, S., Paolicchi, P., & Strazzulla, G. 2006, *ApJ*, 647, L179
- Lecar, M., Podolak, M., Sasselov, D., & Chiang, E. 2006, *ApJ*, 640, 1115
- Lis, D. C., Biver, N., Bockelée-Morvan, D., Hartogh, P., Bergin, E. A., Blake, G. A., Crovisier, J., de Val-Borro, M., Jehin, E., Küppers, M., Manfroid, J., Moreno, R., Rengel, M., & Szutowicz, S. 2013, *ApJ*, 774, L3
- Meier, R., Owen, T. C., Jewitt, D. C., Matthews, H. E., Senay, M., Biver, N., Bockelée-Morvan, D., Crovisier, J., & Gautier, D. 1998, *Science*, 279, 1707
- Morbidelli, A., Chambers, J., Lunine, J. I., Petit, J. M., Robert, F., Valsecchi, G. B., & Cyr, K. E. 2000, *Meteoritics and Planetary Science*, 35, 1309

- Nesvorný, D., Jedicke, R., Whiteley, R. J., & Ivezić, Ž. 2005, *Icarus*, 173, 132
- Rivkin, A. S. & Emery, J. P. 2010, *Nature*, 464, 1322
- Robert, F. 2006, Solar System Deuterium/Hydrogen Ratio, ed. D. S. Lauretta & H. Y. McSween, 341–351
- Rubin, A. E. 1997, *Meteoritics and Planetary Science*, 32, 231
- Walsh, K. J., Morbidelli, A., Raymond, S. N., O’Brien, D. P., & Mandell, A. M. 2011, *Nature*, 475, 206
- Weisberg, M. K., McCoy, T. J., & Krot, A. N. 2006, Systematics and Evaluation of Meteorite Classification, ed. D. S. Lauretta & H. Y. McSween, 19–52

Chapter 2

Experimental Space Weathering of Fe and Mg-end Member Phyllosilicates

2.1 Introduction

Space weathering, which is a process that alters the surfaces of airless bodies exposed to the space environment, is known to redden, obscure band depths and darken the spectra of lunar soils (Fischer et al. 1994). The spectral changes result from the production of agglutinates, small glassy aggregates (McKay et al. 1991), and the vapor deposition of nanophase metallic iron (npFe^0) particles onto lunar grains during micrometeorite impacts and solar wind sputtering (Conel & Nash 1970; Keller & McKay 1993). The vapor deposition model models the effects of npFe^0 particles on the optical properties of lunar soils (Hapke 1973; Hapke et al. 1975; Cassidy & Hapke 1975; Hapke 2001). However, vapor deposition alone cannot account for the spectral differences seen between lunar soils and freshly ground lunar rocks (Gold et al. 1970; Hapke et al. 1970), and a contribution from agglutinates in addition to npFe^0 particles is necessary to resolve the mismatch. (Keller et al. 1998) found that while nanophase particles produce significant reddening and darkening, the larger iron particles found in agglutinate glass (James et al. 2001) result in darkening without reddening. The lunar samples demonstrate the importance of particle size on the wavelength dependence of the optical characteristics of space weathered soils.

The silicate rich S-complex asteroids, which are dominated by olivine and pyroxene, also experience optical changes in response to space weathering (Jedicke et al. 2004; Nesvorný et al. 2005). However, optical trends in S-complex asteroids suggests that space weathering processes are different for asteroids than those occurring on the Moon. For instance, visible albedos of the young Karin and old Koronis asteroid families do not show a reduction in albedo with age (Masiero et al. 2011). Furthermore, spacecraft data of the S-complex asteroids Eros and Ida imply reddening and darkening occur sequentially rather than simultaneously (Chapman 2004).

The first study to show space weathering on C-complex asteroids used photometric colors of asteroid families from the Sloan Digital Sky Survey (SDSS). Nesvorný et al. (2005) performed principal component analyses on the SDSS data and found correlations in the color trends and ages of asteroid families. Unlike S-complex asteroids, they found that C-complex asteroids experience a decrease in spectral slopes with age. A subsequent survey by Lazzarin et al. (2006) investigated C-complex asteroids independent of family association using spectroscopic data from the Small Main-Belt Asteroid Spectroscopic Survey (SMASS II; Bus & Binzel 2002). In contrast to Nesvorný et al. (2005), they found the spectral slopes become redder with age. However, when they repeated their analyses on the same asteroids used in Nesvorný et al. (2005), they found the spectra become bluer with age. C-complex asteroids have been proposed as the parent bodies of CC meteorites (Hiroi et al. 1996; Burbine 1998; Burbine et al. 2001; Cloutis et al. 2011a), which show a wide range of compositions (Table 2.1). Thus, Lazzarin et al. (2006) attributed the Nesvorný et al. (2005) decrease in spectral slopes to sampling effects that reflect mineralogical differences rather than space weathering trends.

Table 2.2 shows previously published spectral trends resulting from simulated space weathering experiments on C-complex asteroid analog materials and carbonaceous chondrites. Experiments on CC simulants, Tagish Lake (C2 ungrouped) and complex organics result in a decrease of spectral slopes (Hiroi et al. 2003, 2004; Moroz et al. 2004a). Other experiments on Allende (CV3), Mighei (CM2), and FM 95002 (CO3) result in an

Table 2.1. Aqueously Altered Carbonaceous Chondrite Compositions

Group or Subtype	Petrologic Grade	Mineralogy	Proposed Asteroid Parent Class
CI	1.0	serpentine, magnetite, oxides, sulfides, olivine	B (Cloutis et al. 2011a)
CM	1.0-2.0	cronstedtite, serpentine, olivine, pyroxene, sulfides, calcite, magnetite	G,C (Burbine 1998)
CR	1.0-2.0	olivine, pyroxene, plagioclase, serpentine, Fe-Ni metal, sulfides	C (Hiroi et al. 1996)
CV	3.0	olivine, pyroxene, sulfides, Fe-Ni metal, feldspar, magnetite, serpentine	K (Burbine et al. 2001)
CO	3.0-3.6	olivine, pyroxene, Fe-Ni metal, oxides magnetite, sulfides, serpentine	K (Burbine et al. 2001)

Note. — Petrological grade ranges from 0 (high degree of aqueous alteration) to 3.0 (little to no aqueous alteration) and are tabulated from Beck et al. (2014). CM, CI and CV mineralogies represent the modal mineralogy of a type specimen for those meteorite groups: Murchison (M), Orgueil (I), and Vigarano (V) (Cloutis et al. 2011b; Bland et al. 2004; Cloutis et al. 2012b). CR and CO mineralogy reflects several meteorite compositions within those classes (Buseck & Hua 1993).

Table 2.2. Previously Published Space Weathering Experiments

Meteorite	Petrologic Grade	Slope Changes	Albedo Changes	Method	Reference
Mighei (CM)	2.3 [†]	Increase	Increase	Laser	Moroz et al. (2004b)
Murray (CM)	2.5	—	Increase	H ⁺ Ion	Hapke (1966)
Tagish Lake (C)	2.0	Decrease	Increase	Laser	Hiroi et al. (2004)
Tagish Lake	2.0	Increase	Increase	He ⁺ Ion	Vernazza et al. (2013)
Tagish Lake	2.0	Decrease	Increase	Ar ⁺ Ion	Vernazza et al. (2013)
CM simulant	—	Decrease	Decrease	Laser	Hiroi et al. (2003)
Organics	—	Decrease	Increase	He ⁺ Ion	Moroz et al. (2004a)
Organics	—	Decrease	Increase	N ⁺ Ion	Moroz et al. (2004a)

Note. — [†] Petrologic grade derived by Rubin (2007).

increase of spectral slopes (Moroz et al. 1996, 2004b; Shingareva et al. 2004; Lazzarin et al. 2006; Gillis-Davis et al. submitted). It is clear from both experimental data and observational data that space weathering trends of carbonaceous materials are both variable and inconsistent.

We propose the complex compositions of CCs require systematic experiments and observations to understand the complicated response of carbonaceous material to space weathering. In this thesis, we aim to resolve some of the discrepancies in previous space weathering experiments by performing laser irradiation on end-member phyllosilicates. Phyllosilicates, which form by reactions between silicate minerals and water and have H_2O or OH incorporated into their crystal structure, are a group of minerals abundant in CI and CM meteorites (e.g. Cloutis et al. 2011a; Rubin 2007) and C-complex asteroids (Fornasier et al. 2014). This study uses pulsed laser irradiation to simulate micrometeorite bombardment of a Mg-rich phyllosilicate, lizardite ($\text{Mg}_3(\text{Si}_2\text{O}_5)(\text{OH})_4$), and an Fe-rich sample dominated by the phyllosilicate cronstedtite ($\text{Fe}_2^{2+}\text{Fe}^{3+}(\text{SiFe}^{3+})\text{O}_5(\text{OH})_4$, the full composition is described in § 2.2). Our aim is to characterize the spectral differences between phyllosilicates and anhydrous silicates in response to simulated space weathering, thus we also simulated micrometeorite bombardment of an anhydrous silicate, San Carlos olivine ($(\text{Mg,Fe})_2\text{SiO}_4$).

2.2 Sample Preparation

The lizardite sample originated from the San Benito Co., California locality and occurred as sheets that were partially covered with artinite ($\text{Mg}_2(\text{CO}_3)(\text{OH})_2\cdot 3(\text{H}_2\text{O})$) needles. The sample was concentrated by using tweezers to remove the needles from between layers of lizardite. The cronstedtite sample originated from the Kisbanya, Romania, locality and occurred as crystal growths on a basalt-like host rock. We used a diamond-tipped Dremel tool to remove as much of the host rock without disrupting the cronstedtite crystals. The San Carlos olivine required no modification prior to grinding. The suite of instruments

Table 2.3. Microprobe Analyses

Oxide (wt. %)	Lizardite	Cronstedtite	Olivine
SiO ₂	39.34	17.38	41.13
TiO ₂	0.03	0.00	0.00
Al ₂ O ₃	0.28	0.01	0.03
Cr ₂ O ₃	0.15	0.00	0.01
FeO [†]	1.68	76.32	9.51
MnO	0.04	0.00	0.14
MgO	39.71	0.00	49.26
CaO	0.00	0.00	0.09
NiO	0.00	0.00	0.36
H ₂ O [‡]	12.91	9.79	0.00

Note. — Fractional abundances determined from electron microprobe analyses of the minerals used in this work.

[†]Cronstedtite measurement reflects Fe₂O₃. [‡] H₂O fraction determined from stoichiometry.

used for the sample preparation and irradiation experiments are located at the University of Hawai'i at Mānoa.

We assayed the mineralogy of the cronstedtite and concentrated lizardite using a compact and portable X-ray diffraction / X-ray fluorescence (XRD/XRF) instrument from InXitu Inc. This instrument does not require large or finely powdered samples for quality diffraction patterns (Sarrazin et al. 2005). The XRD analyses showed the lizardite sample was 95% pure and the cronstedtite sample was composed of ~73 wt.% cronstedtite, 23 wt.% pyrite (FeS₂) and 3 wt.% siderite (FeCO₃). Siderite, an Fe-carbonate, and pyrite, an Fe-sulfide, are also formed during aqueous alteration.

The chemical compositions of each mineral were derived using electron microprobe analyses and are presented in Table 2.3. The electron microprobe is a JEOL JXA-8500F field-emission gun microanalyzer with 5 wavelength-dispersive spectrometers. A beam current of 5.0 nA for cronstedtite and 4.0 nA for lizardite was used with a spot size of 10 μ m for both minerals.

Each mineral was crushed into a powder using a mortar and pestle, and then dry-sieved into two size fractions, greater and less than $75\ \mu\text{m}$. Our experiments used ~ 0.5 gram of each mineral from the $<75\ \mu\text{m}$ size fraction. The smaller size fraction was chosen to match the particle size used in Sasaki et al. (2001, 2003).

2.3 Experimental Method

Spectral data were taken using a visible and near-infrared wavelength ($0.35\text{--}2.5\ \mu\text{m}$) Analytical Spectral Devices Inc. FieldSpec 4 Spectroradiometer, with a resolution, given as full-width half-maximum, of 3 nm at $.35\text{--}1.0\ \mu\text{m}$ and 10 nm at $1.0\text{--}2.5\ \mu\text{m}$. Reflectance spectra were taken at incidence and emission angles of $i=30^\circ$ and $e=0^\circ$, respectively, and measured relative to a 99% reflectance LabSphere Spectralon Standard. For our spectral measurements, each sample was placed in a sample holder and the surface was leveled by moving a flat spatula across the holder surface, taking care not to compress the sample. Four spectra were taken and then the sample was removed, mixed and placed back into the holder. This sequence was repeated twice for each imaging series, resulting in 12 spectra that account for packing effects during placement into the holder.

The uncompressed samples were put into a glass beaker and irradiated in a chamber at vacuum pressures of 10^{-5} to 10^{-6} mbar. A Continuum Surelite-I-20 Nd:YAG 1064 nm pulsed laser with a 20 Hz frequency and 6-8 nanosecond duration was used to irradiate the samples. The pulse duration simulates the timescale of micrometeorite dust impacts (Yamada et al. 1999). The incident laser energy of 30mJ was chosen to replicate the energies used in Sasaki et al. (2001, 2003), which simulate $1\ \mu\text{m}$ dust impacts at 1 AU. Sasaki et al. (2001) use the flux of impacts at 1 AU and an impact velocity of $20\ \text{km s}^{-1}$ (to reach vaporization energies) to equate 30mJ to $\sim 10^8$ years of space weathering. The laser was focused to a spot size of $\sim 250\ \mu\text{m}$ and the position was manually adjusted to irradiate the full area of the sample. The lizardite and olivine samples were irradiated at intervals of 2.5, 2.5, 5.0, 5.0, 5.0, 10.0, 10.0, 10.0 and 10.0 minutes for a total of 60 minutes. The

irradiation intervals for cronstedtite were the same as for olivine and lizardite, but the total time was limited to 40 minutes due to the significant fraction of lost sample during irradiation. A Stanford Research System 100 amu Residual Gas Analyzer (RGA), which is a quadrupole mass spectrometer, was used to measure water, hydrogen and other volatiles released during each irradiation. The chamber was returned to atmospheric pressure after each irradiation and spectra were taken outside of the chamber for spectral imaging. Three experiments were conducted on each mineral to ensure the spectral trends were repeatable across multiple experiments.

2.4 Spectral Analysis

Visible and near-infrared (NIR) continuum points that lie outside absorption bands were used to compare variations in reflectance (our proxy for albedo). Due to the difference in absorption band positions and width, the continuum points used to measure albedo were different values for each mineral. The visible wavelength reflectance changes were measured using the reflectance values at continuum points of $0.70\ \mu\text{m}$ for olivine, $0.57\ \mu\text{m}$ for lizardite, and $0.60\ \mu\text{m}$ for cronstedtite. The NIR reflectance changes were measured using reflectance values at continuum points of $2.16\ \mu\text{m}$ for lizardite, $2.20\ \mu\text{m}$ for cronstedtite and $2.30\ \mu\text{m}$ for olivine.

Continuum removal was used to quantify the changes in band depths for each mineral. The continuum was removed by fitting a line to continuum points surrounding the 1.05 , 1.13 , and $1.5\ \mu\text{m}$ bands for olivine, lizardite and cronstedtite, respectively. Specifically, continuum points at $0.70\ \mu\text{m}$ and $1.60\ \mu\text{m}$ were used for olivine, $0.57\ \mu\text{m}$ and $1.70\ \mu\text{m}$ were used for lizardite, and $0.60\ \mu\text{m}$ and $2.20\ \mu\text{m}$ were used for cronstedtite. The original reflectance spectrum was divided by the linear fit and the band depths were computed by subtracting the minimum reflectance value from the continuum value (i.e. $1 - \text{minimum value}$, Clark & Roush (1984)). We divided all slope, albedo and band depth measurements

in a single experiment by the corresponding values derived from the fresh spectrum. This allowed us to compare the relative spectral changes for each of the minerals.

Spectral slopes were computed using a linear fit to continuum regions that lay outside of absorption bands after normalizing the spectra to 0.55 μm . Normalization was performed to isolate slope variations from albedo differences between the minerals. Due to the different continuum regions, the slopes were measured using different values for each mineral. The visible/NIR slopes for olivine were fit using two points at 0.70 μm and 1.60 μm . The NIR slopes were measured using values at 1.60 μm and 2.30 μm . Lizardite visible/NIR slopes were measured using continuum points at 0.57 μm and 1.70 μm , and NIR slopes were measured using 1.70 μm and 2.16 μm . Visible slopes for cronstedtite were measured using points at 0.60 μm and 0.75 μm , and NIR slopes using 0.75 μm and 2.20 μm . Reflectance and normalized spectra are presented in Figure 2.1.

2.5 Radiative Transfer Modeling

Hapke (2001) developed a radiative transfer model to represent the optical properties of npFe⁰ particles in the rims of lunar grains. In particular Hapke (2001) used Maxwell-Garnet theory (an equivalent to Rayleigh scattering theory) to relate the optical reddening and darkening of space weathered lunar grains to single scattering albedo through Equation 2.1.

$$w = S_E + \frac{(1 - S_E)(1 - S_l)e^{-(\alpha_h + \alpha_g + \alpha_c)D}}{1 - S_l e^{-(\alpha_h + \alpha_g + \alpha_c)D}} \quad (2.1)$$

where w is the single scattering albedo; α the absorption for the coefficient for the host material (h), the iron particles within grains (g), and the coating of iron particles on the grains (c), respectively; D the particle diameter, S_l and S_E the internal and external surface reflectance, respectively (Hapke 1981, 1993, 2001). The absorption coefficients (α) of the host material as well as the metallic iron depend on n and k , the real and imaginary indices

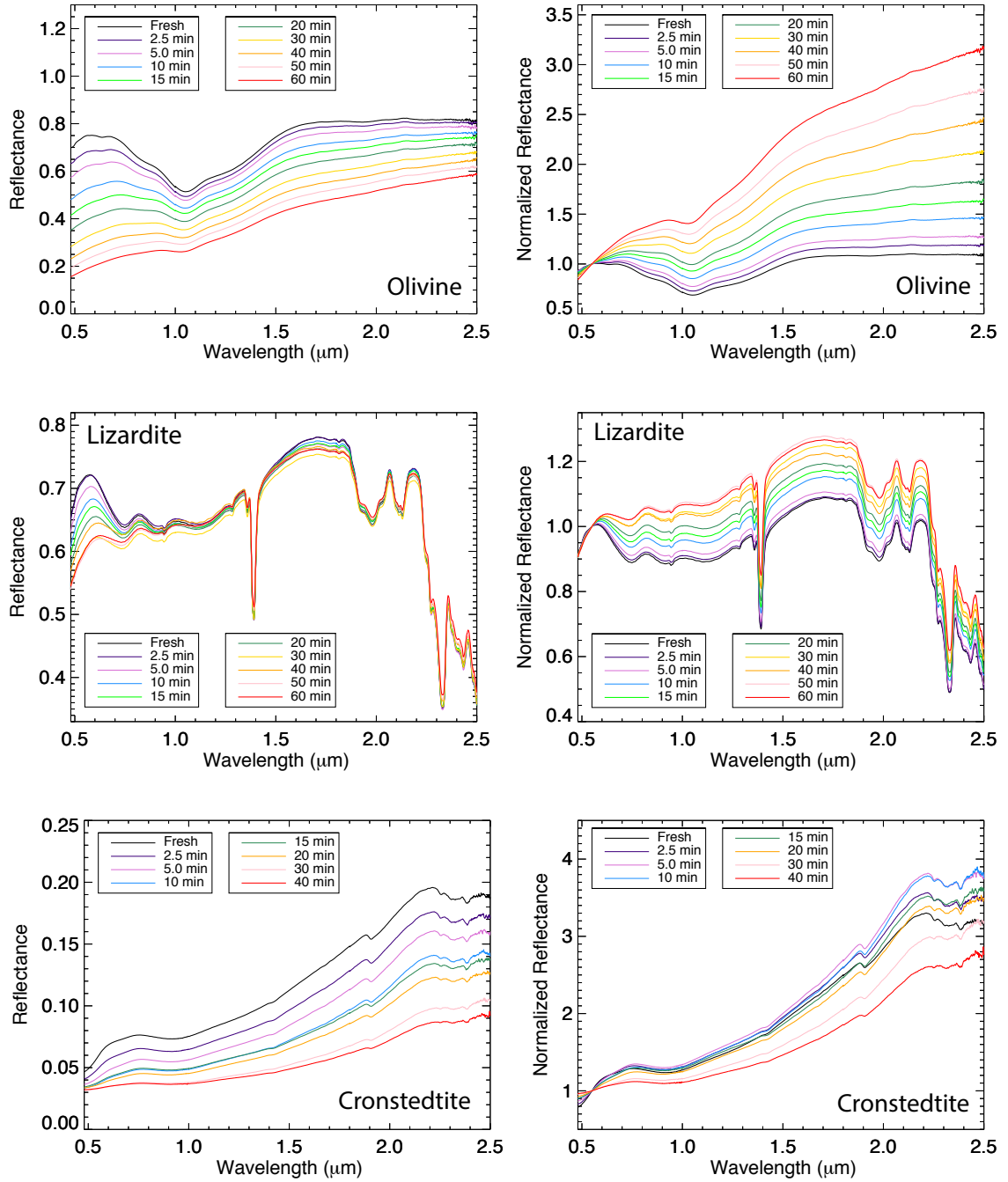


Figure 2.1 *Left:* Reflectance spectra for each of the minerals as a function of increasing irradiation time. *Right:* Reflectance spectra normalized to 0.55 μm .

Table 2.4. Radiative Transfer Model Inputs

Input Parameter	Olivine	Lizardite	Cronstedtite
n^{\dagger}	1.64	1.60	1.72
ρ^{\ddagger}	3.32	2.55	3.34

Note. — \dagger n is the real index of refraction. $\ddagger\rho$ is the mineral density.

of refraction, respectively; the mass fraction (M) of iron in the grain and coating relative to the host material and the density (ρ) of the host grain and metallic iron particles.

In addition to the optical effects of npFe⁰, Lucey & Riner (2011) used Mie theory to modify the Hapke (2001) model to allow a size-dependent treatment of the optical effects of space weathering. This modification allows consideration of the optical effects of the larger (> 50 nm) iron particles (termed Britt-Pieters particles; Lucey & Noble 2008) found in agglutinitic glass, which in contrast to the npFe⁰, darken and do not redden. We used the Lucey & Riner (2011) radiative transfer model to estimate the abundance and relative contribution of both npFe⁰ and Britt-Pieters particles on the spectra of each sample in response to laser irradiation.

The Lucey & Riner (2011) model requires an unweathered spectrum of the host material (e.g. lizardite), the viewing geometry ($i=30^\circ$ and $e=0^\circ$ for each of our spectra) of the reflectance spectrum, and the grain diameter, density and real indices of refraction of the host material. We used a grain size of $37.5\ \mu\text{m}$ as input to the model to represent the approximate mean diameter of our $<75\ \mu\text{m}$ samples. The real indices of refraction and density input parameters of each mineral are listed in Table 2.4. The model also requires values for the npFe⁰ and Britt-Pieters particle abundances as input. We used the IDL routine, MPFIT (Markwardt 2009), to perform a non-linear least squares fit between our modeled and observed spectra. Combining MPFIT with the radiative transfer model allowed us to determine the fraction of npFe⁰ and $1\ \mu\text{m}$ sized Britt-Pieters particles that produce

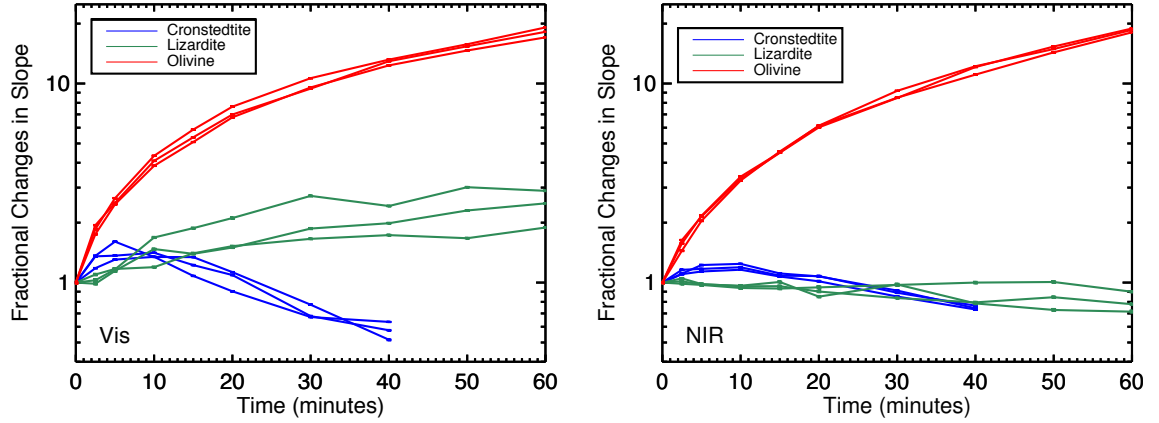


Figure 2.2 Plots of slope variations for each experiment. Data have been normalized to the slope value of the fresh, non-irradiated spectrum. *Left:* Visible slopes were measured using continuum points at 0.6 and 0.75 μm for cronstedtite, 0.57 and 1.7 μm for lizardite, and 0.7 and 1.6 μm for olivine. Due to lack of continuum points in the visible region, some visible slopes were measured using one value in the NIR region. *Right:* NIR slopes, which were measured using continuum points at 1.7 and 2.2 μm for cronstedtite, 1.7 and 2.16 μm for lizardite, and 1.6 and 2.3 μm for olivine.

the model that best fit our observed spectra. We ran two sets of models for each spectrum, one modeling only the effects of npFe^0 particles and the other modeling the dual effect of both npFe^0 and Britt-Pieters particles.

2.6 Results

2.6.1 Spectral Variation

Space weathering is known to alter the albedos, slopes and band depths of asteroid spectra. We normalized each of the albedo, slope and band depth measurements to initial value in each experiment to determine the relative change of each spectral feature and allow comparison between each of the minerals. The most significant spectral changes were seen in the increase of the olivine slopes in response to space weathering. Figure 2.2 shows the relative slope changes for each experiment and it is clear that the degree of slope change exhibited by the hydrated minerals is much less than olivine in both the visible and NIR.

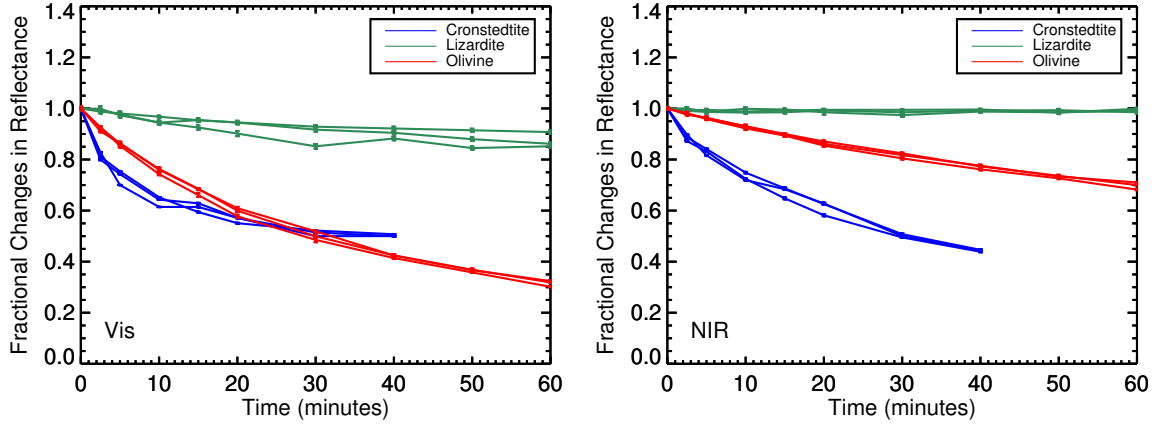


Figure 2.3 Plots of reflectance/albedo variations for each experiment. Data have been normalized to the albedo value of the fresh, non-irradiated spectrum *Left*: Visible albedo variations were measured using continuum points at $0.6 \mu\text{m}$ for cronstedtite, $0.57 \mu\text{m}$ for lizardite, and $0.7 \mu\text{m}$ for olivine. *Right*: NIR albedo variations were measured using continuum points at $2.2 \mu\text{m}$ for cronstedtite, $2.16 \mu\text{m}$ for lizardite, and $2.3 \mu\text{m}$ for olivine.

Lizardite shows an increase in the visible/NIR slope and a decrease in the NIR slope. It is interesting to note that lizardite appears to become spectrally redder in the visible/NIR region while simultaneously becoming bluer at NIR wavelengths. Cronstedtite is unique in the evolution of both its visible and NIR spectral slopes, where it initially reddens, then reverses and becomes bluer with increased irradiation. Although the cronstedtite slopes show similar trends at both visible and NIR wavelengths, the decrease in NIR slopes is slightly less dramatic than the decrease in visible slopes.

The albedo trends seen in olivine are similar to trends seen in previous works (Sasaki et al. 2001, 2003), where the albedo reduction is largest at the visible wavelengths. Lizardite shows a slight decrease in visible albedo, but no changes are observed at NIR wavelengths. As seen in Figure 2.3, cronstedtite initially darkens faster in the visible than the NIR, but slows and begins to plateau beyond ~ 15 minutes. The reverse from spectral reddening to blueing appears to result from the continued darkening in the NIR while albedo changes taper in the visible.

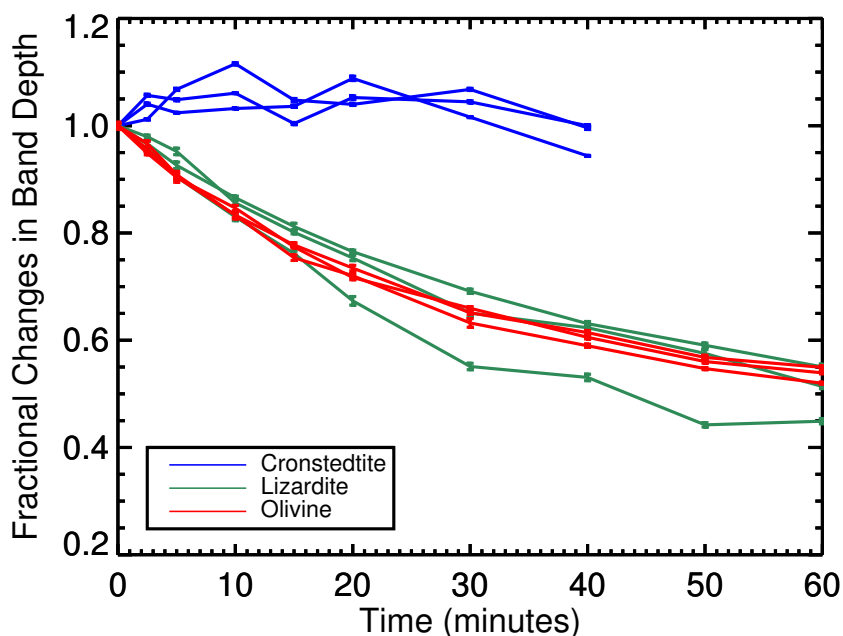


Figure 2.4 The fractional changes in the cronstedtite $\sim 1.5 \mu\text{m}$, lizardite $1.13 \mu\text{m}$, and olivine $1.05 \mu\text{m}$ band depths. The data have been normalized to the band depth of the fresh, non-irradiated spectrum for each experiment.

As seen in Figure 2.4, the relative changes in the $\sim 1.05 \mu\text{m}$ band for olivine and $1.13 \mu\text{m}$ band for lizardite are similar. However, lizardite, which has a large suite of absorption bands in the visible and NIR, shows a smaller reduction in band depths at for bands at longer wavelengths as compared to shorter wavelengths. In contrast to olivine and lizardite, cronstedtite shows little fluctuations in the $1.1 \mu\text{m}$ band. The full set of figures showing the reflectance and normalized reflectance and tables reporting that values used for the analysis in this paper are presented in the Appendix.

2.6.2 Volatile Production

Gas pressure measurements using the RGA recorded the variation in the pressures of N_2 , H_2O , H_2S , SO_2 , H , NO , NH_3 , CO , CO_2 produced during each irradiation. Water was the only volatile released that had measurable pressures above that of air. Figure 2.5

shows the mean water pressures derived from the three experiments conducted on each mineral, where the error bars represent the 1-sigma uncertainties. The small amount of water released during the irradiation of olivine is likely a product of adsorbed water. Lizardite and cronstedtite release about $10\times$ more water than olivine. Both phyllosilicates appear to contain similar amounts of water throughout each experiment. Unlike olivine, the production rates for lizardite and cronstedtite decrease very little from initial to final irradiations and do not appear to experience significant dehydration.

2.6.3 Radiative Transfer Models

The fraction of npFe^0 and Britt-Pieters particles as well as the resulting reduced χ^2 value for the best fit in each modeled spectrum are given in Table 2.5. The two series (npFe^0 , and $\text{npFe}^0 + \text{Britt-Pieters}$) of modeled spectra for olivine show no significant difference between

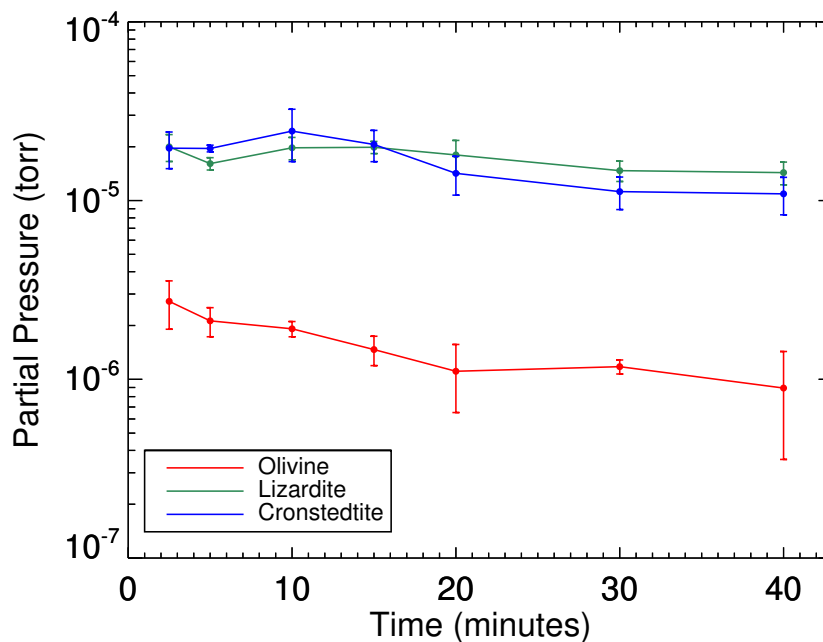


Figure 2.5 Partial pressure measurements of H_2O released during each irradiation interval. Values represent mean pressures and 1-sigma uncertainties derived from the three experiments conducted on each mineral.

Table 2.5. Summary of Model Results

Experiment	npFe ⁰ Particles [†] (wt%)	χ^2_{red}	npFe ⁰ Particles [‡] (wt%)	Britt-Pieters Particles (wt%)	χ^2_{red}
Olivine					
2.5 min	0.003	1.004	0.003	0.000	0.998
5.0 min	0.008	1.070	0.007	0.000	0.881
10 min	0.018	4.101	0.017	0.000	4.019
15 min	0.028	1.961	0.028	0.000	1.962
20 min	0.043	4.357	0.043	0.000	4.359
30 min	0.064	1.594	0.064	0.000	1.594
40 min	0.090	12.495	0.090	0.000	12.501
Lizardite					
2.5 min	0.000	0.357	0.000	0.000	0.357
5.0 min	0.001	0.423	0.001	0.001	0.299
10 min	0.002	0.938	0.002	0.000	0.939
15 min	0.002	2.239	0.002	0.000	2.240
20 min	0.004	1.297	0.004	0.000	1.297
30 min	0.006	2.629	0.006	0.000	2.630
40 min	0.003	7.543	0.003	0.000	7.546
Cronstedtite					
2.5 min	0.186	3.419	0.132	0.043	1.699
5.0 min	0.360	6.102	0.266	0.078	3.191
10 min	0.624	13.237	0.401	0.166	5.729
15 min	0.717	7.787	0.382	0.212	2.417
20 min	0.816	15.221	0.382	0.365	3.851
30 min	1.475	15.726	0.560	0.597	3.913
40 min	1.634	22.361	0.274	0.976	3.584

Note. — Nanophase iron (npFe) and Britt-Pieter particle abundances determined from radiative transfer modeling. [†]Abundances of npFe when only npFe particles are used in the model. [‡] Abundances of npFe when both npFe and Britt-Pieters particles are used in the model.

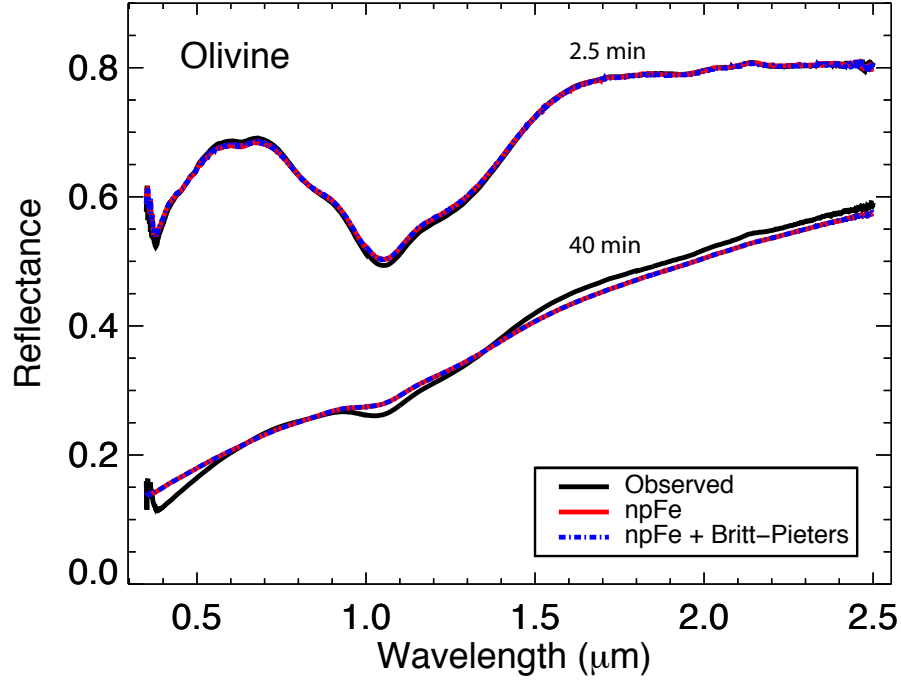


Figure 2.6 Observed reflectance spectra and radiative transfer models for olivine. For clarity, only the 2.5 minute and 40 minute models are shown.

the fits when the Britt-Pieters particles are included along with npFe^0 in the model (Fig. 2.6). We see no difference between the two model fits for the olivine spectra when the Britt-Pieters particles are included along with npFe^0 particles, suggesting no $1\ \mu\text{m}$ sized or larger particles are produced during irradiation.

The largest deviations between modeled and observe spectra were seen in the lizardite data (Fig. 2.7). Figure 2.8 shows the modeled cronstedtite spectra are significantly better fit to the observed data when a significant fraction of Britt-Pieters particles are used in the model. The radiative transfer models suggest the laser irradiation of cronstedtite results in the production of $\sim 1\ \mu\text{m}$ sized Britt-Pieters particles, whereas olivine and lizardite only produce npFe^0 particles.

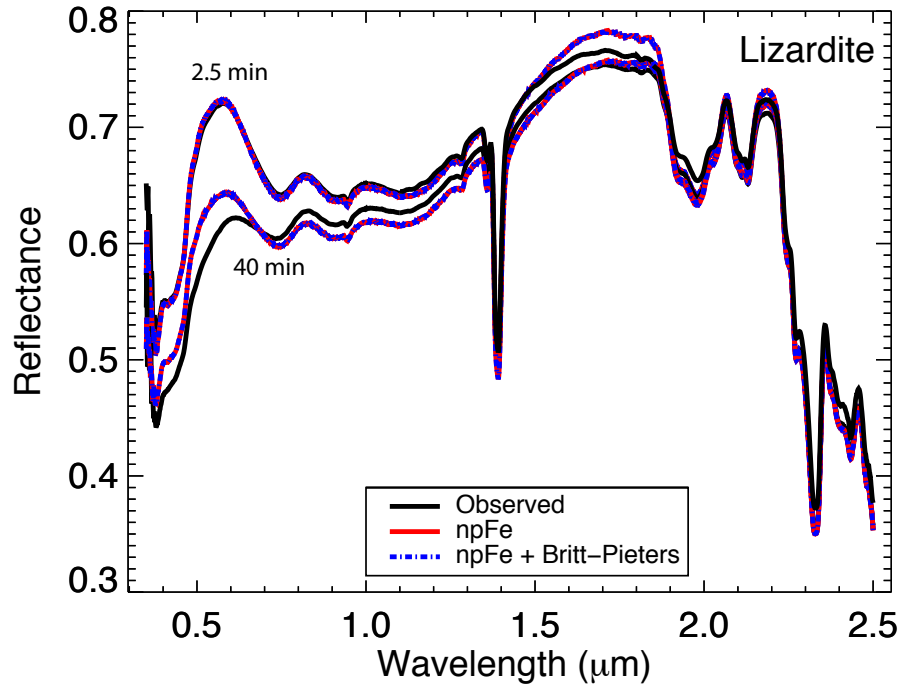


Figure 2.7 Observed reflectance spectra and radiative transfer models for lizardite. For clarity, only the 2.5 minute and 40 minute models are shown.

2.7 Discussion

2.7.1 The Role of Water

Previous space weathering experiments comparing the differences between anhydrous silicates suggest the degree of spectral reddening and darkening depend on the FeO content, melting points, and electrical conductivities of the host minerals (Moroz et al. 1996; Yamada et al. 1999; Sasaki et al. 2003; Moroz et al. 2014). Rivkin et al. (2002) postulate the energy from micrometeorite impacts may be used to first liberate the water in phyllosilicates and only after dehydration will reddening and darkening occur. We test this hypothesis by using laser irradiation to simulate micrometeorite impacts on phyllosilicates, which can contain a significant amount of water (up to 10 wt.% Morbidelli et al. 2000).

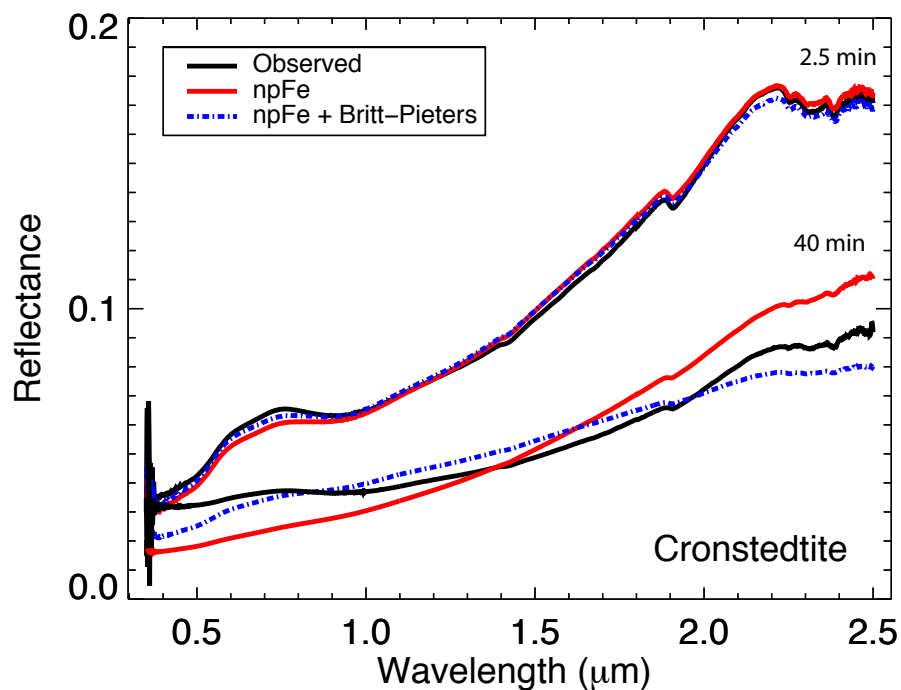


Figure 2.8 Observed reflectance spectra and radiative transfer models for cronstedtite. For clarity, only the 2.5 minute and 40 minute models are shown.

As seen in Figure 2.5, cronstedtite and lizardite release similar levels of water during each irradiation, and the amount of water released only decreases by a small fraction throughout the experiment. The small degree of decrease suggest lizardite and cronstedtite never become completely dehydrated. The emitted volatile (RGA) data in combination with the spectral changes observed in the phyllosilicates show that dehydration is not necessary for the production of npFe^0 or Britt-Pieters particles. However, it may be that a small fraction of the phyllosilicates become dehydrated during irradiation and it is this component that produces the iron particles resulting in darkening and the increase or decrease of spectral slopes.

2.7.2 Space Weathering Trends in Phyllosilicates

Moroz et al. (2004a) found ion irradiation of asphaltite, an analog for CC organics, produces a decrease in spectral slope in response to ion bombardment. The asphaltite spectral changes are attributed to carbonization as functional groups containing hydrogen are lost during irradiation. In contrast to changes induced by the production of iron particles, Moroz et al. (2004a) suggest carbonization increases the absorption coefficient and optical density of the asphaltite high enough for scattering to dominate in the region below $\sim 0.7 \mu\text{m}$. Hence, the bluer spectral slope results from the increase in reflectance below $\sim 0.7 \mu\text{m}$, while darkening occurs at longer wavelengths.

The cronstedtite sample is the first mineral mixture without an organic component to show a decrease in spectral slopes in response to space weathering. In contrast to the increase in reflectance below $\sim 0.7 \mu\text{m}$ that causes the bluer spectral slopes in Moroz et al. (2004a), the cronstedtite sample shows a bluer spectral slope due to a decrease in reflectance in the NIR wavelengths (Figure 2.3). Based on our radiative transfer models, we propose that cronstedtite becomes bluer due to optical changes induced by the production of Britt-Pieters particles. The normalized spectra (Figure 2.1) reveal that the cronstedtite sample shows an increase in spectral slopes in the first 10 minutes of irradiation, which corresponds to the higher fraction of npFe^0 than Britt-Pieters particles in our radiative transfer models. Table 2.5 shows the proportion of npFe^0 to Britt-Pieters particles as a function of irradiation for each mineral. The cronstedtite sample starts to exhibit a decrease in spectral slopes beyond 10 minutes, which also corresponds to when the model starts to show a much higher fraction of Britt-Pieters particles. As described by Hapke (2001), the production of npFe^0 results in spectral reddening due to the decrease in absorption efficiency at longer wavelengths (Figure 2.9). However, when particle size is close to λ , absorption efficiencies behave almost independent of λ (Hapke 2001), thus Lucey & Riner (2011) find that particles larger than $1 \mu\text{m}$ lead to darkening in the NIR wavelengths but no reddening. Indeed, as seen in Figure 2.3, the decrease in albedo begins to plateau in the visible wavelengths beyond ~ 10 minutes, but continues to decrease in the NIR region. Therefore, the initial reddening

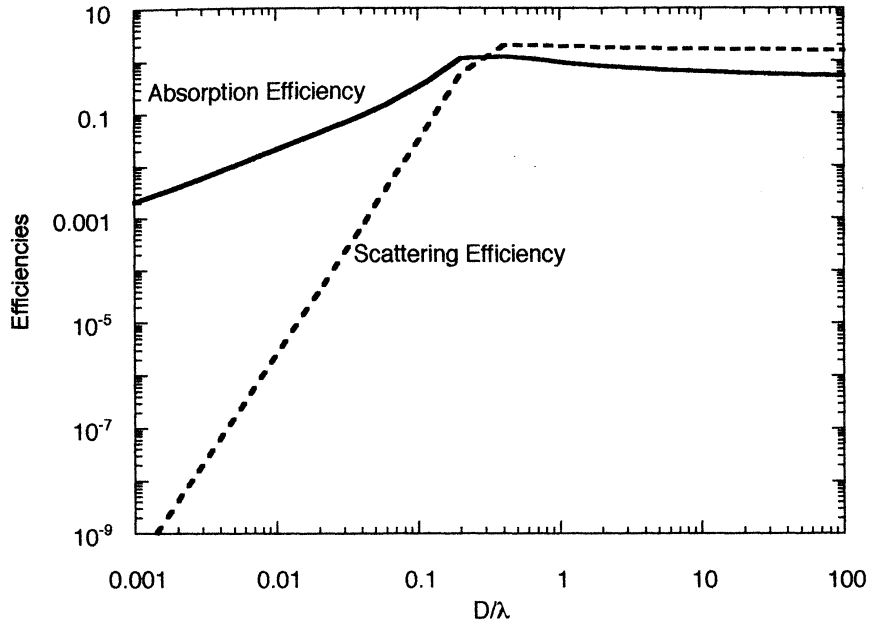


Figure 2.9 A figure from Hapke (2001) showing the absorption and scattering efficiencies as a function of the diameter to wavelength ratio.

of cronstedtite is likely a product of the optical effects of npFe^0 , whereas the progression to bluer spectral slopes is likely the result of the optical effects of Britt-Pieters particles.

Previous experiments on the Fe-poor silicate plagioclase resulted in little spectral darkening and reddening, which Moroz et al. (2014) attributes to a low FeO content. Lizardite is a Mg-end member phyllosilicate and as reported in Table 2.3, also has a small fraction of FeO. Despite the low FeO content, lizardite does show notable variations in slope and albedo, but as seen in Figures 2.2-2.3, the fractional changes in lizardite are typically the least pronounced of all the three minerals. Our radiative transfer models are consistent with these spectral trends as they suggest lizardite produces the least amount of npFe^0 . Although the slope evolution for lizardite and cronstedtite both decrease at NIR wavelengths, the radiative transfer models (Fig. 2.7) imply that no Britt-Pieters particles are produced during the irradiation of lizardite. Due to the lack of Britt-Pieters particles, it is unclear what may be causing the NIR slopes to get spectrally bluer in the lizardite sample.

It is important to note that the suite of lizardite spectra show significant variation when comparing each experiment, and further experiments are needed verify these spectral trends. Another unique trend seen in the lizardite data is the similarity in band depth suppression as compared to olivine. Although slope and albedo variations are less pronounced than olivine, the band depth variations are consistent between the two minerals. These data suggest the space weathering trends of both lizardite and cronstedtite are notably different than the trends seen in olivine and other anhydrous silicates.

2.7.3 Space Weathering Trends in Meteorites

Modal mineralogy of CCs show a progression from Fe-cronstedtite to Mg-serpentine as aqueous alteration progresses (Howard et al. 2009, 2011; Rubin et al. 2007). Table 2.1 depicts the increasing abundance of cronstedtite and serpentine in CCs for petrologic grades of ~ 3.0 to 1.0. Howard et al. (2014) found that cronstedtite forms early and remains relatively constant, whereas Mg-serpentine increase systematically with increased hydration. Following the formation of cronstedtite and MgFe-serpentine, the most aqueously altered meteorites show an increase in the formation of serpentine. Assuming the spectral evolution of the cronstedtite sample to space weathering is dominated by the cronstedtite component of the sample (and not pyrite or siderite), we propose the spectral trends of phyllosilicates appear to depend on the degree of aqueous alteration experienced by an asteroid or meteorite. Due to the significant fraction of phyllosilicates seen in CCs (up to 80 wt.% (Cloutis et al. 2011b)) and therefore their potential significant influence on the spectral trends of CCs, we compare our trends to those of previous space weathering experiments of CCs (Table 2.2).

The CM meteorite Mighei experienced a significant degree of aqueous alteration and has a high fraction of cronstedtite (~ 50 wt.% (Cloutis et al. 2011b)). However, laser-induced space weathering conducted by Moroz et al. (2004b); Shingareva et al. (2004) resulted in spectral reddening. Although the Moroz et al. (2004b); Shingareva et al. (2004) data are not consistent with the cronstedtite slope trends, it is important to note that the simulated

impact energies in Moroz et al. (2004b) were significantly larger than what was chosen for our experiments. The Moroz et al. (2004b) simulations resulted in the production of large glassy aggregates up to 100 μm in diameter (Shingareva et al. 2004). Thus, comparison between the Moroz et al. (2004b) experiment and our results is difficult since the Mighei experimental products are intrinsically different than the sub-micron sized iron particles (such as npFe^0 and Britt-Pieters sized particles) produced in our experiments.

Tagish Lake (TL) is a unique meteorites with affinities to CM2.0 and CI chondrites (Zolensky et al. 2002; Cloutis et al. 2012a), but is highly varied its composition. TL has both carbonate rich and carbonate poor lithologies, but overall is dominated by a Mg-rich serpentine and Fe-bearing phyllosilicate matrix (Zolensky et al. 2002; Izawa et al. 2010; Cloutis et al. 2012a), and contains an organic carbon component that is widely varied among the different lithogies (Cloutis et al. 2012a). Several space weathering experiments have been conducted on TL samples which produce varied results (Figure 2.2). Both Ar^+ ion bombardment and laser irradiation result in decreased spectral slopes (Hiroi et al. 2004; Vernazza et al. 2013), whereas an increase in slope is seen after He^+ ion bombardment (Vernazza et al. 2013).

Characterizing the spectral differences of TL in response to space weathering is difficult due to the heterogeneity of the TL samples and the different methods used in each experiment. However, in two of the three experiments, the spectral slopes become bluer due to an increase in reflectance in the visible wavelengths (Hiroi et al. 2004; Vernazza et al. 2013). The spectral evolution of TL is therefore similar to the trends seen in experiments on complex hydrocarbons (Moroz et al. 2004a) and is likely a result of the organic carbon component in TL. However, TL and our cronstedtite samples both contain the Fe-carbonate siderite (3 wt.%). Thus, the carbon component from siderite may be the cause of the spectral decrease in our cronstedtite sample. However, in contrast to the spectral evolution of asphaltite and TL, our cronstedtite sample shows a slope decrease as a result of reflectance decreasing in the NIR wavelengths. Therefore, the bluer spectral slopes in the cronstedtite samples appear to originate from a physical mechanism that is more consistent with the

production of Britt-Pieters particles than carbonization. Further experiments are needed to assess how siderite responds to simulated space weathering and whether carbon in a mineral phase also leads to a decrease in spectral slopes in response to laser irradiation. In addition, the response of CCs is complex, and currently, there is no clear link between the CC space weathering trends and the minerals presented in this chapter, thus future work is needed to assess whether space weathering trends do indeed vary as a function of the degree of aqueous alteration.

2.8 Summary

In this chapter, we present results from a new set of experiments simulating space weathering of phyllosilicates. In simulating micrometeorite bombardment through the laser irradiation of olivine, lizardite, and cronstedtite (which also contains a small fraction of siderite and pyrite), we find the following:

1. Complete dehydration of aqueously altered minerals is not necessary to for space weathering to be effective in producing npFe^0 or Britt-Pieters particles.
2. The slope decreases experienced by lizardite and cronstedtite differ from the slope increase seen in olivine. Our cronstedtite sample, which also contains a notable amount of siderite and pyrite, experiences a decrease in spectral slopes with increased irradiation in both the visible and NIR wavelengths. In contrast, lizardite experiences an increase in slopes in the visible region and a decrease in the NIR region.
3. The spectral trends in lizardite and cronstedtite imply that CCs and asteroids may experience space weathering trends that are dependent upon the degree of aqueous alteration experienced.
4. Lizardite shows a small degree of albedo decrease in the visible and no change in the NIR region, whereas both cronstedtite and olivine show a significant drop in albedo in the visible and NIR wavelengths.

5. Our radiative transfer models suggest the olivine and lizardite spectral changes result from the production of npFe^0 , whereas the spectral changes seen in the cronstedtite samples appear to originate from the production of $1\ \mu\text{m}$ sized Britt-Pieters particles.
6. Olivine and lizardite both show similar degrees in band depth suppression, whereas cronstedtite shows little variation.

References

- Beck, P., Garenne, A., Quirico, E., Bonal, L., Montes-Hernandez, G., Moynier, F., & Schmitt, B. 2014, *Icarus*, 229, 263
- Bland, P. A., Cressey, G., & Menzies, O. N. 2004, *Meteoritics and Planetary Science*, 39, 3
- Burbine, T. H. 1998, *Meteoritics and Planetary Science*, 33, 253
- Burbine, T. H., Binzel, R. P., Bus, S. J., & Clark, B. E. 2001, *Meteoritics and Planetary Science*, 36, 245
- Bus, S. J. & Binzel, R. P. 2002, *Icarus*, 158, 106
- Buseck, P. R. & Hua, X. 1993, *Annual Review of Earth and Planetary Sciences*, 21, 255
- Cassidy, W. & Hapke, B. 1975, *Icarus*, 25, 371
- Chapman, C. R. 2004, *Annual Review of Earth and Planetary Sciences*, 32, 539
- Clark, R. N. & Roush, T. L. 1984, *J. Geophys. Res.*, 89, 6329
- Cloutis, E. A., Hiroi, T., Gaffey, M. J., Alexander, C. M. O. ., & Mann, P. 2011a, *Icarus*, 212, 180
- Cloutis, E. A., Hudon, P., Hiroi, T., Gaffey, M. J., & Mann, P. 2011b, *Icarus*, 216, 309
- Cloutis, E. A., Hudon, P., Hiroi, T., Gaffey, M. J., & Mann, P. 2012a, *Icarus*, 221, 984

- Cloutis, E. A., Hudon, P., Hiroi, T., Gaffey, M. J., Mann, P., & Bell, J. F. 2012b, *Icarus*, 221, 328
- Conel, J. E. & Nash, D. B. 1970, *Geochimica et Cosmochimica Acta Supplement*, 1, 2013
- Fischer, E. M., Pieters, C. M., & Pratt, S. F. 1994, in *Lunar and Planetary Science Conference*, Vol. 25, *Lunar and Planetary Science Conference*, 371
- Fornasier, S., Lantz, C., Barucci, M. A., & Lazzarin, M. 2014, *Icarus*, 233, 163
- Gillis-Davis, J. J., Lucey, P. G., Bradley, J. P., Misra, A., Kaluna, H. M., Takir, D., & Joseph, B. E. C. submitted, *Geophys. Res. Lett.*
- Gold, T., Campbell, M. J., & O’Leary, B. T. 1970, *Geochimica et Cosmochimica Acta Supplement*, 1, 2149
- Hapke, B. 1966, *The Nature of the Lunar Surface*, ed. W. Hess, D. Menzel, & J. O’Keefe (Baltimore, Md: Johns Hopkins Univ. Press), 141–154
- Hapke, B. 1973, *Darkening of Silicate Rock Powders by Solar Wind Sputtering*, Vol. 7, 342–355
- Hapke, B. 1981, *J. Geophys. Res.*, 86, 4571
- Hapke, B. 1993, *Theory of reflectance and emittance spectroscopy*
- Hapke, B. 2001, *J. Geophys. Res.*, 106, 10039
- Hapke, B., Cassidy, W., & Wells, E. 1975, *Effects of vapor-phase deposition processes on the optical, chemical, and magnetic properties of the lunar regolith*, Vol. 13, 339–353
- Hapke, B. W., Cohen, A. J., Cassidy, W. A., & Wells, E. N. 1970, *Geochimica et Cosmochimica Acta Supplement*, 1, 2199
- Hiroi, T., Moroz, L. V., Shingareva, T. V., Basilevsky, A. T., & Pieters, C. M. 2003, in *Lunar and Planetary Science Conference*, Vol. 34, *Lunar and Planetary Science Conference*, ed. S. Mackwell & E. Stansbery, 1324

- Hiroi, T., Pieters, C. M., Rutherford, M. J., Zolensky, M. E., Sasaki, S., Ueda, Y., & Miyamoto, M. 2004, in *Lunar and Planetary Inst. Technical Report*, Vol. 35, Lunar and Planetary Science Conference, ed. S. Mackwell & E. Stansbery, 1616
- Hiroi, T., Zolensky, M. E., Pieters, C. M., & Lipschutz, M. E. 1996, *Meteoritics and Planetary Science*, 31, 321
- Howard, K. T., Alexander, C. M. O. ., Schrader, D. L., & Dyl, K. . 2014, *Geochimica et Cosmochimica Acta*,
- Howard, K. T., Benedix, G. K., Bland, P. A., & Cressey, G. 2009, *Geochimica et Cosmochimica Acta*, 73, 4576
- Howard, K. T., Benedix, G. K., Bland, P. A., & Cressey, G. 2011, *Geochimica et Cosmochimica Acta*, 75, 2735
- Izawa, M. R. M., Flemming, R. L., King, P. L., Peterson, R. C., & McCausland, P. J. A. 2010, *Meteoritics and Planetary Science*, 45, 675
- James, C. L., Basu, A., Wentworth, S. J., & McKay, D. S. 2001, in *GSA Ann. Meet. Abstract No. 27433*
- Jedicke, R., Nesvorný, D., Whiteley, R., Ivezić, Ž., & Jurić, M. 2004, *Nature*, 429, 275
- Keller, L. P. & McKay, D. S. 1993, *Science*, 261, 1305
- Keller, L. P., Wentworth, S. J., & McKay, D. S. 1998, in *New Views of the Moon: Integrated Remotely Sensed, Geophysical, and Sample Datasets*, ed. B. L. Jolliff & G. Ryder, 44
- Lazzarin, M., Marchi, S., Moroz, L. V., Brunetto, R., Magrin, S., Paolicchi, P., & Strazzulla, G. 2006, *ApJ*, 647, L179
- Lucey, P. G. & Noble, S. K. 2008, *Icarus*, 197, 348
- Lucey, P. G. & Riner, M. A. 2011, *Icarus*, 212, 451

- Markwardt, C. B. 2009, in *Astronomical Society of the Pacific Conference Series*, Vol. 411, *Astronomical Data Analysis Software and Systems XVIII*, ed. D. A. Bohlender, D. Durand, & P. Dowler, 251
- Masiero, J. R., Mainzer, A. K., Grav, T., Bauer, J. M., Cutri, R. M., Dailey, J., Eisenhardt, P. R. M., McMillan, R. S., Spahr, T. B., Skrutskie, M. F., Tholen, D., Walker, R. G., Wright, E. L., DeBaun, E., Elsbury, D., Gautier, IV, T., Gomillion, S., & Wilkins, A. 2011, *ApJ*, 741, 68
- McKay, D. S., Heiken, G. H., Basu, A., Blanford, G., Simon, S., Reedy, R., French, B. M., & Papike, J. 1991, *Lunar Sourcebook*, ed. G. H. Heiken (Cambridge University Press), 285–356
- Morbidelli, A., Chambers, J., Lunine, J. I., Petit, J. M., Robert, F., Valsecchi, G. B., & Cyr, K. E. 2000, *Meteoritics and Planetary Science*, 35, 1309
- Moroz, L., Baratta, G., Strazzulla, G., Starukhina, L., Dotto, E., Barucci, M. A., Arnold, G., & Distefano, E. 2004a, *Icarus*, 170, 214
- Moroz, L. V., Fisenko, A. V., Semjonova, L. F., Pieters, C. M., & Korotaeva, N. N. 1996, *Icarus*, 122, 366
- Moroz, L. V., Hiroi, T., Shingareva, T. V., Basilevsky, A. T., Fisenko, A. V., Semjonova, L. F., & Pieters, C. M. 2004b, in *Lunar and Planetary Science Conference*, Vol. 35, *Lunar and Planetary Science Conference*, ed. S. Mackwell & E. Stansbery, 1279
- Moroz, L. V., Starukhina, L. V., Rout, S. S., Sasaki, S., Helbert, J., Baither, D., Bischoff, A., & Hiesinger, H. 2014, *Icarus*, 235, 187
- Nesvorný, D., Jedicke, R., Whiteley, R. J., & Ivezić, Ž. 2005, *Icarus*, 173, 132
- Rivkin, A. S., Howell, E. S., Vilas, F., & Lebofsky, L. A. 2002, *Asteroids III*, 235
- Rubin, A. E. 2007, in *Lunar and Planetary Science Conference*, Vol. 38, *Lunar and Planetary Science Conference*, 1230

- Rubin, A. E., Trigo-Rodríguez, J. M., Huber, H., & Wasson, J. T. 2007, *Geochim. Cosmochim. Acta*, 71, 2361
- Sarrazin, P., Chipera, S., Bish, D., Blake, D., & Vaniman, D. 2005, *Advances in X-ray Analysis*, 48, 156
- Sasaki, S., Kurahashi, E., Yamanaka, C., & Nakamura, K. 2003, *Advances in Space Research*, 31, 2537
- Sasaki, S., Nakamura, K., Hamabe, Y., Kurahashi, E., & Hiroi, T. 2001, *Nature*, 410, 555
- Shingareva, T. V., Basilevsky, A. T., Fisenko, A. V., Semjonova, L. F., & Korotaeva, N. N. 2004, in *Lunar and Planetary Science Conference*, Vol. 35, *Lunar and Planetary Science Conference*, ed. S. Mackwell & E. Stansbery, 1137
- Vernazza, P., Fulvio, D., Brunetto, R., Emery, J. P., Dukes, C. A., Cipriani, F., Witasse, O., Schaible, M. J., Zanda, B., Strazzulla, G., & Baragiola, R. A. 2013, *Icarus*, 225, 517
- Yamada, M., Sasaki, S., Nagahara, H., Fujiwara, A., Hasegawa, S., Yano, H., Hiroi, T., Ohashi, H., & Otake, H. 1999, *Earth, Planets, and Space*, 51, 1255
- Zolensky, M. E., Nakamura, K., Gounelle, M., Mikouchi, T., Kasama, T., Tachikawa, O., & Tonui, E. 2002, *Meteoritics and Planetary Science*, 37, 737

Chapter 3

Optical Space Weathering Trends Among Carbonaceous Asteroids

3.1 Introduction

Space weathering studies of asteroids have primarily focused upon the alteration of the silicate rich S-complex asteroids. These moderate albedo ($p_v \sim 0.15-0.3$; Ryan & Woodward 2010) asteroids are known to spectrally darken, redden and have increasingly suppressed absorption bands as a function of time (Clark et al. 2002; Chapman 2004). The intrinsically dark ($p_v \sim 0.02-0.08$; Ryan & Woodward 2010) nature of carbonaceous material and the lack of prominent absorption features implied space weathering trends would be difficult to identify for C-complex asteroids (Hapke 2001; Moroz et al. 1996), however, two recent studies indicate significant spectral slope variation among this class of asteroids as a function of age (Nesvorný et al. 2005; Lazzarin et al. 2006).

Principal component analyses of asteroid colors in the SDSS show C-complex asteroid families become spectrally bluer (decrease in spectral slope) with age at optical wavelengths (Nesvorný et al. 2005). In contrast, a study using spectroscopic data from the SMASS II Bus & Binzel (2002b), show spectral slopes redden (increase in spectral slope) with age (Lazzarin et al. 2006). Both of the trends in these two surveys are attributed to space weathering processes, however the discrepancies between the two studies are attributed

to sampling different mineralogies within the broad C-complex population Lazzarin et al. (2006).

The young Karin (5 Myr; Nesvorný et al. 2002) and old Koronis (2.5 Gyr; Marzari et al. 1995) asteroid families were used to confirm that S-complex spectral trends with age were indeed a result of space weathering and not a product of mineralogical variation (Nesvorný et al. 2005). The recent discovery of a sub-family of the Themis asteroids allows a similar test to be conducted on carbonaceous asteroids. The Themis asteroid family (Hirayama 1918) has $\sim 4,000$ members (Milani et al. 2014) resulting from the catastrophic break up of a 390-450 km parent body asteroid 2.3 Gyr ago (Marzari et al. 1995). A recent (< 10 Mya) break up of a Themis family member (~ 20 km to 65 km in size) resulted in the formation of the Beagle family which contains ~ 60 asteroids (Nesvorný et al. 2008). These two families are the first C-type families identified which originate from the same parent body (Nesvorný et al. 2008), and provide a unique tool for assessing C-complex space weathering trends while alleviating mineralogical variations among C-complex asteroids.

In this chapter we use spectroscopic and albedo data to search for space weathering trends among the Themis and Beagle asteroids. We also search for trends among the Veritas asteroid family, which is another young (8.3 Myr; Nesvorný et al. 2003) C-complex family not related to the Themis and Beagle asteroids, to assess whether differences in mineralogy affected the spectral trends of Nesvorný et al. (2005).

3.2 Observations

In this paper, we present data for 52 main-belt asteroids belonging to the Themis, Beagle and Veritas asteroid families. Observations took place on 3.5 nights during Mar. 03, Oct. 29, Oct. 30, 2013 and Feb. 21, 2014 at the 8.2-meter Subaru telescope on Maunakea, Hawai'i (see Tables 3.1-3.3 for log of observations). Spectroscopic data covering the $0.47 < \lambda < 0.91 \mu\text{m}$ wavelength range were taken with the Faint Object Camera and Spectrograph (FOCAS). FOCAS has two $2\text{K} \times 4\text{K}$ CCDs with a total of 8 readout channels, each with

512×4176 pixels (Kashikawa et al. 2002). The spectra were recorded in channel 3 of chip 2, which has a read noise of 3.4 e- and gain of 2.082 e-/ADU. We used the lowest resolution grating (75 gr/mm) and 2x2 binning to obtain the highest signal to noise for our targets which are dominated by relatively small (<15 km) and faint asteroids. The resulting low resolution dispersion of 11.8 Å/pixel is ideal for detecting the shallow and broad absorption features typically seen in C-complex asteroid spectra. The SY47 order sorting filter was used to prevent higher order contamination. Observations were taken through a 1" wide slit, oriented to the parallactic angle, while tracking at non-sidereal rates. Due to the lack of non-sidereal guiding and to prevent drifting across the slit, integration times were limited to 600 seconds.

Family members were selected based on the dynamically derived memberships found in Nesvorný (2012). Previous studies show trends where the frequency of asteroids with absorption features varies as a function of diameter (Florczak et al. 1999; Fornasier et al. 2014), so Themis and Veritas targets were limited to members with similar diameters as Beagle targets (≤ 15 km) to avoid size related variations. Nearby solar analog stars were observed at airmasses similar to the asteroids throughout the night and ThAr lamp spectra were taken at the beginning or end of each observing run for wavelength calibration.

3.3 Data Reduction and Analysis

Data were reduced using the Image Reduction and Analysis Facility (IRAF) V2.14 `noao` `longslit` and Subaru `focasred` packages (Tody 1986). The reduction procedure included overscan and bias subtraction, image trimming, flattening, and cosmic ray removal for long exposure images. The `apall` package was used to perform background subtraction, extraction of the one-dimensional and the associated sigma spectrum from the two-dimensional images. The sigma spectrum is produced by measuring the sigma at each wavelength in the two-dimensional image. Following extraction, data were wavelength calibrated using emission lines from the ThAr lamp spectra.

Table 3.1. Observing Geometry and Conditions: Themis Family Asteroids

Asteroid ID	Vmag	a (AU)	e	i (deg)	r [†] (AU)	Δ^{\ddagger} (AU)	α^{\S} (deg)	Obs Run	No. of Spectra	Airmass (Object)	Solar Analog	Airmass (Stand)
7511	17.5	3.205	0.157	1.277	2.694	2.023	6.739	3	2	1.23	HD19061	1.29
8697	18.7	3.106	0.162	0.978	3.606	2.637	3.641	4	2	1.04	HD73708	1.03
15572	18.1	3.209	0.168	2.109	3.030	2.131	9.525	3	2	1.30	HD7983	1.28
15772	19.6	3.217	0.143	2.694	3.530	3.265	16.127	4	2	1.06	HD284013	1.02
16877	17.6	3.055	0.122	1.307	2.726	1.775	7.075	4	2	1.04	HD73708	1.03
18946	19.3	3.046	0.178	0.522	3.181	2.281	8.836	1	1	1.46	HD73708	1.39
26633	18.2	3.220	0.176	2.544	2.702	1.852	12.816	3	2	1.27	HD7983	1.28
28789	18.9	3.132	0.172	0.513	2.857	1.964	10.830	3	2	1.03	HD19061	1.11
31093	17.7	3.135	0.162	3.119	3.144	2.256	9.348	4	2	1.44	G104-335	1.45
31334	17.7	3.176	0.132	1.436	2.807	1.865	7.536	4	2	1.03	HD73708	1.03
38365	18.9	3.198	0.194	2.558	3.275	2.308	4.506	1	1	1.49	BD+30 2047	1.34
47920	18.0	3.126	0.145	2.967	3.186	2.206	3.570	3	2	1.03	HD19061	1.02
51143	18.4	3.146	0.167	1.178	3.139	2.213	8.052	3	2	1.03	HD19061	1.11
51579	19.4	3.166	0.196	2.688	2.610	2.416	22.362	3	2	1.35	HD197081	1.26
54320	17.8	3.116	0.186	0.635	2.543	1.559	3.519	3	2	1.13	HD19061	1.02
58231	17.6	3.222	0.156	2.033	2.735	1.744	1.067	3	2	1.16	HD19061	1.11
58302	18.3	3.097	0.156	1.607	2.710	1.808	10.675	1	1	1.27	HD73708	1.39

Table 3.1—Continued

Asteroid ID	Vmag	a (AU)	e	i (deg)	r^{\dagger} (AU)	Δ^{\ddagger} (AU)	α^{\S} (deg)	Obs Run	No. of Spectra	Airmass (Object)	Solar Analog	Airmass (Stand)
82646	18.1	3.061	0.163	3.381	2.692	1.740	7.111	4	2	1.11	HD73708	1.03
91965	18.7	3.244	0.113	1.381	2.977	2.091	10.189	1	1	1.41	HD73708	1.39
123646	18.5	3.227	0.117	2.436	2.901	1.911	1.171	1	1	1.66	HD95868	1.55
132845	20.1	3.122	0.175	1.516	2.580	1.993	20.330	3	2	1.64	HD199011	1.66
149084	19.7	3.180	0.166	2.603	2.676	1.840	13.769	1	1	1.35	HD73708	1.39

Note. — Orbital elements (a, e, i) ephemerides, and observational data for each asteroid. Observing run numbers correspond to Run 1= Mar. 02, 2013, Run 2 = Oct. 29, 2013, Run 3 = Oct. 30, 2013, Run 4= Feb. 21, 2014. † heliocentric distance ‡ geocentric distance § phase angle

Table 3.2. Observing Geometry and Conditions: Beagle Family Asteroids

Asteroid ID	Vmag	a (AU)	e	i (deg)	r [†] (AU)	Δ^{\ddagger} (AU)	α^{\S} (deg)	Obs Run	No. of Spectra	Airmass (Object)	Solar Analog	Airmass (Stand)
7968	20.5	3.157	0.163	1.386	2.856	2.233	17.417	3	2	1.23	HD220764	1.27
8161	17.0	3.167	0.168	2.544	2.778	1.787	1.565	2	2	1.25	HD19061	1.20
	19.2	—	—	—	2.944	3.113	18.518	4	2	1.21	HD19061	1.11
19923	18.5	3.161	0.111	1.698	2.839	2.068	14.693	4	2	1.15	G104-335	1.13
21569	19.2	3.164	0.116	0.676	2.849	2.578	20.266	1	1	1.37	G104-335	1.33
26140	19.2	3.152	0.137	2.545	3.419	2.563	9.435	3	2	1.29	HD7983	1.28
55188	18.6	3.160	0.183	2.453	2.807	2.407	20.152	2	2	1.00	HD73708	1.04
63951	20.2	3.154	0.180	0.454	2.693	2.456	21.632	3	2	1.12	HD73708	1.20
71489	19.7	3.150	0.130	0.781	3.420	2.966	15.844	3	2	1.27	HD603	1.28
84230	20.0	3.157	0.167	0.925	2.911	2.194	15.416	3	2	1.13	HD220764	1.28
88079	19.2	3.151	0.139	0.112	2.761	1.870	10.939	1	1	1.06	HD73708	1.09
104671	19.5	3.162	0.162	0.852	3.061	2.068	0.397	2	2	1.04	HD19061	1.02
116557	20.2	3.161	0.165	1.203	2.934	2.177	14.392	3	2	1.35	HD220764	1.27
140399	20.0	3.146	0.174	1.701	2.705	2.719	21.053	3	2	1.22	HD73708	1.20
	18.7	—	—	—	2.870	1.905	5.227	4	2	1.60	HD95868	1.28
143633	20.1	3.160	0.109	0.755	2.912	2.004	9.276	4	2	1.13	G104-335	1.13
144732	20.6	3.152	0.134	0.435	3.011	2.305	15.249	2	3	1.45	HD284013	1.29

Table 3.2—Continued

Asteroid ID	Vmag	a (AU)	e	i (deg)	r[†] (AU)	Δ^{\ddagger} (AU)	α^{\S} (deg)	Obs Run	No. of Spectra	Airmass (Object)	Solar Analog	Airmass (Stand)
150625	20.3	3.150	0.181	1.353	3.179	2.188	0.077	1	1	1.43	HD95868	1.39
166780	19.1	3.159	0.170	1.343	2.695	1.702	0.866	2	2	1.09	HD19061	1.02
178208	19.8	3.172	0.113	2.565	3.056	2.070	1.835	4	2	1.10	HD95868	1.05
180762	20.9	3.147	0.175	2.183	3.659	2.697	4.341	1	1	1.30	HD95868	1.24
182228	20.2	3.153	0.170	1.990	3.209	2.240	4.422	1	1	1.09	HD73708	1.09
202360	20.8	3.153	0.132	2.455	3.566	2.579	2.198	2	2	1.33	HD19061	1.20
203061	20.8	3.151	0.157	0.326	3.155	2.167	2.293	3	2	1.30	HD19061	1.11
211009	19.5	3.152	0.132	1.859	2.759	1.782	4.007	4	2	1.33	HD95868	1.28

Note. — Orbital elements (a, e, i) ephemerides, and observational data for each asteroid. Observing run numbers correspond to Run 1= Mar. 02, 2013, Run 2 = Oct. 29, 2013, Run 3 = Oct. 30, 2013, Run 4= Feb. 21, 2014. [†]heliocentric distance [‡]geocentric distance [§]phase angle

Table 3.3. Observing Geometry and Conditions: Veritas Family Asteroids

Asteroid ID	Vmag	a (AU)	e	i (deg)	r [†] (AU)	Δ [‡] (AU)	α [§] (deg)	Obs Run	No. of Spectra	Airmass (Object)	Solar Analog	Airmass (Stand)
5592	17.3	3.173	0.062	8.511	3.254	2.696	15.777	3	2	1.05	HD73708	1.03
7231	17.1	3.168	0.075	9.429	2.947	2.215	14.862	3	2	1.20	HD220764	1.28
8624	18.9	3.166	0.032	9.080	3.207	2.384	11.364	4	2	1.04	HD42160	1.14
62512	19.0	3.165	0.065	8.807	3.015	2.040	3.871	4	2	1.05	HD73708	1.03
82961	18.6	3.163	0.057	8.317	3.145	2.163	3.138	3	2	1.09	HD19061	1.02
169282	20.0	3.166	0.082	10.236	3.074	2.536	17.079	4	2	1.04	HD257880	1.02
215270	19.5	3.172	0.079	10.117	2.951	2.027	8.560	2	2	1.15	HD19061	1.20

Note. — Orbital elements (a, e, i) ephemerides, and observational data for each asteroid. Observing run numbers correspond to Run 1= Mar. 02, 2013, Run 2 = Oct. 29, 2013, Run 3 = Oct. 30, 2013, Run 4= Feb. 21, 2014. [†]heliocentric distance [‡]geocentric distance [§]phase angle

Median combined asteroid spectra were divided by nearby G2V solar analog spectra to produce reflectance spectra for each asteroid. Residual features due to incomplete removal of sky lines were removed using a median filter to search for erroneous spikes in the final reflectance spectra. Tables 3.1-3.1 report which solar analog stars were used to produce the reflectance spectra for each asteroid.

We measured slopes using the equation for the normalized reflectivity gradient S' (reported in units of $\%/1000 \text{ \AA}$), as defined by Jewitt & Meech (1986):

$$S'(\lambda_1, \lambda_2) = \left(\frac{dS/d\lambda}{S_{0.55}} \right) \quad (3.1)$$

where $dS / d\lambda$ is the slope of the reflectivity measured within the wavelength region between λ_1 and λ_2 . Reflectance spectra were normalized to $0.55 \text{ }\mu\text{m}$ and spectral slopes were measured using a weighted linear least-squares fit to data between $0.49 < \lambda < 0.91 \text{ }\mu\text{m}$. The fits were weighted using the IRAF generated sigma spectrum for each asteroid. Data shorter than $0.49 \text{ }\mu\text{m}$ were not included in the fit due to a possible steep drop in reflectance below $\sim 0.5 \text{ }\mu\text{m}$ created by the $\text{Fe}^{2+} \rightarrow \text{Fe}^{3+}$ intervalence charge transfer in phyllosilicates (Vilas 1994; Hiroi et al. 1996). Asteroid slopes and 1-sigma uncertainties are show in Tables 3.4-3.6. Negative slopes indicate asteroids that scatter more light than the Sun at short wavelengths, whereas positive slopes correspond to objects that scatter more light at long wavelengths.

To search for the shallow $0.7 \text{ }\mu\text{m}$ phyllosilicate feature we performed continuum removal and fit the $0.55\text{-}0.85\text{ }\mu\text{m}$ feature region with a 2nd or 3rd order polynomial. The continuum removal was performed by dividing the full spectrum by a linear fit to the $0.7 \text{ }\mu\text{m}$ continuum shoulders ($0.52\text{-}0.54 \text{ }\mu\text{m}$ and $0.86\text{-}0.88 \text{ }\mu\text{m}$). The continuum removed spectra are shown in Figures 3.1-3.4. The band depth and center were determined using the reflectance value at the wavelength corresponding to the minimum of the polynomial fit. The band depth uncertainty was derived using the uncertainty in the sigma spectrum corresponding to the position of the band center and only features with band depths greater than the

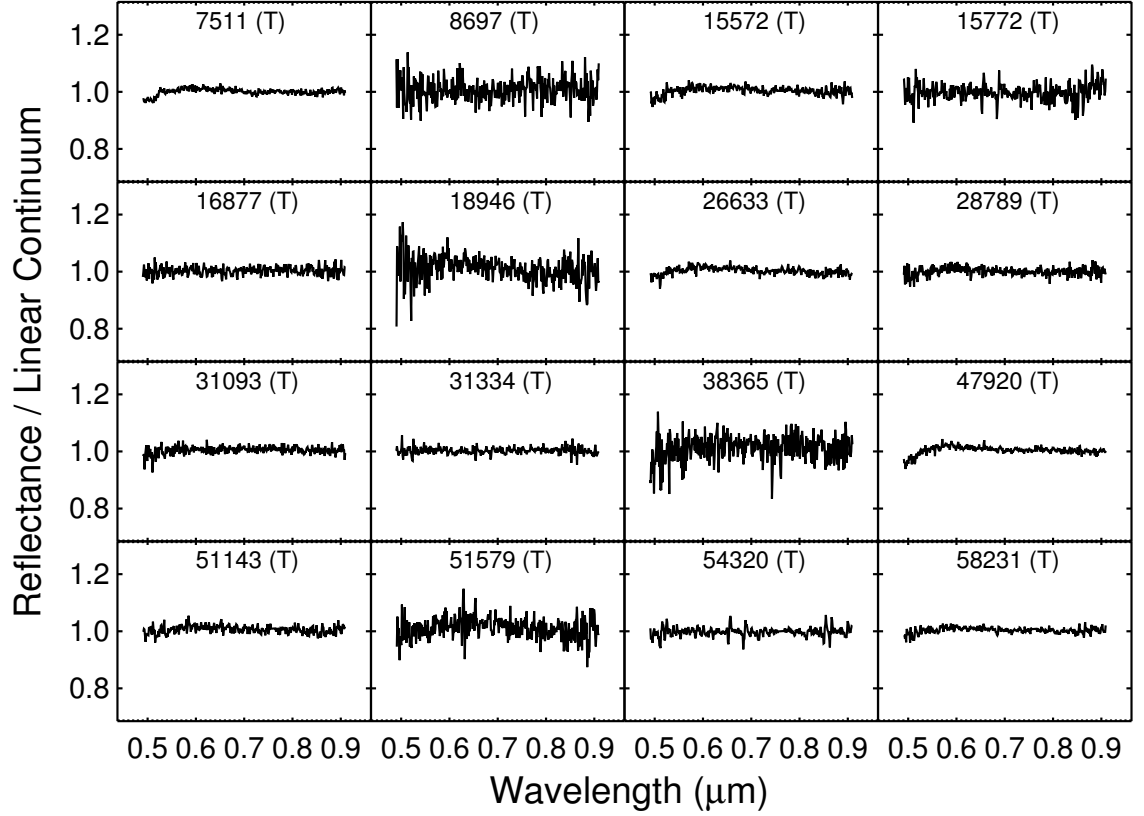


Figure 3.1 Continuum removed spectra of Themis asteroids. Continuum removal was performed by dividing the full spectrum by a linear fit to 0.52-0.54 μm and 0.86-0.88 μm spectral regions. Labels show the asteroid ID as well as family membership, where (T) are Themis, family members.

associated uncertainties were flagged as a detection. Band depths for objects where features were detected and sensitivity limits computed from the signal-to-noise ratio (SNR) of each spectrum are reported in Tables 3.4-3.6.

In addition to our Subaru data, we use visible albedos derived by Masiero et al. (2011) from the Wide-field Infrared Survey Explorer (WISE) to characterize the albedo distributions of Themis, Beagle and Veritas asteroids. We used 2025, 565, and 16 Themis, Veritas and Beagle members, respectively, in our analyses but divided the data set into two size populations (cutoff = 15 km) for consistency with our Subaru data set. The mean values for slope and albedo, the standard error of the mean (SEM) and the standard deviations

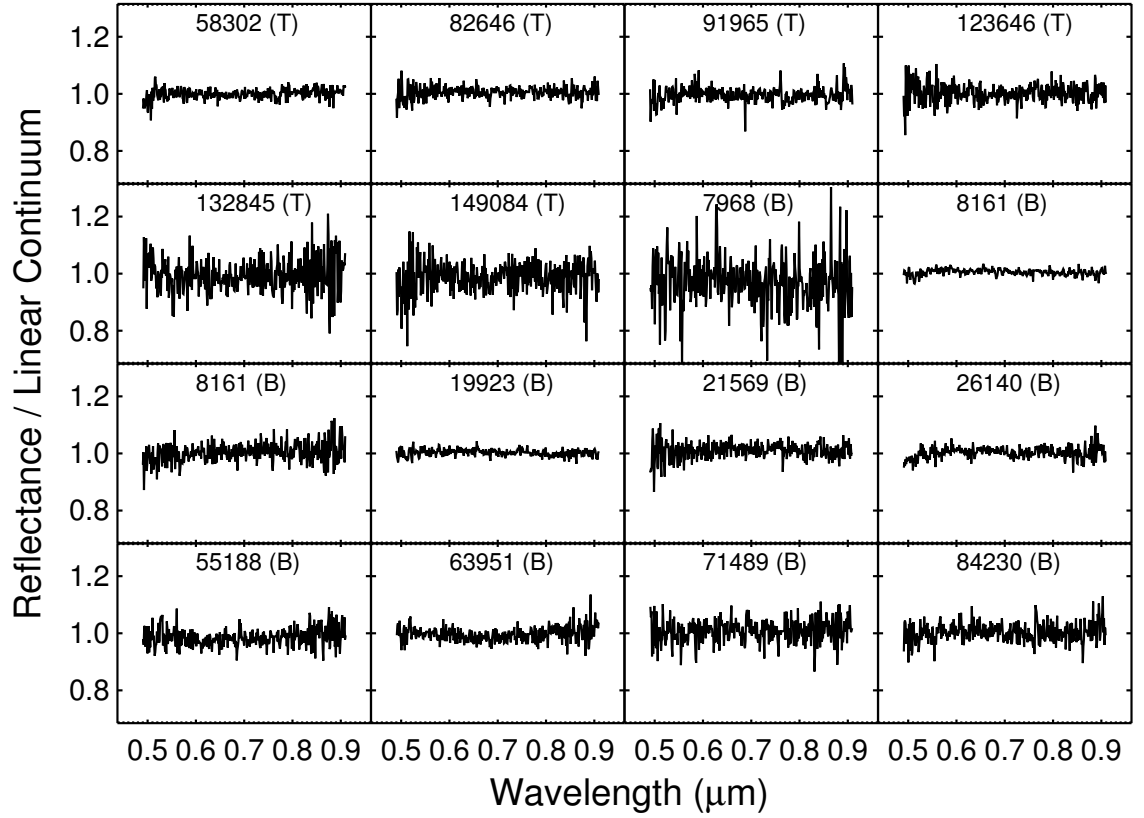


Figure 3.2 Continuum removed spectra of individual asteroids. Continuum removal was performed by dividing the full spectrum by a linear fit to 0.52-0.54 μm and 0.86-0.88 μm spectral regions. Labels show the asteroid ID as well as family membership, where (T) are Themis, (B) are Beagle family members.

for each family and size range are reported in Table 3.7. We use the SEM to quantify the variation in our estimate of the mean, and the standard deviation to quantify the dispersion in our slope and albedo distributions.

3.4 Results

Members of the Themis and Beagle families show a wide range of blue to red-sloped spectra (Figure 3.5). However, $\sim 90\%$ (21 out of 23) Beagle asteroids have blue-sloped spectra, whereas 60% (13 out of 22) of the Themis asteroids are blue-sloped. These data suggest

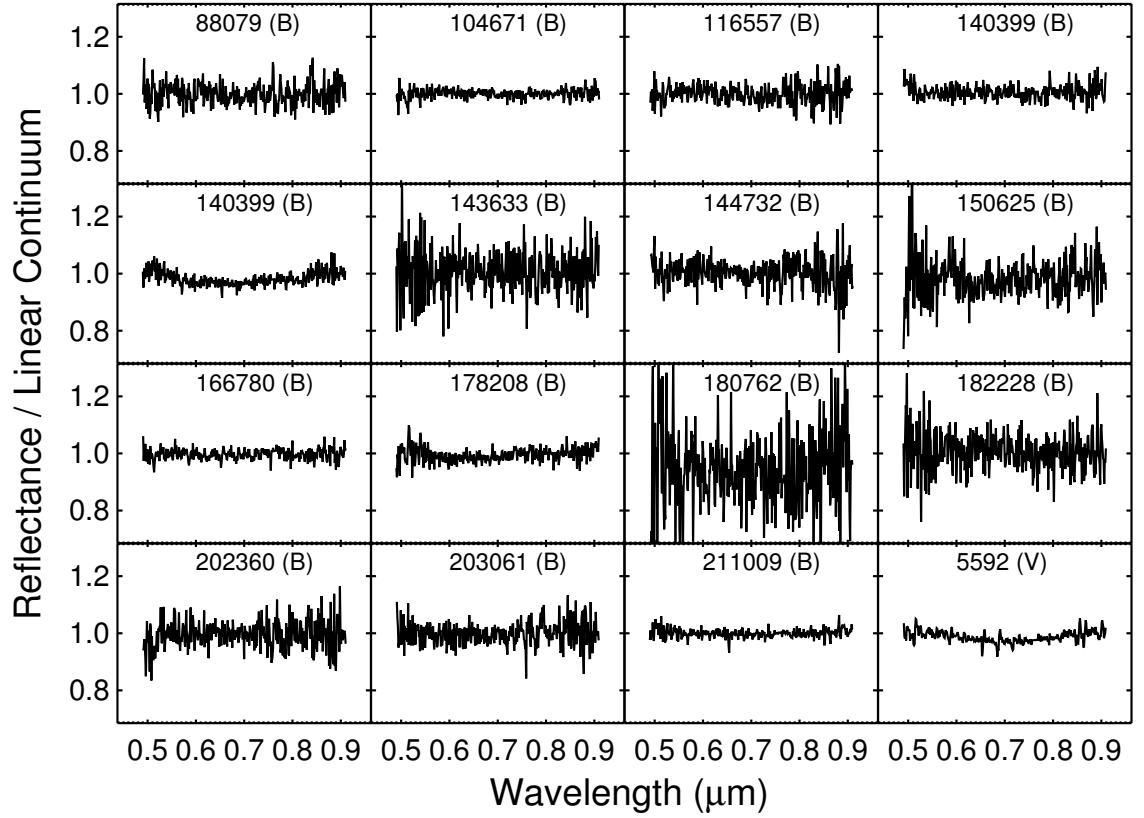


Figure 3.3 Continuum removed spectra of Beagle and Veritas asteroids. Continuum removal was performed by dividing the full spectrum by a linear fit to 0.52-0.54 μm and 0.86-0.88 μm spectral regions. Labels show the asteroid ID as well as family membership, where (B) are Beagle and (V) are Veritas family members.

the Beagle family is dominated by B-type asteroids, which are characterized by negatively (blue) sloped spectra (Tholen 1984; Bus & Binzel 2002a). The Themis asteroids show a range of C, B, F and G spectral types (Tholen 1984), consistent with the observations of other Themis members (Florczak et al. 1999).

3.4.1 Spectral Slopes

The slope distributions for the Themis and Beagle families are shown in Figure 3.5. Given the larger fraction of blue sloped spectra, the weighted mean for the Beagle asteroids ($-1.280 \pm 0.003\%$ per 1000 \AA) is significantly bluer than that of the Themis asteroids ($-0.378 \pm$

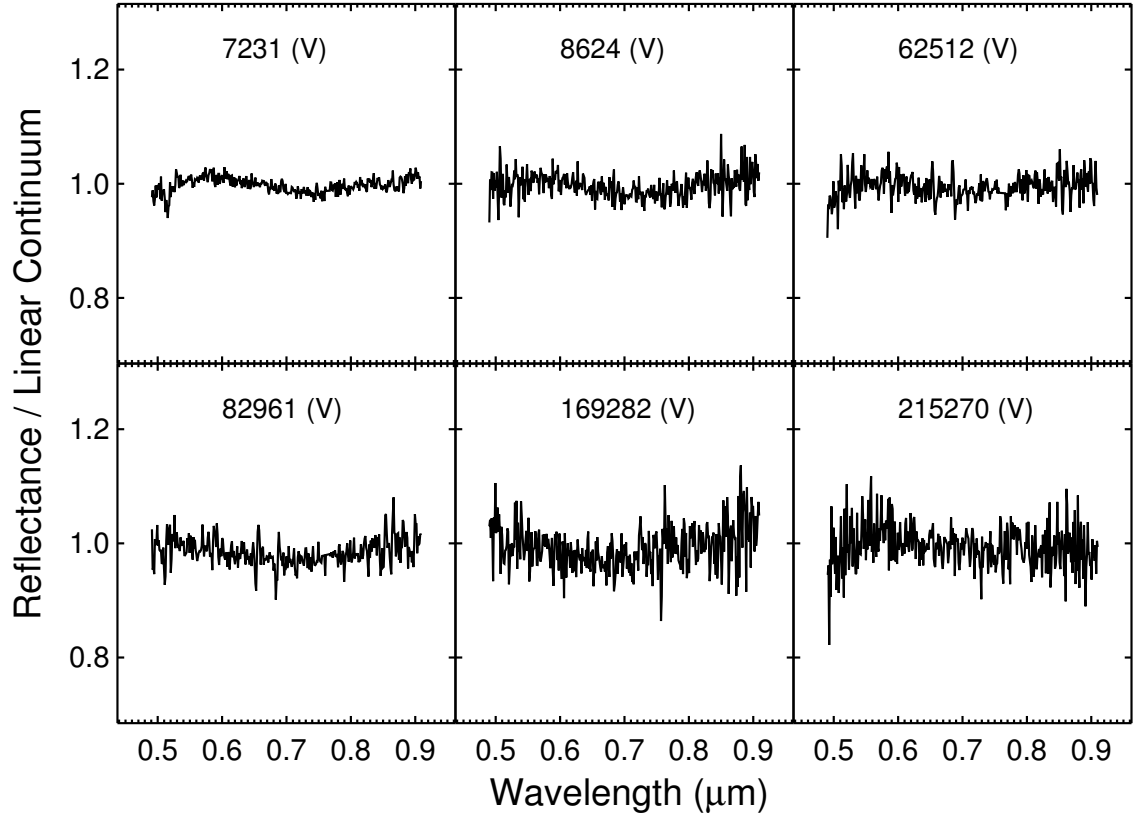


Figure 3.4 Continuum removed spectra of Veritas asteroids. Continuum removal was performed by dividing the full spectrum by a linear fit to 0.52-0.54 μm and 0.86-0.88 μm spectral regions. Labels show the asteroid ID as well as family membership, where (V) are Veritas family members.

0.003% per 1000 \AA). To test the significance of the difference in the slope distributions of the two families, we applied the Student's T and Kolmogorov-Smirnov (KS) tests to the Themis and Beagle data sets. We find the difference in means is significant at the 2-sigma level. One of the Themis asteroids, 18946, is extremely red ($3.037 \pm 0.005\%$ per 1000 \AA) so we applied the statistical tests with 18946 excluded. While the tests do show a slight drop in significance, the difference in the populations is still significant at the 2-sigma level.

The Beagle asteroids 140399 and 8161 were each observed on two nights and have significantly varied spectral slopes (Table 3.5). Both spectra of 140399 show the asteroid is moderately blue, however spectra of 8161 are both blue and red sloped. Both spectra were

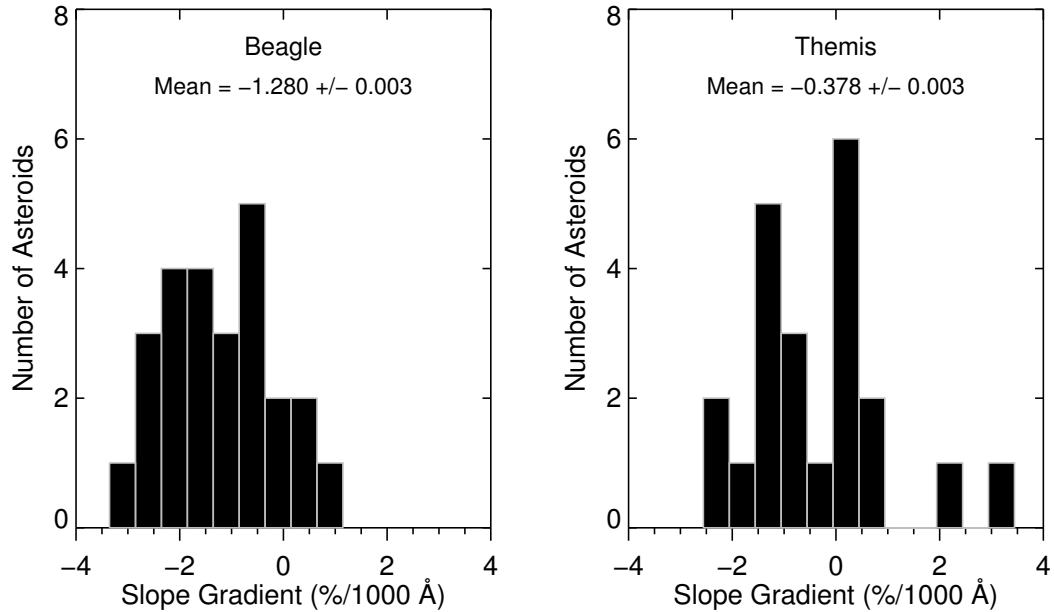


Figure 3.5 Spectral slope gradients (as defined by Jewitt & Meech 1986) for Themis and Beagle members. The weighted mean and standard error of the mean are reported.

taken during photometric conditions and produced using the same solar analog star, thus the large slope variation in asteroid 8161 may imply color differences across the surface of this asteroid. However, follow-up observations are needed to assess whether these trends can be reproduced.

3.4.2 Hydration Features

Several groups have noted a trend in the decreased frequency of phyllosilicate absorption features with decreasing asteroid diameter (Jones et al. 1990; Vilas & Sykes 1996; Howell et al. 2001; Florczak et al. 1999; Fornasier et al. 2014). Data from the SMASS II survey show a high fraction of hydrated members in the young (8.3 Myr) Veritas asteroid family (Bus & Binzel 2002b; Nesvorný et al. 2003), so we took spectra of 5 randomly selected small (< 10 km) and 2 moderately sized (~20 km) Veritas members to test if the 0.7 μm feature was observable on small diameter objects. We found 5 out of 7 (71%) asteroids less than

Table 3.4. Spectral Characteristics: Themis Family Asteroids

Asteroid ID	Hmag	D [†] (km)	Slope (% / 1000 Å)	S/N	UV [‡] Abs	0.7 μm [‡] Abs	0.7 μm [§] Detection Limit (%)	Obs [*] Run No.
7511	13.7	7.09	-0.896 ± 0.020	158.5	Y	N	0.6	3
8697	13.5	9.16	-2.165 ± 0.008	25.0	N	N	4.0	4
15572	13.4	8.12	0.088 ± 0.004	83.6	Y	N	1.2	3
15772	13.4	8.82	-1.917 ± 0.007	40.4	N	N	2.5	4
16877	13.6	9.19	-0.065 ± 0.010	62.5	N	N	1.6	4
18946	14.4	6.36	3.037 ± 0.005	37.0	N	N	2.7	1
26633	14.1	8.06	-0.025 ± 0.004	95.9	Y	N	1.0	3
28789	14.4	6.36	-0.900 ± 0.006	66.0	N	N	1.5	3
31093	13.4	9.43	0.293 ± 0.013	82.6	N	N	1.2	4
31334	13.6	10.18	0.631 ± 0.019	101.5	N	N	1.0	4
38365	14.1	7.79	2.209 ± 0.017	35.4	N	N	2.8	1
47920	13.4	11.25	0.437 ± 0.012	129.7	Y	N	0.8	3
51143	13.4	9.93	-1.083 ± 0.007	79.0	N	N	1.3	3
51579	14.2	6.01	0.807 ± 0.004	33.1	N	N	3.0	3
54320	14.4	7.02	-1.072 ± 0.015	124.0	N	N	0.8	3
58231	14.0	7.64	-1.426 ± 0.012	126.5	N	N	0.8	3
58302	14.2	6.91	-1.473 ± 0.004	71.9	N	N	1.4	1
82646	14.2	6.97	0.115 ± 0.007	50.5	N	N	2.0	4
91965	14.1	6.47	0.250 ± 0.005	55.2	N	N	1.8	1
123646	14.6	5.80	-2.557 ± 0.005	45.8	N	N	2.2	1
132845	15.3	4.24	-0.688 ± 0.007	21.2	N	N	4.7	3
149084	15.0	4.78	-1.161 ± 0.004	27.1	N	N	3.7	1

Note. — Spectral data of asteroids observed with Subaru telescope. H-magnitudes were obtained from (Milani et al. 2014). [†] Diameters (D) were computed using mean family albedos when diameter measurements were not available from WISE. [‡] Indication where absorption is seen in the spectrum either in the UV or at 0.7 μm . If visible, the 0.7 μm band depth is reported. [§] Detection limits were derived using the mean signal to noise of each spectrum. ^{*} Observing runs 1, 2, 3, and 4 correspond Mar. 02, 2013, Oct. 29, 2013, Oct. 30, 2013, and Feb. 21, 2014 respectively.

Table 3.5. Spectral Characteristics: Beagle Family Asteroids

Asteroid ID	Hmag	D [†] (km)	Slope (% / 1000 Å)	S/N	UV [‡] Abs	0.7 μm [‡] Abs	0.7 μm [§] Detection Limit (%)	Obs* Run No.
7968	15.6	4.87	-1.132 ± 0.004	13.5	N	N	7.4	3
8161	13.3	10.51	-1.787 ± 0.004	99.3	N	N	1.0	2
			0.964 ± 0.010	31.2	N	N	3.2	4
19923	13.8	8.08	-0.128 ± 0.008	85.3	N	N	1.2	4
21569	13.9	13.65	0.455 ± 0.015	55.5	N	N	1.8	1
26140	14.1	7.83	0.418 ± 0.004	54.0	N	N	1.9	3
55188	13.6	8.69	-1.924 ± 0.002	32.9	N	N	3.0	2
63951	15.0	5.54	-1.664 ± 0.003	39.6	N	N	2.5	3
71489	13.8	8.13	-0.242 ± 0.003	28.2	N	N	3.5	3
84230	15.1	5.49	-2.572 ± 0.005	32.2	N	N	3.1	3
88079	14.9	5.49	-3.353 ± 0.005	35.6	N	N	2.8	1
104671	15.4	4.36	-1.261 ± 0.003	55.0	N	N	1.8	2
116557	15.2	4.30	-0.810 ± 0.005	33.0	N	N	3.0	3
140399	14.6	6.39	-1.555 ± 0.003	40.7	N	N	2.5	3
			-2.340 ± 0.012	55.8	N	3.4 ± 1.3	1.8	4
143633	15.7	3.53	-0.423 ± 0.011	14.9	N	N	6.7	4
144732	15.6	3.70	-1.082 ± 0.003	17.9	N	N	5.6	2
150625	16.1	3.26	-2.444 ± 0.009	22.0	N	N	4.5	1
166780	15.7	4.09	-2.506 ± 0.004	58.5	N	N	1.7	2
178208	15.6	4.34	-1.895 ± 0.008	41.6	N	N	2.4	4
180762	15.5	3.29	-1.379 ± 0.013	10.8	N	N	9.3	1
182228	15.6	4.34	-0.710 ± 0.008	23.4	N	N	4.3	1
202360	15.6	3.57	-0.469 ± 0.003	21.3	N	N	4.7	2
203061	16.3	3.02	-0.363 ± 0.007	26.3	N	N	3.8	3
211009	15.7	3.98	-2.058 ± 0.010	70.9	N	N	1.4	4

Note. — Spectral data of asteroids observed with Subaru telescope. H-magnitudes were obtained from (Milani et al. 2014). [†] Diameters (D) were computed using mean family albedos when diameter measurements were not available from WISE. [‡] Indication where absorption is seen in the spectrum either in the UV or at 0.7 μm. If visible, the 0.7 μm band depth is reported. [§] Detection limits were derived using the mean signal to noise of each spectrum. * Observing runs 1, 2, 3, and 4 correspond Mar. 02, 2013, Oct. 29, 2013, Oct. 30, 2013, and Feb. 21, 2014 respectively.

Table 3.6. Spectral Characteristics: Veritas Family Asteroids

Asteroid ID	Hmag	D [†] (km)	Slope (% / 1000 Å)	S/N	UV [‡] Abs	0.7 μm [‡] Abs	0.7 μm [§] Detection Limit (%)	Obs* Run No.
5592	11.7	22.09	-1.366 ± 0.011	111.4	N	3.0 ± 0.7	0.9	3
7231	12.2	18.33	-0.588 ± 0.007	103.9	Y	1.1 ± 0.8	1.0	3
8624	13.6	9.50	0.167 ± 0.002	49.9	N	N	2.0	4
62512	14.7	5.76	1.211 ± 0.013	73.8	Y	1.4 ± 1.1	1.3	4
82961	14.1	6.93	-2.582 ± 0.010	65.7	N	3.0 ± 1.2	1.5	3
169282	14.6	6.27	-0.704 ± 0.006	26.9	N	N	3.7	4
215270	15.1	5.34	1.411 ± 0.002	30.2	N	N	3.3	2

Note. — Spectral data of asteroids observed with Subaru telescope. H-magnitudes were obtained from (Milani et al. 2014). [†] Diameters (D) were computed using mean family albedos when diameter measurements were not available from WISE. [‡] Indication where absorption is seen in the spectrum either in the UV or at 0.7 μm . If visible, the 0.7 μm band depth is reported. [§] Detection limits were derived using the mean signal to noise of each spectrum. * Observing runs 1, 2, 3, and 4 correspond Mar. 02, 2013, Oct. 29, 2013, Oct. 30, 2013, and Feb. 21, 2014 respectively.

25 km in diameter show the 0.7 μm feature. Although asteroid 169282 does not pass our detection criteria (the depth of the band is smaller than than SNR value), visual inspection of the spectrum (Fig. 3.4) does suggest the feature is present. Approximately ~ 4 out of 5 members ($\sim 80\%$) with diameters less than 15 km show the 0.7 μm feature, suggesting that despite the lack of phyllosilicate features on small objects, we should detect the features on our small diameter Themis and Beagle asteroids if phyllosilicates are present.

However, only one Beagle (140399) and no Themis asteroids show the feature. It is important to note that asteroid 140399 was imaged on two separate observing runs and only one of the spectra (Fig. 3.2) shows the absorption. Despite the lack of 0.7 μm features in the Themis members, a small number of objects (4 of 22, or 18%) show evidence of the Fe^{2+} UV absorption band also attributed to phyllosilicates (Vilas 1994). A similarly small fraction (3 of 23, or 13%) of the Beagle asteroids also show this UV feature. Due to the cutoff in the spectral coverage below 0.47 μm , we did not attempt to fit the Fe^{2+} UV feature, but its presence was assessed through visual inspection. Tables 3.4-3.6 show which asteroids were flagged as showing the UV and 0.7 μm features.

Table 3.7. Summary of Asteroid Family Slope and Albedo Distributions

Family	Slope %/1000 Å	σ_{slope}	Albedo (< 15 km)	σ_{albedo}	Albedo (≥ 15 km)	σ_{albedo}
Beagle	-1.280 ± 0.003	1.080	0.0794 ± 0.0045	0.0179	—	—
Themis	-0.378 ± 0.003	1.342	0.0680 ± 0.0006	0.0236	0.0747 ± 0.0013	0.0214
Veritas	0.196 ± 0.001	1.532	0.0695 ± 0.0010	0.0245	0.0619 ± 0.0064	0.0255

Note. — Slopes represent weighted means for each family, and albedo means were derived from reported WISE values (Masiero et al. 2011). The uncertainty reported with the means are the standard error of the mean. The sigma values represent the standard deviation and show the dispersion for each population.

3.4.3 Albedo Variations

Figure 3.6 shows the WISE albedo distributions as function of diameter for both the small (≤ 15 km) and large (> 15 km) asteroid populations in each family. The WISE survey sensitivity is strongly dependent on the distance and diameters of surveyed asteroids. As Beagle and Themis members have nearly identical orbital elements, the detection sensitivity in our analyses is limited to asteroid diameters. Therefore, due to the small size range of the Beagle asteroids, we limit the comparison between the three families to those objects with diameters less than 15 km. Figure 3.7 shows the distribution of albedos for the Beagle family. In comparison, the <15 km population of Themis asteroids ($p_v = 0.068 \pm 0.001$) have a lower average albedo than the Beagle asteroids ($p_v = 0.079 \pm 0.005$). Unexpectedly, the Veritas asteroids, which are similar in age to the Beagle family, have albedos ($p_v = 0.069 \pm 0.001$) similar to the older Themis asteroids. In addition, the two size populations of the Themis asteroids show significantly different albedos (Fig. 3.8), where on average the larger members are brighter than the smaller members. The Veritas asteroids also show a slight difference in albedo difference between small and large members (Fig. 3.9), however the difference is not statistically significant.

For comparison between our results and Masiero et al. (2013), we fit gaussian profiles to the log distributions of the three families. The distributions in log space are shown in

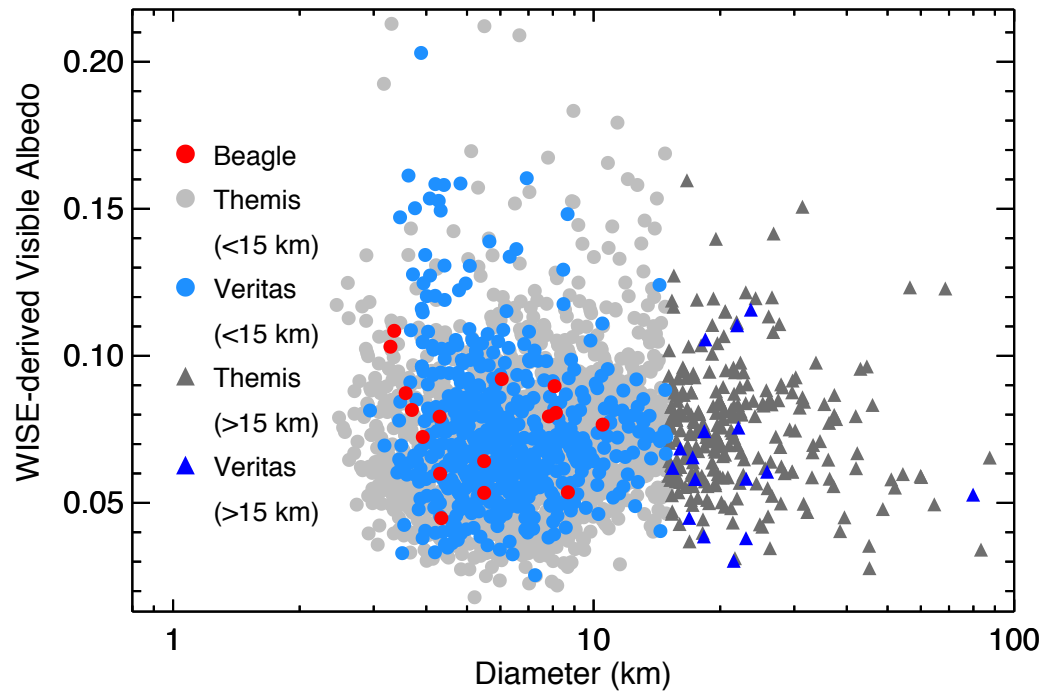


Figure 3.6 WISE albedo versus diameter distributions for Beagle, Themis and Veritas asteroid families.

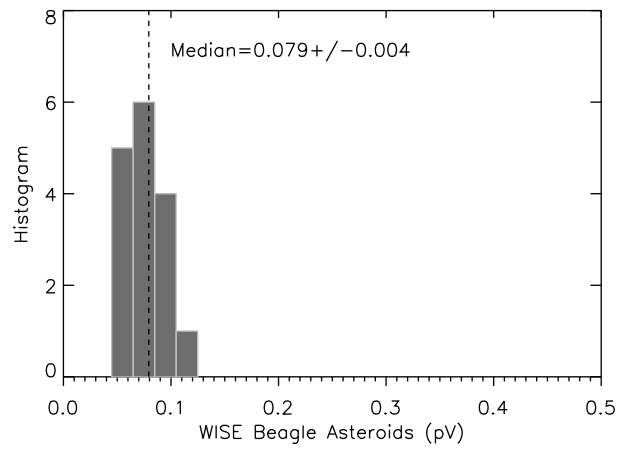


Figure 3.7 WISE albedo distributions for the Beagle asteroids. The median and associated standard error are reported.

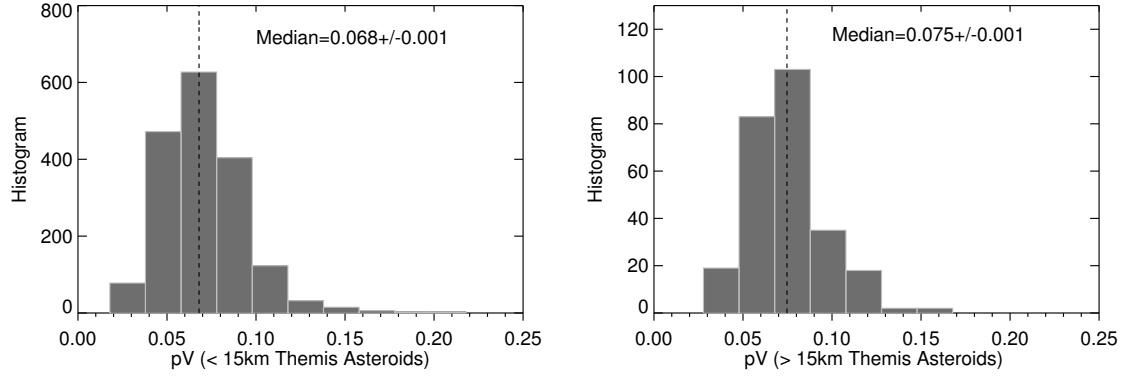


Figure 3.8 WISE derived albedo distributions for Themis asteroids with diameters less than and greater than 15 km (Masiero et al. 2011). Fifteen kilometers is the approximate size of the largest Beagle member when excluding 656 Beagle (Nesvorný et al. 2008). The median and associated standard error are reported.

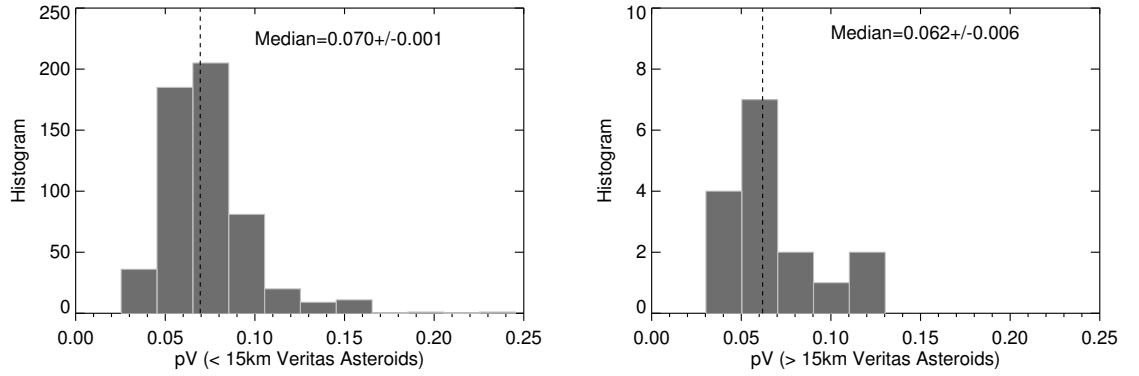


Figure 3.9 WISE derived albedo distributions for Veritas asteroids with diameters less than and greater than 15 km (Masiero et al. 2011). Fifteen kilometers is the approximate size of the largest Beagle member when excluding 656 Beagle (Nesvorný et al. 2008). The median and associated standard error are reported.

Figure 3.10. We find that our gaussian means are consistent with the values derived Masiero et al. (2013). When comparing the gaussian medians with the true sample distribution, we find the gaussian values are slightly larger than the means of the sample population. The difference in means implies the true population does not follow a gaussian distribution. The apparent non-gaussian distribution is likely dominated by a bias introduced when

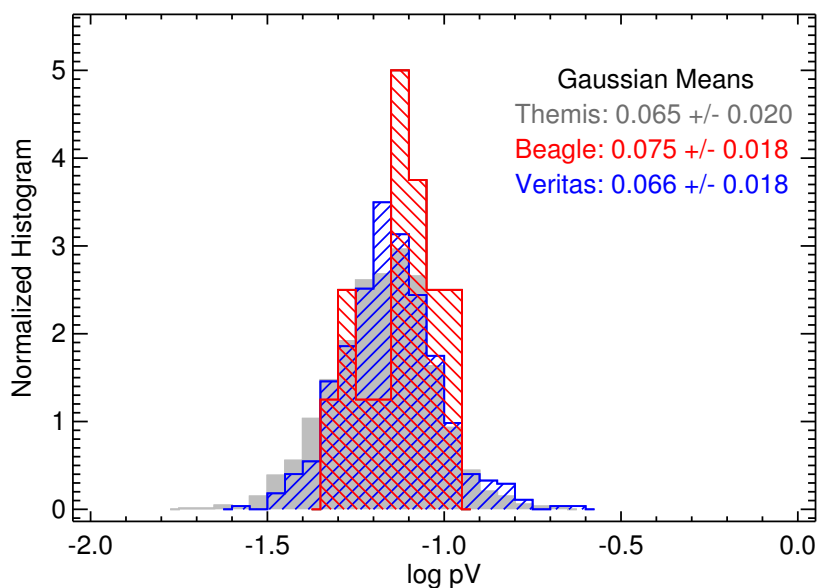


Figure 3.10 Log plot of WISE albedo (p_v) distributions for Themis, Beagles and Veritas asteroids < 15 km in size. Each histogram has been normalized to unit area for comparison. Gaussian mean and widths are reported for each family.

using previously published absolute magnitudes to derive the albedos from WISE asteroid diameters (Masiero et al. 2013).

3.5 Discussion

Spectral characteristics such as slopes and absorption features are some of the tools available for assessing asteroid compositions remotely. However, the abundance of the absorber, the size distribution of regolith grains (Clark 1999), and space weathering processes (Conel & Nash 1970; Gold et al. 1970; Hapke et al. 1970) all greatly influence the slope and absorption features of asteroid spectra. Although these processes and characteristics are difficult to disentangle when analyzing spectroscopic data, the sensitivity of spectroscopy to these processes also allows spectral characteristics to be a powerful remote sensing tool.

3.5.1 C-type Space Weathering Trends

As seen in Figure 3.5, the older Themis asteroids have distinctly redder slopes as compared to the younger Beagle asteroids. This difference implies the spectral slopes of C-complex asteroids become redder over time, which is consistent with the trends observed by Lazzarin et al. (2006). Although the slope evolution of C-complex asteroids appears consistent with silicate-rich S-complex asteroids (Nesvorný et al. 2005; Lazzarin et al. 2006), the albedo trends are not.

Masiero et al. (2011) find the younger Karin family has a lower albedo than the older Koronis family. In contrast to Karin and Koronis, our data suggest the younger Beagle asteroids have a higher albedo than the older Themis asteroids. The albedo and slope data of Themis and Beagle suggest space weathering of C-complex asteroids is consistent with classical space weathering models where atmosphereless bodies darken and redden with age (Chapman 2004, and references within). The albedo trends among the small and large Themis asteroids suggest diameter may play a significant role in the albedo evolution of asteroids. The size distribution of Koronis is peculiar in that the family has sharp cutoff in objects larger than 45 km (Marzari et al. 1995), so future work is necessary to assess whether size related trends are influencing the albedo differences between the Koronis and Karin families.

3.5.2 Regolith Effects on Spectral Characteristics

Due to their lower escape velocities, small asteroids are thought to develop relatively thin regoliths dominated by coarse grains as they are unable to retain fine particles during collisions. Scaling gravitational effects to large diameters asteroids suggests larger asteroids will have thicker regoliths with fine grains in addition to coarse grains (Matson et al. 1977). Laboratory data show the optical effects of particle size on albedo and absorption features. Increasing grain size results in decreased reflectance or albedo (Fischer et al. 1994; Clark 1999; Cloutis et al. 2011a,b). In addition, Fischer et al. (1994) and Clark (1999) find the most prominent absorption bands are seen in fine grain samples. Thus we propose the

albedo and absorption feature trends in our small and large Themis asteroid populations originate from differences in sized related regolith properties (thickness and particle size).

Thin regoliths on small asteroids (Chapman 2004) are predicted to experience regolith overturn more quickly (Willman et al. 2010), thus small asteroids likely reach optical maturity (in terms of space weathering) faster than large asteroids (Chapman 2004). The faster optical maturity and/or the coarse regolith grains of small asteroids would both result in a reduction of absorption features and decreased albedo relative to large asteroids. Indeed, size related trends in phyllosilicate absorption features have been noted in the Themis asteroids, with $\sim 60\%$ of asteroids greater than 50 km showing the feature in comparison to 35% for objects less than 50 km. (Florczak et al. 1999). In addition, the lower albedos of the small Themis asteroids as compared to the large asteroids suggest the Themis asteroid spectra are greatly influenced by regolith properties.

The relatively young ages of the Veritas and Beagle asteroids suggest they have minimally evolved regoliths, yet the <15 km diameter Veritas asteroids show a much higher fraction of hydrated members than the Beagle asteroids. In addition, the Veritas asteroid albedos are lower than the Beagle asteroids and more closely resemble the Themis asteroids. These data imply a significant difference in the composition between Veritas and Themis/Beagle families and that the color differences observed by (Nesvorný et al. 2005) is likely a product of mineralogy rather than space weathering trends.

The effects of regolith thickness and grain size on spectral slopes are difficult to assess. Assuming slopes decrease with increasing grain size as laboratory data have suggested (Fischer et al. 1994; Cloutis et al. 2011a), small asteroids with regoliths dominated by coarse grains would have bluer spectral slopes than large asteroids. However, the thin regoliths of small asteroids space weather more quickly, suggesting the slopes will be redder than large asteroids. The relative contribution of particle size and space weathering trends on slope trends is therefore more complex than albedo and absorption feature trends and beyond the scope of this thesis.

3.5.3 Aqueous Alteration in the Themis Parent Body

Several main-belt comets (MBCs; Hsieh et al. 2006) have been dynamically linked to the Themis family (Hsieh 2009; Novaković et al. 2012). The source of sublimation in these MBCs is attributed to water ice buried beneath a layer of regolith several meters thick (Schorghofer 2008; Prialnik & Rosenberg 2009). Thermal evolution models suggest the Themis/Beagle parent body was likely differentiated, with aqueous alteration taking place predominantly in the core, thus allowing the preservation of an icy shell near the surface (Castillo-Rogez & Schmidt 2010; Grimm & McSween 1989; Cohen & Coker 2000).

Due to the young age of the Beagle family and the small fraction of hydrated Beagle members, we believe that the low frequency of features represents an intrinsically low phyllosilicate content in the Beagle parent body. The detection of phyllosilicates in the Beagle asteroids has important implications for geophysical models of the Themis/Beagle parent body, especially because MBC 133P is a member of the Beagle family (Nesvorný et al. 2008). The association with 133P implies the Beagle parent body originated from an ice-rich layer in Themis/Beagle parent body. However, the small but notable fraction of members with the UV and $0.7\ \mu\text{m}$ features suggest the Beagle parent body was not homogeneous, but rather a mixture of ice and aqueously altered material.

We propose two possibilities for heterogeneity of the Beagle parent body. The first is that heterogeneity may represent non-uniform alteration of the Themis/Beagle parent body. Conversely, Rivkin & Emery (2010) and Campins et al. (2010) have detected possible water ice features on the largest member of the family, 24 Themis. Castillo-Rogez & Schmidt (2010) propose this object is the remnant core onto which components from an icy crust reaccreted post-collisional disruption of the parent body. Therefore, our second hypothesis is that the Beagle parent body may be another object which reaccreted non-native components, resulting in the present heterogeneity of the Beagle asteroids. Exploring the viability of these two scenarios is beyond the scope of this thesis, but coupled geophysical and dynamical modeling of the two families may provide valuable insight into the evolution of this body.

3.6 Summary

Through comparison of visible spectra and albedo data of the Themis and Beagle asteroids, we find the following:

1. Space weathering results in an increase of spectral slopes and a decrease in albedo among C-complex asteroids.
2. The apparent mineralogical differences between the Veritas, and the Themis and Beagle families highlights the importance of accounting for mineralogy when interpreting space weathering trends across the broad C-complex asteroids.
3. The notable fraction of Beagle members with phyllosilicate features indicate the Beagle parent was a heterogeneous mixture of ice and aqueously altered minerals.
4. Trends in decreased phyllosilicate features with decreasing diameter likely result from variations in regolith properties as a function of age and diameter.

Comparison of the albedo and spectral trends in the Beagle and Themis asteroids show C-complex asteroids experience slope reddening and darkening in response to space weathering.

References

- Bus, S. J. & Binzel, R. P. 2002a, *Icarus*, 158, 146
- Bus, S. J. & Binzel, R. P. 2002b, *Icarus*, 158, 106
- Campins, H., Hargrove, K., Pinilla-Alonso, N., Howell, E. S., Kelley, M. S., Licandro, J., Mothé-Diniz, T., Fernández, Y., & Ziffer, J. 2010, *Nature*, 464, 1320
- Castillo-Rogez, J. C. & Schmidt, B. E. 2010, *Geophys. Res. Lett.*, 37, L10202
- Chapman, C. R. 2004, *Annual Review of Earth and Planetary Sciences*, 32, 539
- Clark, B. E., Hapke, B., Pieters, C., & Britt, D. 2002, *Asteroids III*, 585
- Clark, R. N. 1999, *Manual of Remote Sensing, Volume 3, Remote Sensing for the Earth Sciences*, ed. A. Rencz, Vol. 3 (John Wiley and Sons), 3–58
- Cloutis, E. A., Hiroi, T., Gaffey, M. J., Alexander, C. M. O. ., & Mann, P. 2011a, *Icarus*, 212, 180
- Cloutis, E. A., Hudon, P., Hiroi, T., Gaffey, M. J., & Mann, P. 2011b, *Icarus*, 216, 309
- Cohen, B. A. & Coker, R. F. 2000, *Icarus*, 145, 369
- Conel, J. E. & Nash, D. B. 1970, *Geochimica et Cosmochimica Acta Supplement*, 1, 2013
- Fischer, E. M., Pieters, C. M., & Pratt, S. F. 1994, in *Lunar and Planetary Science Conference*, Vol. 25, *Lunar and Planetary Science Conference*, 371

- Florczak, M., Lazzaro, D., Mothé-Diniz, T., Angeli, C. A., & Betzler, A. S. 1999, *A&AS*, 134, 463
- Fornasier, S., Lantz, C., Barucci, M. A., & Lazzarin, M. 2014, *Icarus*, 233, 163
- Gold, T., Campbell, M. J., & O’Leary, B. T. 1970, *Geochimica et Cosmochimica Acta* Supplement, 1, 2149
- Grimm, R. E. & McSween, Jr., H. Y. 1989, *Icarus*, 82, 244
- Hapke, B. 2001, *J. Geophys. Res.*, 106, 10039
- Hapke, B. W., Cohen, A. J., Cassidy, W. A., & Wells, E. N. 1970, *Geochimica et Cosmochimica Acta* Supplement, 1, 2199
- Hirayama, K. 1918, *AJ*, 31, 185
- Hiroi, T., Zolensky, M. E., Pieters, C. M., & Lipschutz, M. E. 1996, *Meteoritics and Planetary Science*, 31, 321
- Howell, E. S., Rivkin, A. S., Vilas, F., & Soderberg, A. M. 2001, in *Lunar and Planetary Science Conference*, Vol. 32, *Lunar and Planetary Science Conference*, 2058
- Hsieh, H. H. 2009, *A&A*, 505, 1297
- Hsieh, H. H., Jewitt, D., & Pittichova, J. 2006, *IAU Circ.*, 8704, 3
- Jewitt, D. & Meech, K. J. 1986, *ApJ*, 310, 937
- Jones, T. D., Lebofsky, L. A., Lewis, J. S., & Marley, M. S. 1990, *Icarus*, 88, 172
- Kashikawa, N., Aoki, K., Asai, R., Ebizuka, N., Inata, M., Iye, M., Kawabata, K. S., Kosugi, G., Ohyama, Y., Okita, K., Ozawa, T., Saito, Y., Sasaki, T., Sekiguchi, K., Shimizu, Y., Taguchi, H., Takata, T., Yadoumaru, Y., & Yoshida, M. 2002, *PASJ*, 54, 819
- Lazzarin, M., Marchi, S., Moroz, L. V., Brunetto, R., Magrin, S., Paolicchi, P., & Strazzulla, G. 2006, *ApJ*, 647, L179

- Marzari, F., Davis, D., & Vanzani, V. 1995, *Icarus*, 113, 168
- Masiero, J. R., Mainzer, A. K., Bauer, J. M., Grav, T., Nugent, C. R., & Stevenson, R. 2013, *ApJ*, 770, 7
- Masiero, J. R., Mainzer, A. K., Grav, T., Bauer, J. M., Cutri, R. M., Dailey, J., Eisenhardt, P. R. M., McMillan, R. S., Spahr, T. B., Skrutskie, M. F., Tholen, D., Walker, R. G., Wright, E. L., DeBaun, E., Elsbury, D., Gautier, IV, T., Gomillion, S., & Wilkins, A. 2011, *ApJ*, 741, 68
- Matson, D. L., Johnson, T. V., & Veeder, G. J. 1977, in *Lunar and Planetary Inst. Technical Report*, Vol. 8, Lunar and Planetary Science Conference, 625
- Milani, A., Cellino, A., Knežević, Z., Novaković, B., Spoto, F., & Paolicchi, P. 2014, *Icarus*, 239, 46
- Moroz, L. V., Fisenko, A. V., Semjonova, L. F., Pieters, C. M., & Korotaeva, N. N. 1996, *Icarus*, 122, 366
- Nesvorný, D. 2012, *NASA Planetary Data System*, 189
- Nesvorný, D., Bottke, W. F., Dones, L., & Levison, H. F. 2002, *Nature*, 417, 720
- Nesvorný, D., Bottke, W. F., Levison, H. F., & Dones, L. 2003, *ApJ*, 591, 486
- Nesvorný, D., Bottke, W. F., Vokrouhlický, D., Sykes, M., Lien, D. J., & Stansberry, J. 2008, *ApJ*, 679, L143
- Nesvorný, D., Jedicke, R., Whiteley, R. J., & Ivezić, Ž. 2005, *Icarus*, 173, 132
- Novaković, B., Hsieh, H. H., & Cellino, A. 2012, *MNRAS*, 424, 1432
- Prialnik, D. & Rosenberg, E. D. 2009, *MNRAS*, 399, L79
- Rivkin, A. S. & Emery, J. P. 2010, *Nature*, 464, 1322
- Ryan, E. L. & Woodward, C. E. 2010, *AJ*, 140, 933

Schorghofer, N. 2008, ApJ, 682, 697

Tholen, D. J. 1984, PhD thesis, University of Arizona, Tucson

Tody, D. 1986, in Society of Photo-Optical Instrumentation Engineers (SPIE) Conference Series, Vol. 627, Instrumentation in astronomy VI, ed. D. L. Crawford, 733

Vilas, F. 1994, Icarus, 111, 456

Vilas, F. & Sykes, M. V. 1996, Icarus, 124, 483

Willman, M., Jedicke, R., Moskovitz, N., Nesvorny, D., Vokrouhlicky, D., & Mothé-Diniz, T. 2010, in Bulletin of the American Astronomical Society, Vol. 42, AAS/Division for Planetary Sciences Meeting Abstracts #42, 1034

Chapter 4

Visible/Near-Infrared Color Trends in the Themis and Beagle Asteroid Families

4.1 Introduction

Space weathering processes, which modify an airless body's surface with time, reduce our ability to accurately assess the mineralogy of asteroids and match them with meteorite analogs (Chapman 2004). Therefore, it is critical to understand how space weathering processes affect asteroid spectra, and infer which wavelengths and absorption features are most affected in order to interpret observations. Through this process of determining which features are most affected, we can also determine which features are the most reliable for assessing the mineralogies and compositions of asteroid parent bodies.

The majority of observational studies looking at space weathering processes on asteroids have focused on visible wavelength data (Jedicke et al. 2004; Nesvorný et al. 2005; Lazzarin et al. 2006). However Chapman et al. (2009) use NIR spectra to study young and old S-complex asteroids and find a slight increase in spectral slope with age. In contrast, NIR spectra of the young (8.3 Myr; Nesvorný et al. 2003) C-complex Veritas asteroids exhibit inverted U-shaped spectra whereas the older (2.3 Gyr; Marzari et al. 1995) Themis asteroids show U-shaped (which we will refer to as concave) spectra. Assuming Themis and Veritas have similar compositions, Chapman et al. (2009) proposes space weathering trends in the NIR wavelengths may be more dominant for C-complex rather than S-complex asteroids.

The Beagle asteroids are an asteroid family that originated from the recent (<10 Myr ago (Nesvorný et al. 2008) collisional disruption of a member of the older (2.3 Gyr old; Marzari et al. 1995) C-complex Themis asteroid family. Therefore these two young and old families provide a unique tool to probe the space weathering processes among C-complex asteroids while minimizing the effects of composition. In Chapter 3, we use visible spectroscopic data of these two families to show that the Themis asteroids have significantly redder slopes than the Beagle asteroids. Our aim in this chapter is to search for differences in visible and NIR colors for Themis and Beagle asteroids to assess if C-complex asteroids with similar compositions are affected by space weathering in the NIR wavelengths.

4.2 Observations

We present simultaneous visible and NIR broadband photometry for 23 main-belt asteroids belonging to the Themis, Beagle and Veritas asteroid families. Observations took place on 10 (partial and full) nights during Feb. 10, 11, 12, 13 and 15, Aug. 29, 30, 31 and Sep. 20 and 27, 2013 at the 3.0-meter NASA InfraRed Telescope Facility (IRTF) on Maunakea, Hawai'i.

Near-infrared data were obtained with Guidedog, the SpeX instrument guider camera. The Guidedog detector is a 512×512 Aladdin 2 InSb CCD array with a gain of 14.7 e-/ADU. The chip is read multiple times during integration, a process called non-destructive reads (NDRs), however the number of NDRs is dependent upon the integration time. For a single NDR, the read noise is 60 e- RMS, but decreases by approximately $\text{NDR}^{-0.5}$ as integration time is increased, with a maximum of 32 NDRs (Rayner et al. 2004).

Visible broadband images were taken with the MIT Optical Rapid Imaging System (MORIS) (Gulbis et al. 2011). MORIS is mounted on the exit window of the SpeX instrument, allowing for simultaneous visible and NIR observations. The camera has a $0.114''/\text{pixel}$ scale and $60''$ field of view. MORIS data are recorded on a 512×512 pixel E2V CCD detector, which has two analog-to-digital converters (ADC). Our observations utilized

the 16-bit ADC with a 1 MHz readout rate, resulting in a read noise and gain of 8.58 e- and 3.70 e-/ADU. Biases and flat field images were obtained for MORIS data using twilight sky images at the beginning or end of the observing runs.

MORIS and Guidedog were used together to obtain simultaneous visible and NIR broadband data for each of our targets. Therefore, each J ($\lambda_{center} \sim 1.25 \mu\text{m}$), H ($\lambda_{center} \sim 1.64 \mu\text{m}$) and K ($\lambda_{center} \sim 2.15 \mu\text{m}$) near-infrared image has a corresponding SDSS r' -band ($\lambda_{center} \sim 0.62 \mu\text{m}$) image. We used a 5-point dither script to get 5 images per filter set. The telescope was dithered between exposures to allow for sky background removal in the NIR images. Non-sidereal guiding was used during asteroid observations and exposures were limited to ~ 180 -250 seconds to avoid saturation in the NIR exposures due to sky brightness. Themis targets were limited to members with similar diameters as Beagle targets (≤ 15 km) to avoid potential size related variations (Florczak et al. 1999; Fornasier et al. 2014). Family membership was based upon dynamically derived membership lists from Nesvorný (2012). Diameters were taken from the Wide-field Infrared Survey (WISE) and when no diameters were available, they were derived using the average albedo of the associated family (Masiero et al. 2011). In addition to the asteroid observations, solar analog stars were imaged at airmasses similar to those of the asteroids. The asteroids and corresponding solar analog stars are shown in Table 4.1.

4.3 Data Reduction and Analysis

Prior to any processing, both MORIS and Guidedog images were divided by the number of co-adds and/or NDRs to convert each image to counts that correspond to the exposure times in the headers. Median combined bias and flat field images were made for the MORIS data, and bias subtraction and flattening were performed using the Image Reduction and Analysis Facility (IRAF) V2.14 `noao` ccdred package.

Photometry was performed with the IRAF `noao` phot package. Phot was used interactively to measure the total flux within user defined apertures (1 to 5" in radius).

Sky correction was performed by measuring the flux in an annulus around or near our target. Due to the faintness of our targets (due to their small diameters) and the low S/N compared to the sky brightness, asteroids were only visible in the NIR images after the images were background subtracted. Therefore our photometry measurements in the NIR bands were performed on the background subtracted images. IRAF computes error estimates using the following equation:

$$\sigma_{flux} = \sqrt{\frac{flux}{gain} + area \times stdev^2 + \frac{area^2 \times stdev^2}{nsky}} \quad (4.1)$$

where flux is the total number of counts excluding sky; area is the area of the asteroid/star aperture; stdev is the standard deviation in the sky annulus and nsky is the number of sky pixels.

Extinction correction was performed on each measurement using average Maunakea values of $k_J=0.015$, $k_H=0.015$ and $k_K=0.033$ magnitudes/airmass (Tokunaga et al. 2002), and the r' coefficient was $k_{r'}=0.11$ (Jørgensen 2009). For each object, we use weighted means to derive the averaged flux, standard deviation and standard error for each filter. The averaged asteroid fluxes were divided by nearby G2V solar analog fluxes to produce reflectance values in each band. Because our r' -band observations were always simultaneous with J, H and K-band observations, we were able to remove any brightness variations caused by the changing rotational cross section. Therefore 4-color spectra were derived by normalizing each NIR band to the corresponding r-band value. Colors were derived for each asteroid using Equation 4.2

$$A - B = -2.5 \log_{10}(R_A/R_B) \quad (4.2)$$

where A and B correspond to first and second filter, and R_A and R_B are the normalized asteroid reflectance values. It is important to note that this formulation produces color indices where the solar colors have been removed. The r' -J, J-H, J-K and H-K colors for each asteroid are reported in Tables 4.2 and 4.3.

We combined our data with previously published colors to assess how the Themis and Beagle color indices compare to other small solar system bodies (Hartmann et al. 1982; Delsanti et al. 2006; Emery et al. 2011). Prior to combining the data sets, the solar colors needed to be removed from the comet and asteroid measurements of Hartmann et al. (1982), and the centaur and Kuiper Belt object (KBO) measurements of Delsanti et al. (2006). For this correction, we adopted the solar colors of Delsanti et al. (2006), where $J-H_{solar}=0.23$, $H-K_{solar}=0.06$, and $J-K_{solar}=0.29$. The Trojan asteroid measurements follow the same formulation used in this work (Emery et al. 2011), so no solar corrections were necessary. The published data report $V-J$ color indices rather than $r'-J$ values, however, the variation in flux between the V ($\lambda_{center} \sim 0.55 \mu\text{m}$) and r' bands ($\lambda_{center} \sim 0.62 \mu\text{m}$) in our data are within observed uncertainties.

4.4 Results

NIR photometry is ideally suited for small asteroids when NIR spectroscopy is not viable due to their faintness. Our data show that although broadband photometry does not allow accurate identification of specific minerals, visible/NIR spectrophotometry is a powerful tool to study the general compositional differences between the Themis and Beagle asteroid families.

4.4.1 Spectral Features

Figures 4.1 and 4.2 show the normalized 4-color spectra for all of our observed targets, and the Themis and Beagle asteroids show a strikingly similar set of spectral features. All of the 4-color spectra show evidence of absorption features, with both families appearing to have 4 general shapes. The most common feature is a broad absorption that occurs between the r' and K bands, with a minima between the J and H bands (e.g. asteroid 23758; Fig. 4.1). For later reference, this feature is termed ‘ConcaveJH’ shaped. The second absorption feature is also concave but has a minimum in the J band (e.g. asteroid 30562; Fig. 4.1),

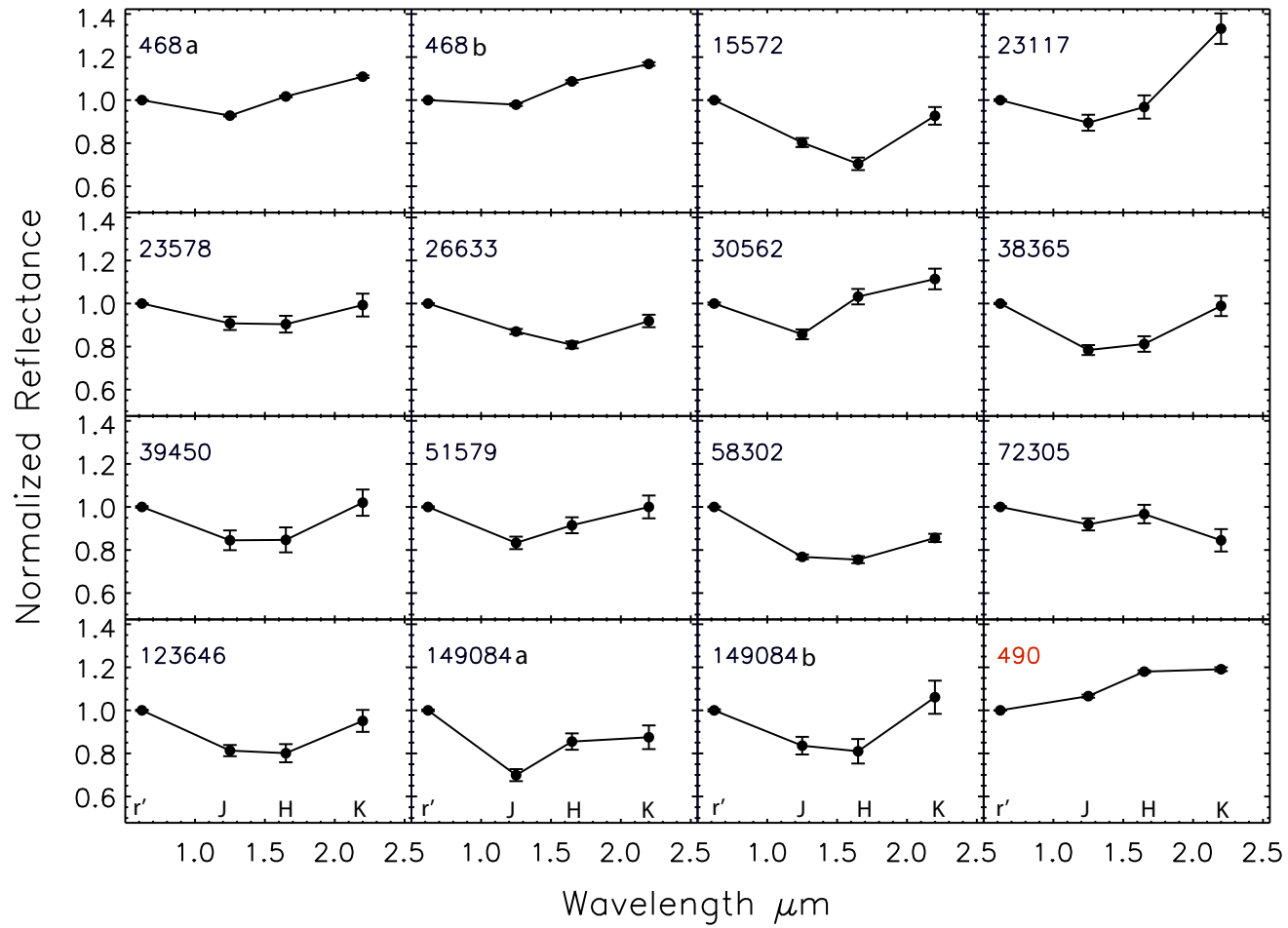


Figure 4.1 Four-color spectra of Themis asteroids (black labels) normalized to the r' -band. Asteroids with multiple observations are differentiated with 'a' and 'b' suffixes. For comparison a 4-color spectrum of the asteroid 490 Veritas is also shown (red label).

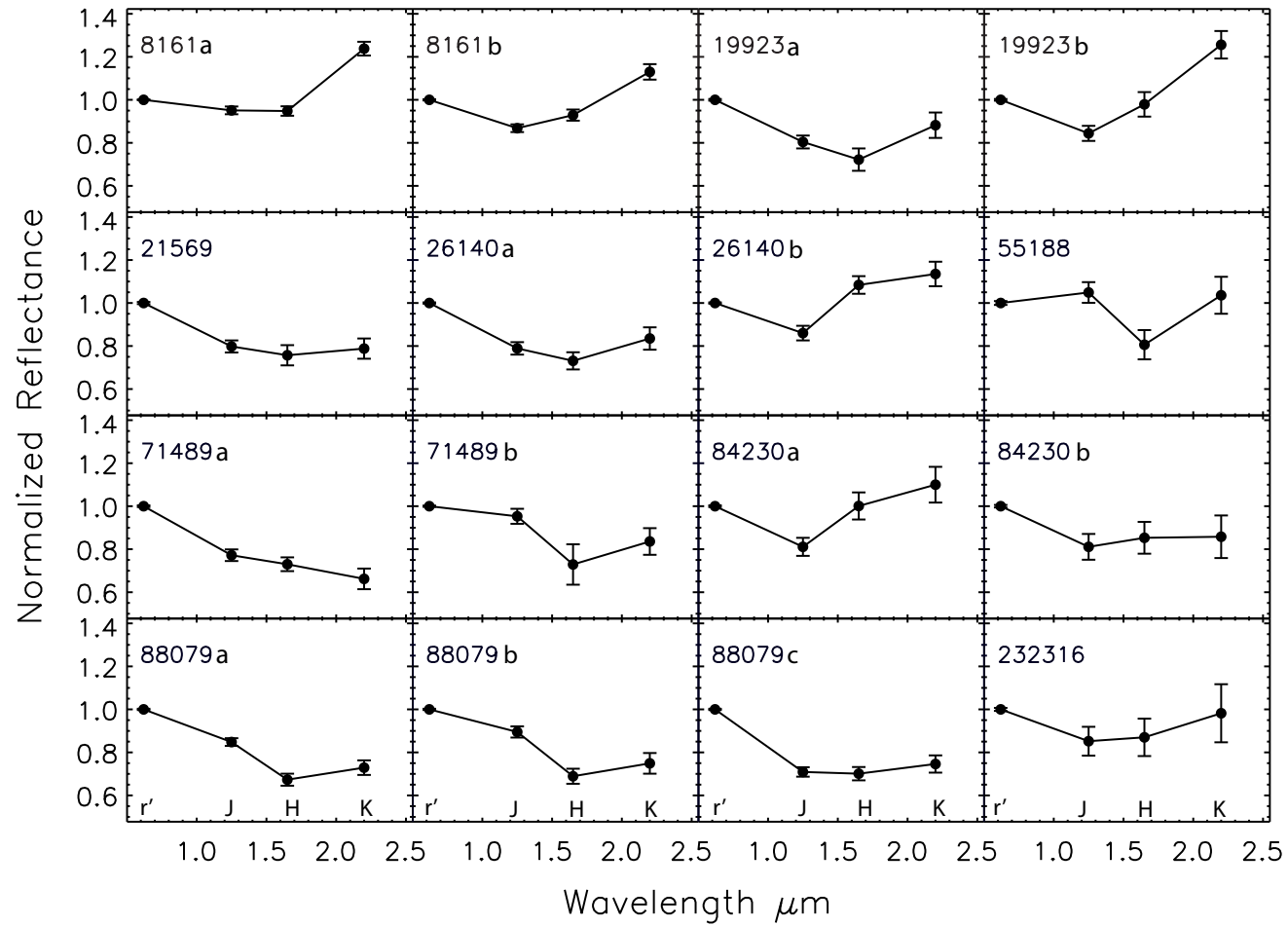


Figure 4.2 Four-color spectra of Beagle asteroids normalized to the r' -band. Asteroids with multiple observations are differentiated with 'a', 'b' and 'c' suffixes.

thus we term it ‘ConcaveJ’. The third feature corresponds to concave shapes with a minimum in H (e.g. asteroid 15572; Fig. 4.1), and is referred to as ‘ConcaveH’. The fourth feature is termed ‘Negative1’ because the reflectance continues to drop at longer wavelengths (e.g. asteroid 21569; Fig. 4.2). A fifth feature is also seen, termed ‘Negative2’, is only found among 4 members of the Beagle asteroids. This feature has an absorption minimum in the H-band and appears to lay between a negatively sloped r and K continuum (e.g. asteroid 71489; Fig. 4.2). To check the authenticity of these features, we re-examined images for nearby stars or other objects that may result in photometric errors, however, these measurements appear to be sound. Furthermore, these features are seen in multiple objects, and for objects such as 88079, the feature is seen on multiple occasions, implying that the absorption features are authentic. Tables 4.2 and 4.3 lists the feature shape for each asteroid.

As seen in Figures 4.1 and 4.2, asteroids 149084, 8161, 19923, 26140, 71489, and 84230 show variation in their spectral features. These features could be interpreted as photometric errors, however, the features all appear in several objects. Although follow-up observations are needed to confirm the change in spectral features with rotation, our data suggest there may be compositional variation across the surfaces of these asteroids Rivkin et al. (2002); Binzel et al. (2015).

In addition to the small Themis and Beagle asteroids, we observed a large diameter Themis asteroid (468; diameter~65 km Masiero et al. 2011) and Veritas asteroid (490; diameter~115 km Masiero et al. 2011) for comparison with the small diameter objects (Fig. 4.1). Comparison of the band depths between the small (<15 km) and the larger asteroids presented here and in Chapman et al. (2009) indicate the absorption bands for the large asteroids have depths up to ~10%, whereas they are as large as ~20% in the smaller objects. A follow-up study is necessary to confirm whether there is indeed a trend of increasing band depth with decreasing diameter. Although there are clear absorption features in our data, computing band depths and other spectral features such as slope, proved to be difficult due

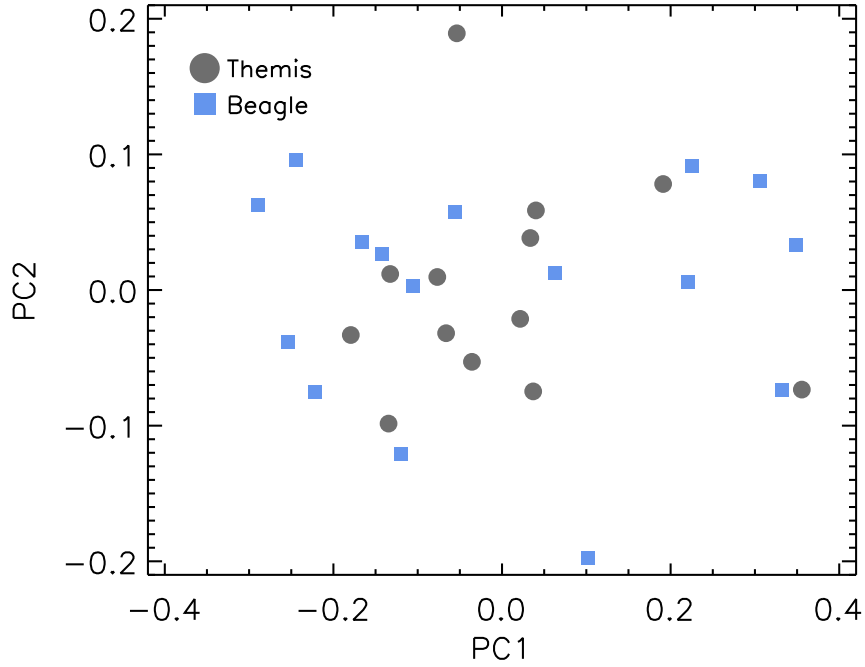


Figure 4.3 Principal component analyses for the Themis and Beagle 4-color spectra. PC1 is associated with the linear component and PC2 the curvature of the 4-color spectra.

to the lack of clear continuum regions in the 4-color spectra. However, in § 4.5, we present further discussion on the interpretation of the spectral shapes seen in our data.

Due to the difficulty in measuring spectral features, we used multivariate analysis to parameterize the 4-color spectrophotometry data and assess if there were notable differences between the NIR features of the Themis and Beagle asteroids. In particular, we create an IDL code that utilizes principal component analyses (PCA) to perform a set of linear transformations and produce a set of orthogonal vectors (eigenvectors) that represent the variance in our data. We used the resulting eigenvectors to transform the reflectance data into principal component space, where the first component (PC1) represents the largest variance within our data. Each subsequent component represents the next largest variance in the the data that is not represented in the preceding component. PCA is well suited for enhancing subtle differences in multivariate data, and it has often been used to parameterize

asteroid photometry and distinguish between asteroids of different taxonomic types (e.g. Tholen 1984). Thus we used PCA to enhance the spectral differences in the Themis and Beagle asteroid data, however, Figure 4.3 shows that there is no clear distinction between the visible/NIR spectral characteristics of the Themis and Beagle asteroids in principal component space.

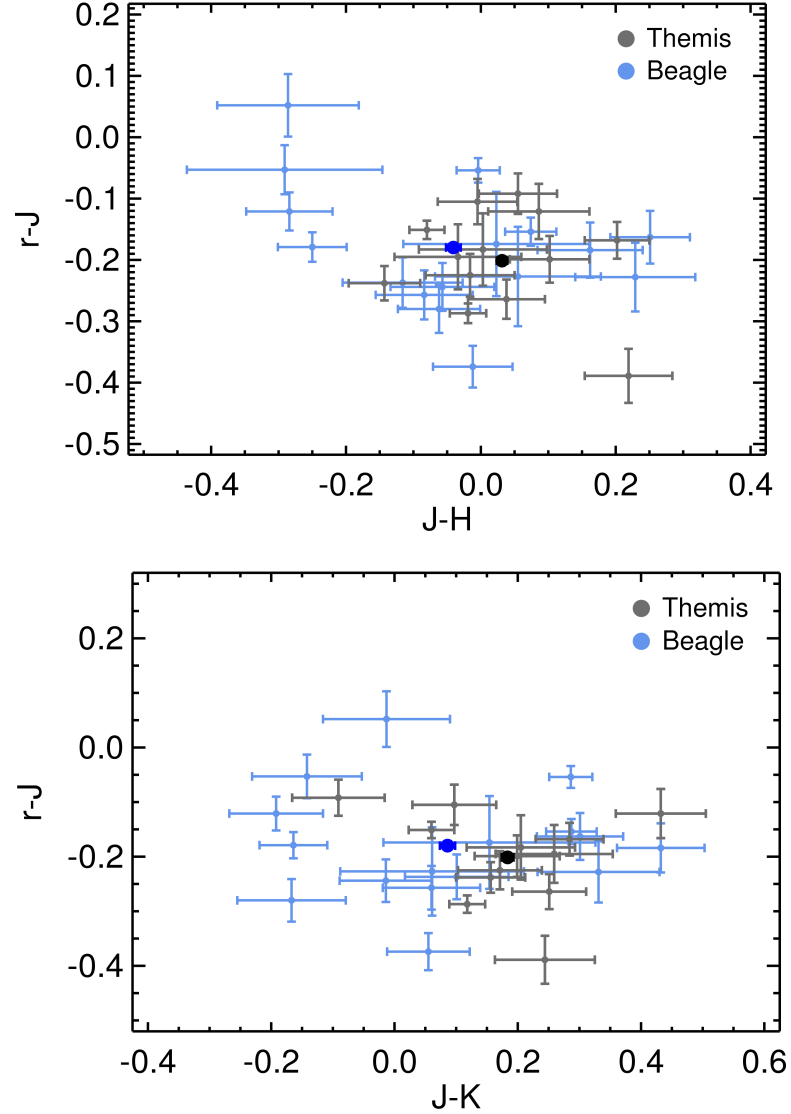


Figure 4.4 Color indices for the Themis and Beagle asteroids. The mean colors for Themis (black) and Beagle (blue) are also shown. The errors of the mean colors are approximately the same size as the symbols.

4.4.2 Color Trends

In addition to principal component analyses, we also used color indices to probe the broad spectral characteristics of Themis and Beagle asteroids. The mean color indices for the Themis and Beagle families were computed using only the objects with diameters <15 km and are reported in Tables 4.2 and 4.3. Although there appears to be a notable difference between the Themis and Beagle means, the statistical significance measured using the Kolmogorov-Smirnov (KS) test suggests the distributions are the same. It may be important to note that the J–K color indices had the smallest significance level and appears to be the most sensitive to any differences between the Themis and Beagle NIR colors.

Although the majority of the Themis and Beagle members have similar colors, there are several objects with notably different colors, as can be seen in Figure 4.4a. The four measurements with the lowest J–H values correspond to the three Beagle members (55188, 71489 - 2 observations, and 88079) which have the unique absorption feature not seen in the Themis members. The other data point that stands out is one of the observations of the Themis member 149084. This asteroid was observed twice, with the first observation that corresponds to the outlier point showing an absorption feature that we classify as ConcaveJ (i.e. minimum reflectance in the J band). Unlike the other asteroids that show this spectral shape (e.g. asteroids 30562, 26140), the r' band reflectance in 149084 is brighter than the H and K bands. The brighter reflectance in r' may simply be an observation uncertainty or may reflect a slope variation between 149084 and others with this spectral shape.

Figures 4.5 and 4.6 compare the color distributions of the Themis and Beagle asteroids with other solar system bodies. All but one of the Themis and Beagle asteroids have negative r' –J values, suggesting a B-type taxonomy. Within uncertainties the Themis and Beagle asteroids are not significantly distinct from other solar system bodies such as comets, Centaurs, and KBOs in NIR color space. However, aside from the C-complex asteroids, the Themis and Beagle asteroids are notably distinct from these solar system bodies in V–J space. Although the Trojan colors from Emery et al. (2011) report $0.85(\mu\text{m})$ –J rather than V–J, we plot the colors in Figure 4.5 for a rough comparison. If there is a difference

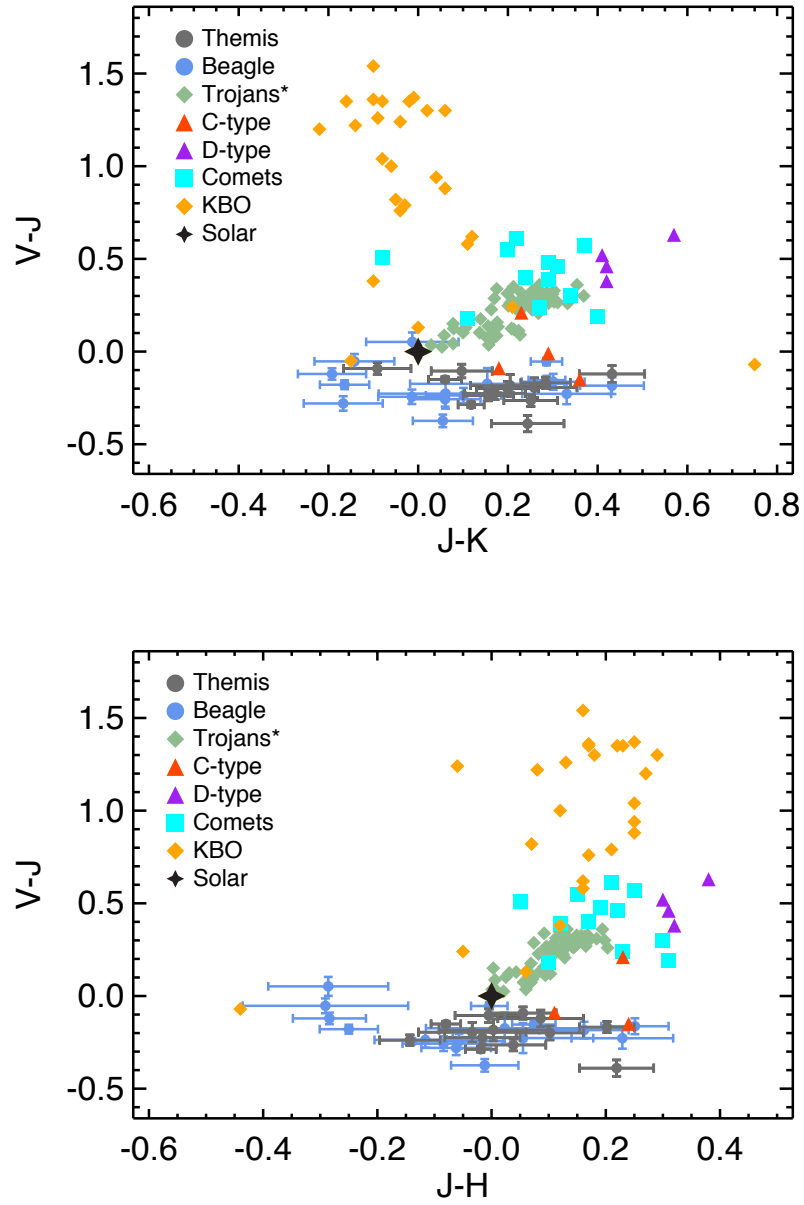


Figure 4.5 Color indices for the Themis and Beagle asteroids as compared to previously published color indices of other solar system bodies (Hartmann et al. 1982; Delsanti et al. 2006; Emery et al. 2011). *Note: Trojan asteroids are simply shown for general reference as the $V-J$ colors actually represent $0.85-J$ values and are therefore an underestimate of the $V-J$ colors (Emery et al. 2011).

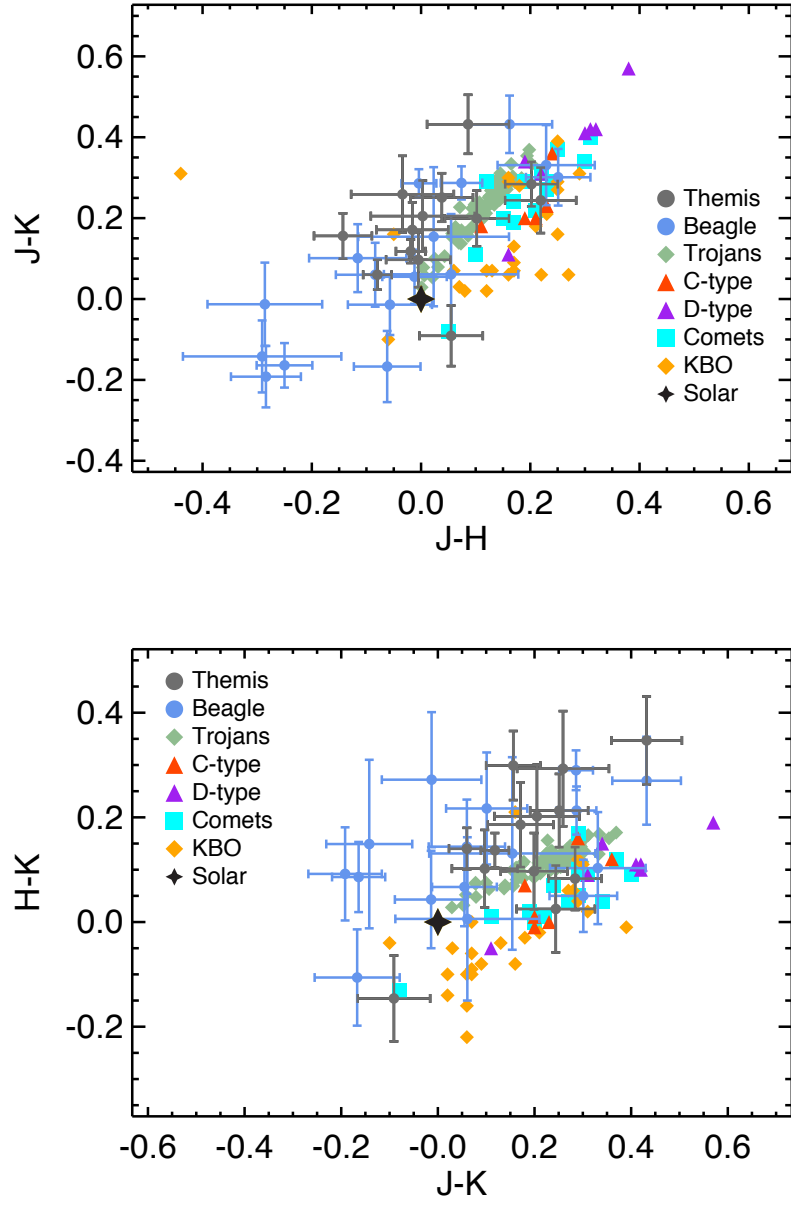


Figure 4.6 Color indices for the Themis and Beagle asteroids as compared to previously published color indices of other solar system bodies (Hartmann et al. 1982; Delsanti et al. 2006; Emery et al. 2011).

between the actual $V-J$ and $0.85(\mu\text{m})-J$ Trojan colors, it will likely be larger due to the relatively steep slopes seen in these objects Emery et al. (2011).

Although the Themis and Beagle asteroids show a large dispersion in NIR color space, they most closely resemble the Trojans (Fig. 4.6). However, the spectra from which the Trojan colors were derived (Emery et al. 2011) show no evidence of the absorption features seen in our data. Thus the similarity in trends likely reflects the similarity in the steep slopes of Trojans in the NIR and the reflectance differences resulting from absorption band centers and continuum shoulders. These data suggest NIR spectrophotometry without visible data is not an effective tool to differentiate between absorption bands and steeply sloped spectra.

4.5 Discussion

In Chapter 3, we find that at visible wavelengths, only a small fraction ($\sim 10\%$) of the Themis and Beagle asteroids show absorption features attributed to hydrated minerals. In addition, these features appear to be affected by both space weathering processes and regolith properties. Thus, visible wavelength absorption features do not appear to be a robust tool to characterize the mineralogy of C-complex asteroids. However, the data presented in this chapter suggest that NIR absorption features do not differ significantly between the two families and thus appear to provide a better way to assess the mineralogy of these C-complex asteroids.

4.5.1 NIR Space Weathering Trends of B-type Asteroids

The unique relationship between the Themis and Beagle families (Nesvorný et al. 2008) provide a critical tool to assess space weathering trends among C-complex asteroids with similar compositions. Several works presented contrasting space weathering trends in the visible wavelengths, where Nesvorný et al. (2005); Lantz et al. (2013) find slopes become bluer with age and Lazzarin et al. (2006) find they become redder. In Chapter 3, we find the Themis asteroid spectra appear redder than the Beagle asteroids and confirm the trends seen in Lazzarin et al. (2006).

Chapman et al. (2009) and Ziffer et al. (2008) use the Themis and Veritas asteroid families to look at space weathering trends in the NIR wavelengths. Ziffer et al. (2008) find that the NIR spectra of Themis asteroids have redder slopes than Veritas asteroids, and Chapman et al. (2009) find that the two families show different spectral shapes. However, our PCA analyses show no distinction between the Themis and Beagle asteroid visible/NIR 4-color spectra. Furthermore, the lack of NIR color differences between these two families that originated from the same parent body suggest space weathering is not effective at NIR wavelengths for C-complex asteroids. As shown in Chapter 3, although the Beagle and Veritas families are both C-complex families with similar dynamical ages, the Veritas family appears to have a different composition than the Beagle family. Therefore our NIR wavelength data re-emphasize the importance of accounting for mineralogy when studying space weathering trends among the broad C-complex class.

4.5.2 Spectral Features of B-type Asteroids

The taxonomic types B and F refer to those objects that have negative slopes as determined from visible/NIR data, however, (Tholen 1984; Bus & Binzel 2002b,a; DeMeo et al. 2009) find these asteroids are relatively rare ($\sim 5\%$) in the main asteroid belt population. In Chapter 3, we found $\sim 60\%$ (13 of 22) of Themis asteroids with diameters < 15 km and $\sim 80\%$ (20 of 23) of Beagle asteroids have B-type spectra. Almost all of the asteroids presented in this paper have negative $r'-J$ color indices reinforcing the conclusion that the Themis and Beagle families have a large fraction of B-type asteroids. The negative $r'-J$ color indices originate from the various absorption features that are seen in all of the 4-color spectra. Although the low resolution of our spectrophotometry prevent accurate feature fitting and the identification of what causes the features, we compare our spectral shapes to the spectra of B-type asteroids presented in Yang & Jewitt (2010); Clark et al. (2010).

Clark et al. (2010) obtained visible/NIR spectra of 22 B-type asteroids and divide the various spectral shapes into 3 broad groups; Pallas, Themis, and other. Two of the three groups are shown in Figure 4.7. The Pallas group contains asteroids with spectra that

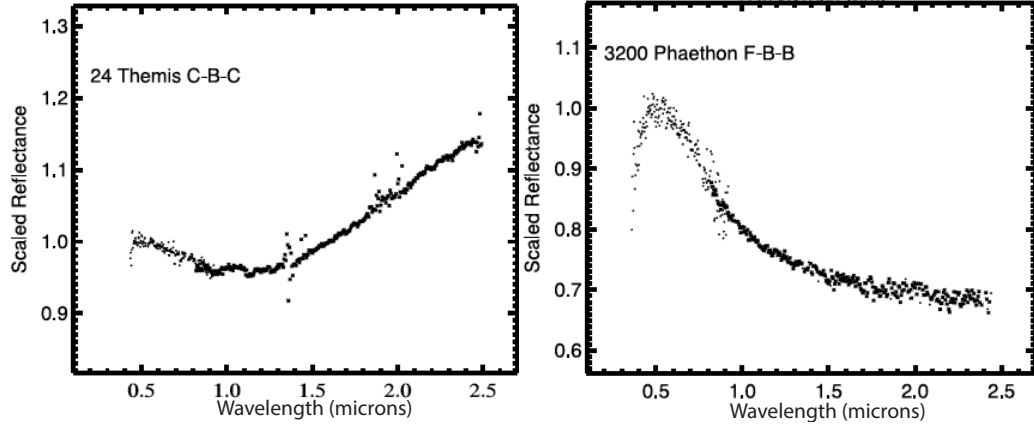


Figure 4.7 Visible and NIR spectra of B-type asteroids from Clark et al. (2010). *Left:* A spectrum of the asteroid 24/Themis, which represents a Themis group spectrum as defined by Clark et al. (2010). *Right:* A spectrum of the 3200/Phaethon, which represents a Pallas group spectrum as defined by Clark et al. (2010).

are negatively sloped out to $2.5\mu\text{m}$. The Negative1 and Negative2 shapes identified in our 4-color spectra are very similar to the spectral shapes found in Clark’s Pallas group. The Negative1 shapes most closely resemble the spectra of 2 Pallas and 3200 Phaethon, whereas the uniquely Negative2 shape seen in the Beagle asteroids resemble the spectrum of asteroid 426 Hippo. Our spectra with ‘Concave’ shapes are generally consistent with the spectra of objects in Clark’s Themis group where absorption bands vary between 1.1 and $1.5\mu\text{m}$.

Clark et al. (2010) used data from the RELAB spectral library (Pieters 1983) to identify which meteorites and mineral spectra were consistent with their spectra of B-type asteroids. Similar to the spectral matches for 3200 Phaethon from Licandro et al. (2007), Clark et al. (2010) find a mixture of chlorite and carbon best fit the spectral features of the Pallas group. Chlorite is a phyllosilicate found to varying degrees in most carbonaceous chondrite (CC) meteorites and is formed through the process of aqueous alteration (e.g. Rubin (1997); Howard et al. (2011); Cloutis et al. (2011, 2012)). Given the detection of phyllosilicate features on the Themis and Beagle asteroids (Florczak et al. 1999; Kaluna et al. 2015), chlorite appears to be a viable cause for the ‘Negative’ shapes in our data. Clark et al. (2010) suggest the Themis group spectra are best fit to CM, CI and thermally metamorphosed

CM/CI meteorite spectra, which is consistent with the compositions suggested by Gaffey & McCord (1978); Vilas (1994); Hiroi et al. (1996); Yang & Jewitt (2010).

Yang & Jewitt (2010) find that the broad absorption features of B-type asteroids is well fit over a wide wavelength range to a mixture of magnetite and neutral material. Magnetite is also found in CCs and is another indicator of aqueous alteration (Kerridge et al. 1979). However, the magnetite feature is centered at $\sim 1 \mu\text{m}$, which is most consistent with our ConcaveJ shapes, but not the others. The ConcaveJH and ConcaveH features appear to be more consistent with Themis group spectra that have band centers near ~ 1.3 to $1.5 \mu\text{m}$ (Clark et al. 2010).

Future work involving the conversion of RELAB spectra to visible/NIR colors will be necessary to constrain the composition of these small Themis and Beagle asteroids for which NIR spectroscopy is not viable. However, despite the lack of constrained composition, both the NIR data and visible data show the Themis and Beagle asteroids have B-type taxonomies, which are associated with significant aqueous alteration histories.

4.5.3 Aqueous Alteration in the Beagle Parent Body

The large fraction of B-type taxonomies and the association of this taxonomic type with phyllosilicates and other aqueously altered minerals (Clark et al. 2010; Yang & Jewitt 2010) suggest the Themis and Beagle parent body experienced extensive aqueous alteration. However, several MBCs are dynamically associated with both families (Hsieh 2009; Novaković et al. 2012), so although our data suggest aqueous alteration was extensive, there must have been at least a small fraction of ice preserved during the thermal evolution of the Themis/Beagle parent body.

Assuming aqueous alteration depletes all of the ice within the region where the alteration occurs, then the high fraction of B-type members (as shown in Chapter 3) and hydrated asteroids in the Themis and Beagle families imply that only a small fraction of the Themis/Beagle parent body was able to preserve ice. Castillo-Rogez & Schmidt (2010) use geophysical evolution models to gain insight into the thermal evolution of the Themis

family parent body. Two of the models begin with a homogeneous mixture of ice and rock, and only differ in the Themis parent body formation time after CAIs. A formation time of 5 Myr after CAIs results in partial (40%) differentiation of the ice and rock, and only a small degree of aqueous alteration. However, if the formation time of the model is reduced to 3 Myr after CAIs, the Themis parent body undergoes significant geophysical evolution. In the latter model, the Themis parent body evolves to have a large silicate-core dominated by hydrated silicates and a water ice rich shell. The apparently high fraction of Themis and Beagle members with aqueously altered mineral features suggests the Themis and Beagle parent body is more likely to have formed around 3 Myr after CAIs. However, more observations and a proper analysis of the NIR absorption features is necessary to better characterize the extent of aqueous alteration in the Themis and Beagle parent body.

4.6 Summary

Our spectrophotometry of 13 Themis and 9 Beagle asteroids yield the following results:

1. There is no statistical difference between the Themis and Beagle in principal component or color space, implying space weathering does not significantly alter the spectral features of C-complex asteroids in NIR wavelengths.
2. An absorption feature centered near $1.0\ \mu\text{m}$ is seen in all but one of the Themis and Beagle asteroids. There are five apparent variations in the shape and band center of these absorption features, however they each appear consistent with aqueously altered mineralogy.
3. The Themis and Beagle parent body appears to have experienced an extensive degree of aqueous alteration, which has important implications on the formation time of the Themis parent body.

Table 4.1. IRTF Observations

Asteroid ID	Hmag	Diam (km)	Obs Run	Vmag	Solar Analog	a (AU)	e	i ($^{\circ}$)	r (AU)	α ($^{\circ}$)
Themis										
468	9.8	64.59	2	15.5	SA 102-1081	3.132	0.198	0.437	3.732	7.10
468	9.8	64.59	4	15.4	SA 102-1081	3.132	0.198	0.437	3.732	6.58
15572	13.4	8.12	8	18.2	SA 115-271	3.209	0.168	2.109	2.938	12.38
23117	13.8	7.93	8	18.5	SA 110-361	3.102	0.142	0.551	2.988	11.45
23578	13.7	9.69	8	18.9	SA 110-361	3.112	0.150	1.773	3.319	10.50
26633	14.1	8.06	6	18.0	SA 115-271	3.220	0.176	2.544	2.667	11.75
30562	13.9	7.49	9	18.7	SA 93-101	3.221	0.156	0.410	2.771	18.31
38365	14.1	7.79	3	18.8	SA 102-1081	3.198	0.194	2.558	3.242	2.23
39450	14.8	5.67	5	19.2	SA 102-1081	3.197	0.174	2.193	2.715	14.79
51579	14.2	6.01	7	18.3	SA110-361	3.166	0.196	2.688	2.567	13.92
58302	14.2	6.91	4	17.9	SA 102-1081	3.097	0.156	1.607	2.695	4.04
72305	14.2	7.48	1	19.1	SA 102-1081	3.203	0.150	0.215	2.742	19.73
123646	14.6	5.80	3	19.0	SA 102-1081	3.225	0.110	2.432	2.893	6.13
149084	15.0	4.78	1	19.2	SA 102-1081	3.182	0.162	2.604	2.670	6.49
	15.0	4.78	4	19.3	SA 102-1081	3.182	0.162	2.604	2.670	2.78
Beagle										
8161	13.3	10.51	8	18.2	SA115-271	3.167	0.168	2.544	2.712	19.83
	13.3	10.51	10	17.6	SA 98-978	3.167	0.168	2.544	2.741	13.39
19923	13.8	8.08	3	19.0	SA 102-1081	3.161	0.111	1.698	3.091	14.03
	13.8	8.08	5	19.1	SA 102-1081	3.161	0.111	1.698	3.088	14.72
21569	13.9	13.65	1	19.4	SA 102-1081	3.164	0.116	0.676	2.834	20.07
26140	14.1	7.83	6	19.2	SA 93-101	3.152	0.137	2.545	3.357	10.13
	14.1	7.83	7	19.1	SA 115-271	3.152	0.137	2.545	3.358	9.85
55188	13.6	8.69	9	19.1	SA 98-978	3.160	0.183	2.453	2.748	20.51
71489	13.8	8.13	6	18.6	SA 93-101	3.150	0.130	0.781	3.362	1.67
	13.8	8.13	7	18.6	SA 113-276	3.150	0.130	0.781	3.363	2.00

Table 4.1—Continued

Asteroid ID	Hmag	Diam (km)	Obs Run	Vmag	Solar Analog	a (AU)	e	i ($^{\circ}$)	r (AU)	α ($^{\circ}$)
84230	15.1	5.49	8	19.5	SA 113-276	3.157	0.167	0.925	3.006	5.09
	15.1	5.49	10	19.5	SA 113- 276	3.157	0.167	0.925	2.962	5.44
88079	14.9	5.49	1	18.8	SA 102-1081	3.151	0.139	0.112	2.754	3.16
	14.9	5.49	2	18.8	SA 102-1081	3.151	0.139	0.112	2.755	3.60
	14.9	5.49	3	18.8	SA 102-1081	3.151	0.139	0.112	2.755	4.03
232316	16.3	2.65	8	20.0	SA 113-276	3.166	0.171	0.097	2.775	1.64
Veritas										
490	8.32	115.55	2	14.1	SA 102-1081	3.172	0.095	9.280	3.469	13.58

Note. — Observing runs 1-10 correspond Feb. 10, 11, 12, 13, 15, Aug. 29, 30, 31 and Sep. 20 and 27, 2013 respectively. [†] Diameters were computed using visible albedos either from WISE or using the mean albedo for each family when WISE albedos were not available.

Table 4.2. IRTF Themis Asteroid Colors

Asteroid	D (km) [†]	Obs Run	r-J	J-H	J-K	H-K	Feature [‡] Type
468	64.59	2	-0.081 ± 0.005	0.099 ± 0.007	0.193 ± 0.008	0.094 ± 0.008	ConcaveJ
468	64.59	4	-0.023 ± 0.006	0.113 ± 0.009	0.192 ± 0.010	0.078 ± 0.010	ConcaveJ
15572	8.12	8	-0.238 ± 0.028	-0.143 ± 0.053	0.156 ± 0.056	0.299 ± 0.066	ConcaveH
23117	7.93	8	-0.121 ± 0.045	0.086 ± 0.075	0.432 ± 0.073	0.347 ± 0.084	ConcaveJH
23578	9.69	8	-0.105 ± 0.037	-0.005 ± 0.059	0.097 ± 0.068	0.102 ± 0.074	ConcaveJH
26633	8.06	6	-0.151 ± 0.015	-0.080 ± 0.026	0.060 ± 0.037	0.140 ± 0.040	ConcaveH
30562	7.49	9	-0.168 ± 0.030	0.202 ± 0.048	0.284 ± 0.055	0.083 ± 0.060	ConcaveJ
38365	7.79	3	-0.264 ± 0.032	0.038 ± 0.057	0.251 ± 0.060	0.213 ± 0.070	ConcaveJH
39450	5.67	5	-0.183 ± 0.059	0.003 ± 0.095	0.205 ± 0.088	0.202 ± 0.099	ConcaveJH
51579	6.01	7	-0.199 ± 0.038	0.102 ± 0.059	0.199 ± 0.069	0.097 ± 0.073	ConcaveJ
58302	6.91	4	-0.287 ± 0.016	-0.019 ± 0.027	0.118 ± 0.029	0.137 ± 0.033	Negative1
72305	7.48	1	-0.092 ± 0.033	0.055 ± 0.058	-0.091 ± 0.075	-0.146 ± 0.082	Negative1
123646	5.80	3	-0.225 ± 0.035	-0.016 ± 0.066	0.171 ± 0.068	0.186 ± 0.081	ConcaveJH
149084	4.78	1	-0.389 ± 0.044	0.219 ± 0.065	0.244 ± 0.081	0.025 ± 0.083	ConcaveJ
	4.78	4	-0.195 ± 0.053	-0.034 ± 0.094	0.259 ± 0.095	0.293 ± 0.110	ConcaveJH
Mean			-0.201 ± 0.006	0.031 ± 0.008	0.183 ± 0.010	0.152 ± 0.010	

Note. — Observing runs 1-10 correspond Feb. 10, 11, 12, 13, 15, Aug. 29, 30, 31 and Sep. 20 and 27, 2013 respectively. [†] Diameters were computed using visible albedos either from WISE or using the mean albedo for each family when WISE albedos were not available. [‡] See text for description of feature shapes.

Table 4.3. IRTF Beagle Asteroid Colors

Asteroid	D (km) [†]	Obs Run	r-J	J-H	J-K	H-K	Feature [‡] Type
8161	10.51	8	-0.054 ± 0.020	-0.004 ± 0.032	0.286 ± 0.035	0.290 ± 0.038	ConcaveJH
	10.51	10	-0.154 ± 0.023	0.074 ± 0.038	0.287 ± 0.041	0.213 ± 0.046	ConcaveJH
19923	8.08	3	-0.237 ± 0.041	-0.116 ± 0.089	0.101 ± 0.084	0.217 ± 0.107	ConcaveH
	8.08	5	-0.184 ± 0.045	0.162 ± 0.078	0.432 ± 0.071	0.270 ± 0.084	ConcaveJ
21569	13.65	1	-0.244 ± 0.039	-0.057 ± 0.077	-0.014 ± 0.075	0.043 ± 0.093	Negative1
26140	7.83	6	-0.257 ± 0.040	-0.084 ± 0.072	0.060 ± 0.079	0.144 ± 0.090	Negative1
	7.83	7	-0.163 ± 0.043	0.251 ± 0.059	0.301 ± 0.070	0.050 ± 0.069	ConcaveJ
55188	8.69	9	0.052 ± 0.051	-0.286 ± 0.105	-0.013 ± 0.103	0.272 ± 0.129	Negative2
71489	8.13	6	-0.280 ± 0.039	-0.062 ± 0.061	-0.167 ± 0.088	-0.106 ± 0.092	Negative1
	8.13	7	-0.053 ± 0.040	-0.291 ± 0.145	-0.142 ± 0.089	0.149 ± 0.161	Negative2
84230	5.49	8	-0.228 ± 0.056	0.229 ± 0.089	0.331 ± 0.099	0.103 ± 0.107	ConcaveJ
	5.49	10	-0.227 ± 0.081	0.055 ± 0.123	0.061 ± 0.149	0.006 ± 0.156	Negative1
88079	5.49	1	-0.179 ± 0.024	-0.250 ± 0.051	-0.164 ± 0.055	0.086 ± 0.067	Negative2
	5.49	2	-0.121 ± 0.031	-0.284 ± 0.064	-0.192 ± 0.076	0.092 ± 0.089	Negative2
	5.49	3	-0.374 ± 0.034	-0.012 ± 0.059	0.055 ± 0.067	0.067 ± 0.075	Negative1
232316	2.65	8	-0.174 ± 0.085	0.023 ± 0.138	0.154 ± 0.172	0.131 ± 0.184	ConcaveJH
Mean			-0.180 ± 0.006	-0.041 ± 0.011	0.086 ± 0.012	0.127 ± 0.007	

Note. — Observing runs 1-10 correspond Feb. 10, 11, 12, 13, 15, Aug. 29, 30, 31 and Sep. 20 and 27, 2013 respectively. [†] Diameters were computed using visible albedos either from WISE or using the mean albedo for each family when WISE albedos were not available. [‡] See text for description of feature shapes.

References

- Binzel, R. P., DeMeo, F. E., Burt, B. J., Cloutis, E. A., Rozitis, B., Burbine, T. H., Campins, H., Clark, B. E., Emery, J. P., Hergenrother, C. W., Howell, E. S., Lauretta, D. S., Nolan, M. C., Mansfield, M., Pietrasz, V., Polishook, D., & Scheeres, D. J. 2015, *Icarus*, 256, 22
- Bus, S. J. & Binzel, R. P. 2002a, *Icarus*, 158, 146
- Bus, S. J. & Binzel, R. P. 2002b, *Icarus*, 158, 106
- Castillo-Rogez, J. C. & Schmidt, B. E. 2010, *Geophys. Res. Lett.*, 37, L10202
- Chapman, C. R. 2004, *Annual Review of Earth and Planetary Sciences*, 32, 539
- Chapman, C. R., Enke, B., Merline, W. J., Nesvorný, D., Tamblyn, P., & Young, E. F. 2009, in *Lunar and Planetary Science Conference*, Vol. 40, *Lunar and Planetary Science Conference*, 2258
- Clark, B. E., Ziffer, J., Nesvorny, D., Campins, H., Rivkin, A. S., Hiroi, T., Barucci, M. A., Fulchignoni, M., Binzel, R. P., Fornasier, S., DeMeo, F., Ockert-Bell, M. E., Licandro, J., & Mothé-Diniz, T. 2010, *Journal of Geophysical Research (Planets)*, 115, 6005
- Cloutis, E. A., Hiroi, T., Gaffey, M. J., Alexander, C. M. O. ., & Mann, P. 2011, *Icarus*, 212, 180
- Cloutis, E. A., Hudon, P., Hiroi, T., Gaffey, M. J., Mann, P., & Bell, J. F. 2012, *Icarus*, 221, 328

- Delsanti, A., Peixinho, N., Boehnhardt, H., Barucci, A., Merlin, F., Doressoundiram, A., & Davies, J. K. 2006, *AJ*, 131, 1851
- DeMeo, F. E., Binzel, R. P., Slivan, S. M., & Bus, S. J. 2009, *Icarus*, 202, 160
- Emery, J. P., Burr, D. M., & Cruikshank, D. P. 2011, *AJ*, 141, 25
- Florczak, M., Lazzaro, D., Mothé-Diniz, T., Angeli, C. A., & Betzler, A. S. 1999, *A&AS*, 134, 463
- Fornasier, S., Lantz, C., Barucci, M. A., & Lazzarin, M. 2014, *Icarus*, 233, 163
- Gaffey, M. J. & McCord, T. B. 1978, *Space Sci. Rev.*, 21, 555
- Gulbis, A. A. S., Bus, S. J., Elliot, J. L., Rayner, J. T., Stahlberger, W. E., Rojas, F. E., Adams, E. R., Person, M. J., Chung, R., Tokunaga, A. T., & Zuluaga, C. A. 2011, *PASP*, 123, 461
- Hartmann, W. K., Cruikshank, D. P., & Degewij, J. 1982, *Icarus*, 52, 377
- Hiroi, T., Zolensky, M. E., Pieters, C. M., & Lipschutz, M. E. 1996, *Meteoritics and Planetary Science*, 31, 321
- Howard, K. T., Benedix, G. K., Bland, P. A., & Cressey, G. 2011, *Geochimica et Cosmochimica Acta*, 75, 2735
- Hsieh, H. H. 2009, *A&A*, 505, 1297
- Jedicke, R., Nesvorný, D., Whiteley, R., Ivezić, Ž., & Jurić, M. 2004, *Nature*, 429, 275
- Jørgensen, I. 2009, *Publications of the Astronomical Society of Australia*, 26, 17
- Kaluna, H. M., Masiero, J. R., & Meech, K. J. 2015, *Icarus*
- Kerridge, J. F., Mackay, A. L., & Boynton, W. V. 1979, *Science*, 205, 395
- Lantz, C., Clark, B. E., Barucci, M. A., & Lauretta, D. S. 2013, *A&A*, 554, A138

- Lazzarin, M., Marchi, S., Moroz, L. V., Brunetto, R., Magrin, S., Paolicchi, P., & Strazzulla, G. 2006, *ApJ*, 647, L179
- Licandro, J., Pinilla-Alonso, N., de León, J., Campins, H., Boehnhardt, H., Tozzi, G., Hainaut, O., & Mothé-Diniz, T. 2007, in *Bulletin of the American Astronomical Society*, Vol. 38, AAS/Division for Planetary Sciences Meeting Abstracts #39, 470–+
- Marzari, F., Davis, D., & Vanzani, V. 1995, *Icarus*, 113, 168
- Masiero, J. R., Mainzer, A. K., Grav, T., Bauer, J. M., Cutri, R. M., Dailey, J., Eisenhardt, P. R. M., McMillan, R. S., Spahr, T. B., Skrutskie, M. F., Tholen, D., Walker, R. G., Wright, E. L., DeBaun, E., Elsbury, D., Gautier, IV, T., Gomillion, S., & Wilkins, A. 2011, *ApJ*, 741, 68
- Nesvorný, D. 2012, *NASA Planetary Data System*, 189
- Nesvorný, D., Bottke, W. F., Levison, H. F., & Dones, L. 2003, *ApJ*, 591, 486
- Nesvorný, D., Bottke, W. F., Vokrouhlický, D., Sykes, M., Lien, D. J., & Stansberry, J. 2008, *ApJ*, 679, L143
- Nesvorný, D., Jedicke, R., Whiteley, R. J., & Ivezić, Ž. 2005, *Icarus*, 173, 132
- Novaković, B., Hsieh, H. H., & Cellino, A. 2012, *MNRAS*, 424, 1432
- Pieters, C. M. 1983, *J. Geophys. Res.*, 88, 9534
- Rayner, J. T., Onaka, P. M., Cushing, M. C., & Vacca, W. D. 2004, in *Society of Photo-Optical Instrumentation Engineers (SPIE) Conference Series*, Vol. 5492, *Ground-based Instrumentation for Astronomy*, ed. A. F. M. Moorwood & M. Iye, 1498–1509
- Rivkin, A. S., Howell, E. S., Vilas, F., & Lebofsky, L. A. 2002, *Asteroids III*, 235
- Rubin, A. E. 1997, *Meteoritics and Planetary Science*, 32, 231
- Tholen, D. J. 1984, PhD thesis, University of Arizona, Tucson

Tokunaga, A. T., Simons, D. A., & Vacca, W. D. 2002, PASP, 114, 180

Vilas, F. 1994, Icarus, 111, 456

Yang, B. & Jewitt, D. 2010, AJ, 140, 692

Ziffer, J., Campins, H., Howell, E. S., Licandro, J., Walker, M., Deshpande, R., & Hargrove, K. 2008, in Bulletin of the American Astronomical Society, Vol. 40, AAS/Division for Planetary Sciences Meeting Abstracts #40, 509

Chapter 5

The Spin Pole Orientation of the Main Belt Comet 133P/Elst-Pizarro

5.1 Introduction

The term ‘active asteroids’ is used to describe asteroids which experience mass loss in the form of a comet-like dust tail or coma (Jewitt 2012). A suite of physical mechanisms ranging from impact ejection to rotational instability and electrostatic levitation could result in the comet-like activity on active asteroids. However, the objects that appear to be active as a result of ice sublimation are termed ‘main belt comets’ (MBCs) (Hsieh et al. 2006). Although no direct evidence of gas has been observed on MBCs, 133P/Elst-Pizarro, 238P/Read and 313P/Gibbs have shown recurrent activity near perihelion (Hsieh et al. 2004, 2010; Jewitt et al. 2014; Hsieh et al. 2011, 2015), indicating mass loss due to the sublimation of ice.

133P/Elst-Pizarro, 176P/Linear and P/2006VW₁₃₉ are three active asteroids associated with the Themis and Beagle asteroid families (Hsieh 2009; Nesvorný et al. 2008; Novaković et al. 2012). In Chapters 3 and 4, we show that the Themis and Beagle asteroids exhibit spectral features associated with aqueously altered minerals. These minerals result from low temperature reactions between liquid water and anhydrous minerals in asteroid parent bodies ~ 15 Myr after nebular collapse (Krot et al. 2006). Although aqueously altered mineral features indicate the Themis and Beagle families formed as a mixture of water ice

and rock, only after the discovery of 133P/Elst-Pizarro (Boehnhardt et al. 1996) was it found that water ice was still preserved within the asteroid belt. Thermal evolution models conducted by Prialnik & Rosenberg (2009) and Schorghofer (2008) suggest that ice can be preserved for billions of years in the subsurfaces of small asteroids if they maintain an insulating regolith layer and/or low obliquities.

In this chapter, we investigate the rotational spin axis orientation of 133P/Elst-Pizarro to test and constrain models of ice longevity in asteroids. We use data obtained over a ten-year observing campaign and employ light curve inversion to determine the pole orientation and constrain the obliquity of 133P/Elst-Pizarro.

5.2 Observations and Reductions

We observed 133P/Elst-Pizarro from 2002 through 2011 using the University of Hawai'i (UH) 2.2 m telescope on Mauna Kea and the New Technology Telescope (NTT), operated by the European Southern Observatory (ESO) at La Silla. A log of observations and observing geometry is shown in Table 5.1. The UH 2.2 m observations were made using the Kron-Cousins VRI broadband filters and an image scale $0.219'' \text{ pixel}^{-1}$. Observations at the NTT were made using the ESO Multi-Mode Instrument (EMMI), which utilizes two adjacent MIT/LL CCDs, both having 2048×4096 pixels and pixel scales of $0.166'' \text{ pixel}^{-1}$. Image exposure times ranged from 300 to 600 seconds while tracking at non-sidereal rates appropriate for the target.

We performed bias subtraction and flat field reductions on each nights data. Flat fields were obtained using 10-15 dithered images taken each night during twilight, which were median combined to produce master flats for each evening. Photometry was obtained by measuring the total flux within a circular aperture ranging in radius from $1''$ to $5''$ due to fluctuations in nightly seeing. Apertures sizes were chosen to measure $\sim 99\%$ of the flux within each objects radial profile. Absolute flux calibration was achieved by taking images

Table 5.1. 133P/Elst-Pizarro Observations and Geometry

UT Date	Telescope	r^a (AU)	Δ^b (AU)	α^c ($^\circ$)	L^d ($^\circ$)	B^e ($^\circ$)	ν^f ($^\circ$)	Nobs g	δt^h (hrs)
08/19/2002	UH 2.2m	2.858	2.046	14.35	356.4	-0.39	63.246	6	3.1
09/07/2002	UH 2.2m	2.886	1.935	8.10	0.4	-0.48	67.228	24	2.0
09/08/2002	UH 2.2m	2.887	1.932	7.74	0.6	-0.48	67.427	6	3.8
09/09/2002	UH 2.2m	2.889	1.928	7.36	0.8	-0.49	67.626	8	6.0
11/05/2002	UH 2.2m	2.977	2.181	13.33	12.2	-0.73	79.069	6	3.8
11/06/2002	UH 2.2m	2.979	2.193	13.57	12.4	-0.74	79.256	5	3.1
11/07/2002	UH 2.2m	2.980	2.204	13.80	12.6	-0.74	79.443	4	1.2
12/27/2002	UH 2.2m	3.061	2.933	18.73	22.1	-0.92	88.941	14	2.4
12/28/2002	UH 2.2m	3.062	2.948	18.71	22.2	-0.93	89.118	8	1.7
07/17/2007	NTT 3.58m	2.643	1.628	1.65	296.7	0.95	4.449	19	2.1
07/20/2007	NTT 3.58m	2.643	1.627	0.62	297.5	0.94	5.191	16	1.6
10/26/2008	UH 2.2m	3.198	2.206	1.40	37.6	-1.66	103.734	13	3.9
10/27/2008	UH 2.2m	3.200	2.207	1.06	37.4	-1.67	103.903	34	6.3
11/25/2008	UH 2.2m	3.244	2.359	9.08	32.2	-1.67	108.721	4	0.4
11/26/2008	UH 2.2m	3.245	2.369	9.39	32.0	-1.66	108.885	16	1.9
11/28/2008	UH 2.2m	3.248	2.616	9.95	31.8	-1.66	109.212	17	4.3
02/12/2010	UH 2.2m	3.665	2.970	12.17	103.9	-1.15	171.4	17	3.1
02/13/2010	UH 2.2m	3.665	2.982	12.37	104.0	-1.15	171.5	13	1.9
02/14/2011	UH 2.2m	3.516	2.538	2.65	152.1	-0.19	219.6	52	8.5

Note. — a -Heliocentric range, b -Observer range, c -Phase angle, d -Heliocentric ecliptic longitude, e -Heliocentric ecliptic latitude, f -True anomaly, g -Number of images, h -Length of observations.

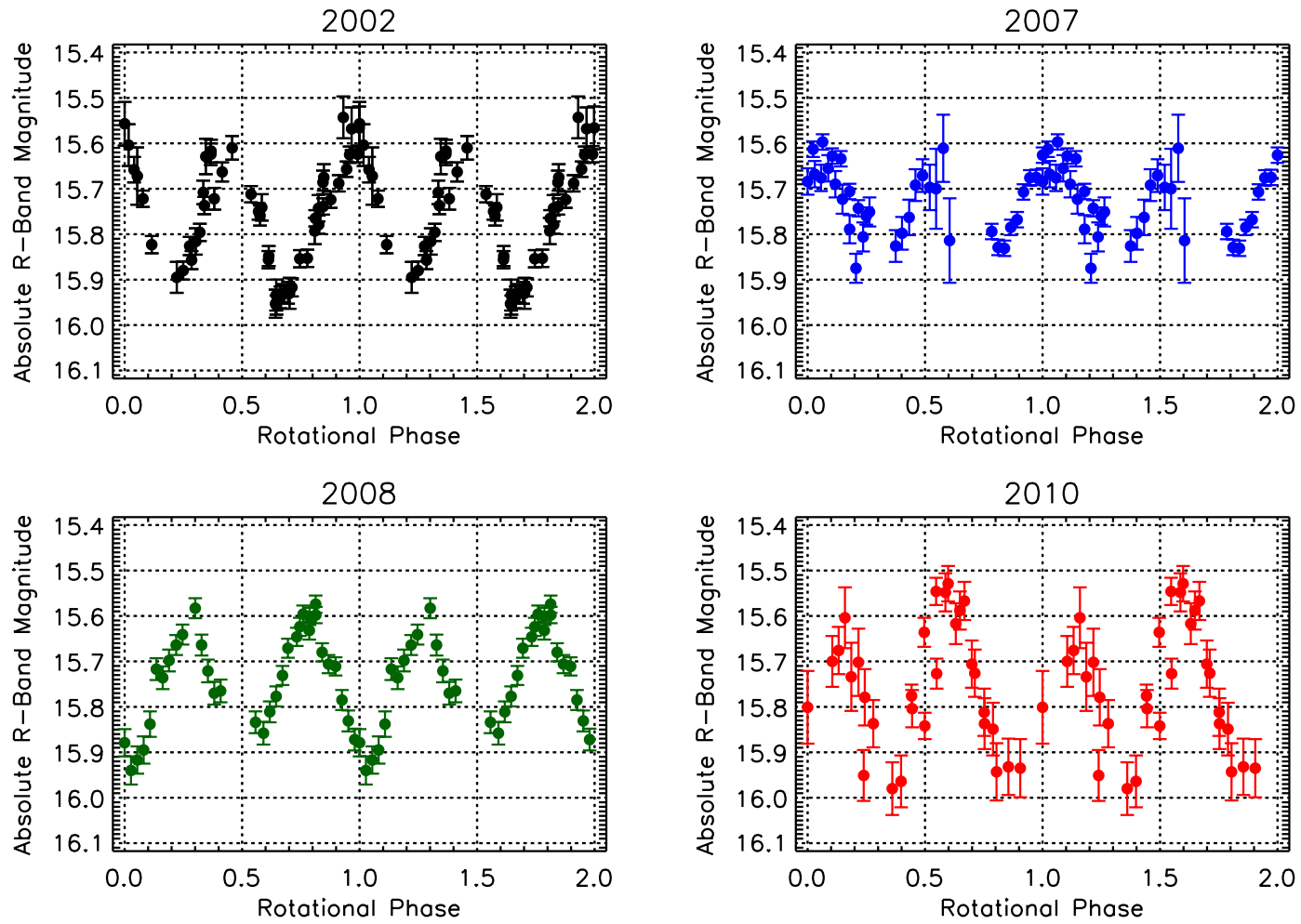


Figure 5.1 133P/Elst-Pizarro phased lightcurves

of Landolt standard stars and measuring the instrumental color terms, zero points and extinction coefficients for each night’s data. For non-photometric nights, 133P/Elst-Pizarro fields were re-imaged later when conditions were photometric. To further increase the accuracy of our data, photometry was also obtained for as many field stars (7-30) in each of the images, with each star’s flux averaged and used to measure deviations from image to image. These deviations were then applied to our measurements of 133P/Elst-Pizarro, improving our lightcurves by several percent.

5.3 Analysis and Results

5.3.1 Lightcurve Inversion

We used the lightcurve inversion software, `convexinv`, available from the Database of Asteroid Models from Inversion Techniques (DAMIT; Durech et al. 2010), to solve for the rotation period of 133P/Elst-Pizarro. This software utilizes a fast ray-tracing algorithm to simultaneously solve for the shape, spin and scattering model of an asteroid. The inversion process generates a convex asteroid shape model and optimizes it so that modeled light curves fit the input observed light curves, $L^{(i)}$ and $L_{obs}^{(i)}$ respectively. The relative chi-square is defined in Eq. 5.1.

$$\chi_{rel}^2 = \sum_i \left| \frac{L_{obs}^{(i)}}{\bar{L}_{obs}^{(i)}} - \frac{L^{(i)}}{\bar{L}^{(i)}} \right|^2, \quad (5.1)$$

where $\bar{L}^{(i)}$ and $\bar{L}_{obs}^{(i)}$ are the average modeled and observed brightness. The program’s input consists of one-way light travel time corrected lightcurves and observed fluxes, which have been converted from reduced magnitudes, as well as the ecliptic cartesian coordinates of the Sun and Earth with respect to the asteroid. Also required is an input file that holds the initial parameters, listed in Table 5.2, and are described in more detail in Kaasalainen & Torppa (2001) and Kaasalainen et al. (2001). Also included in the input parameters is a value for the rotation period (see § 5.3.1)

Table 5.2. Convexinv Input Parameters

Parameters	Values Used	Fixed/Free (0/1)
period_scan specific parameters		
Initial P[hr], final P[hr] and period step [hr]	3.4705, 3.4715, 10^{-5}	n/a
convexinv specific parameters		
Initial λ_{ecl}^*	0° to 350°	1
Initial β_{ecl}^*	-90° to $+90^\circ$	1
Initial P[hr]	3.47101 ± 0.00033	0
Initial epoch [†]	0	0
Initial rotation angle [†]	0	0
period_scan and convexinv common parameters:		
Convexity regularization [†]	0.1	0
Laplace series l and m [†]	6 and 6	0
Resolution [†]	8	0
Amplitude a^\ddagger	0	1
Width d^\ddagger	0.1	1
Slope k^\ddagger	0	1
Lambert coeff c	0.1	0
Iteration stop condition	Varied	n/a

Note. — * Ecliptic longitude (λ_{ecl}) and latitude (β_{ecl}) of rotation spin pole. [†]Parameters held fixed by the program, [‡]Phase function parameters from Eq. 5.2.

The model utilizes light scattering parameters such as a phase function parameterization, Eq. 5.2, where α is the phase angle, k is the slope of the linear part of the phase function, and a and d are the amplitude and width of the opposition surge.

$$f(\alpha) = a \exp\left(-\frac{\alpha}{d}\right) + k\alpha + 1 \quad (5.2)$$

A simple empirical scattering law is also adopted, shown in Eq. (5.3). The law is a combination of the Lommel-Seeliger, Eq. (5.4), single scattering and the Lambert, Eq. (5.5), multiple scattering laws (Kaasalainen et al. 2001). The terms μ and μ_0 are the cosines of the angles of incidence and reflection.

$$S(\mu, \mu_0, \alpha) = f(\alpha)[S_{LS}(\mu, \mu_0) + cS_L(\mu, \mu_0)] \quad (5.3)$$

The Lommel-Seeliger single scattering law, S_{LS} , is given by:

$$S_{LS} = \frac{S_L}{(\mu + \mu_0)}, \quad (5.4)$$

and the Lambert multiple scattering law, S_L , is given by:

$$S_L = \mu\mu_0. \quad (5.5)$$

5.3.2 Rotation Period

Hsieh et al. (2004) derived a rotation period of 3.471 ± 0.001 h for 133P/Elst-Pizarro using data collected in 2002. Delahodde et al. (2004) combined their 2002 data set with that of Hsieh et al. (2004) and derived a rotation period of 3.47113 ± 0.00001 h. Determining a rotation period with high precision typically involves using densely sampled data that span a short time interval. The strength of light curve inversion is that it simultaneously determines the period, pole and shape of an asteroid using both sparsely and densely sampled data

Table 5.3. Physical Characteristics as a Function of Observing Epochs

Epoch	β	Δm_r	Axis ratio
2002	0.044 ± 0.007	0.40 ± 0.05	1.45 ± 0.07
2007	0.049 ± 0.004	0.28 ± 0.04	1.29 ± 0.04
2008	0.039 ± 0.009	0.37 ± 0.04	1.41 ± 0.04
2010	0.052 ± 0.007	0.44 ± 0.07	1.50 ± 0.07
2011 [†]	—	0.48 ± 0.06	1.56 ± 0.06

Note. — β : linear phase function, Δm_r : Lightcurve range, axis ratio: derived from Δm_r . [†]2011 data were taken on a single night, so no β derived for this epoch.

Table 5.4. 133P/Elst-Pizarro Rotation Periods from Period Scan

Epoch	Period (hrs)	Period Scan RMS (hrs)
2002	3.47092	0.03986
2002-2007	3.47101	0.03948
2002-2008	3.47088	0.04198
2002-2010	3.47113	0.04534
2002-2011	3.47112	0.04816
Standard Deviation [†]	0.00011	—

Note. — The best fit rotation periods from **Period Scan** as subsequent data are added. [†]The standard deviation was derived from the set of rotation periods.

across a large time span (Durech et al. 2009). We used light curve inversion on the full data set from 2002 through 2011 to test the rotation period found by Delahodde et al. (2004).

We phased each night's data set for those epochs that had sufficient data, and refined light curves by removing anomalously bright or faint data points. 133P/Elst-Pizarro was observed active during the 2002 and 2007 epochs, so prior to phasing the data, we corrected for coma contamination by using the absolute magnitude and phase function parameters derived from data were 133P/Elst-Pizarro. Discrepancies between the observed and expected brightness allowed us to estimate the scattering surface area of the dust and correct for coma contamination. A more detailed description of this correction is presented in Hsieh et al. (2010). Data were phased by first converting apparent magnitudes $m_r(r, \Delta, \alpha)$ to reduced magnitudes at unit distances, $m_r(1, 1, \alpha)$, using Equation 5.6:

$$m_r(1, 1, \alpha) = m_r(r, \Delta, \alpha) - 5 \log r \Delta, \quad (5.6)$$

where r is heliocentric distance; Δ is geocentric distance and α is phase angle. The reduced magnitudes were then averaged as a function of phase angle and fit using a linear regression. The slope of the fit, β , was used to convert the reduced magnitudes to absolute magnitudes through Equation 5.7:

$$m_r(1, 1, 0) = m_r(1, 1, \alpha) - \beta \alpha. \quad (5.7)$$

The values of β were computed for epochs where the data spanned more than several nights. In addition, for each epoch the ratio of 133P/Elst-Pizarro's projected axes were determined using the lightcurve ranges as shown in Eq. 5.8

$$a/b = 10^{0.4 \Delta m_R}. \quad (5.8)$$

Both the β and axis ratios are shown in Table 5.3. The refined phased light curves are shown in Figure 5.1.

Rotation period estimates were computed using the `period_scan` program (Durech et al. 2010), which utilizes the inversion process as described above, but only optimizes the shape and spin parameters of the model. By first determining the period solution using only the 2002 data, and monitoring the solutions as data from subsequent epochs, we found the rotation period varied as more data was used. The set of solutions as each epochs data were added are shown in Table 5.4. We use the variation in period solutions to measure the `period_scan` rotation period uncertainty. Using the full data set, the best fit rotation period is found to be 3.47112 ± 0.00011 h, consistent with the rotation period derived by Delahodde et al. (2004).

5.3.3 Pole Orientation

We used our light curves as input to the `convexinv` program to measure the pole orientation, shape and spin parameters of 133P/Elst-Pizarro. To ensure the robustness of the model, we varied the initial input pole values by 30° for ecliptic longitude (λ_{ecl}) and 15° for ecliptic latitude (β_{ecl}), creating a 13x12 grid of 156 input pole values. `Convexinv` allows the user to determine which parameters to fit or hold fixed. Thus, we ran the `convexinv` software for a range of periods (~ 3.4707 - 3.4714 , varied at increments of ~ 0.00001) while holding the period parameter fixed to measure the variation in the `convexinv` solutions. We found the pole orientation solutions varied quite largely as the input period was varied. In addition, there were several pole solutions that shared the lowest χ_{rel}^2 value and neither corresponded to the best fit period from `period_scan`.

Due to the sensitivity of the `convexinv` model to the input period values, we do not use the spin pole solutions corresponding to the minimum χ_{rel}^2 value. Instead, we estimate the pole orientation solutions from the mean of pole solutions that had χ_{rel}^2 values within 2-sigma of the minimum χ_{rel}^2 value. The pole solutions have a degeneracy of 180° , which is a product of the inability of light curve inversion to differentiate between poles oriented in opposite ecliptic longitude directions. Accounting for the degeneracy in ecliptic longitude, we find the pole orientation of 133P/Elst-Pizarro $\lambda_{ecl,1} = 103^\circ \pm 31^\circ$, $\beta_{ecl,1} = 12^\circ \pm 28^\circ$ and

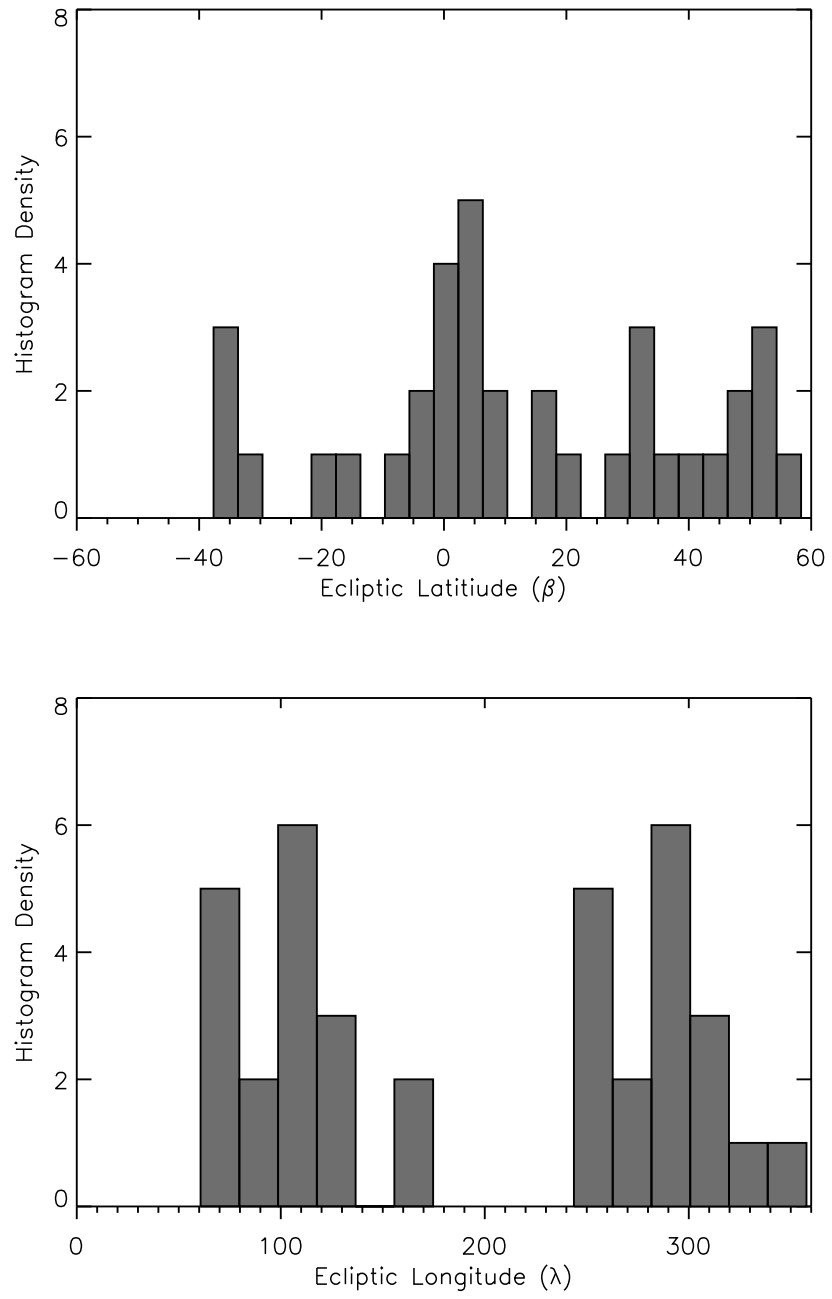


Figure 5.2 Histograms representing the distribution of 133P/Elst-Pizarro spin pole solutions in ecliptic longitude (λ_{ecl}) and ecliptic latitude β_{ecl} .

$\lambda_{ecl,2} = 284^\circ \pm 30^\circ$, $\beta_{ecl,2} = 14^\circ \pm 28^\circ$. The uncertainties represent the standard deviation of the λ_{ecl} and β_{ecl} values from the pole solutions that were used to derive the mean. The distribution of λ_{ecl} and β_{ecl} are shown in Figure 5.2. Obliquity is the angle between an objects rotation spin axis and the orbital plane. 133P/Elst-Pizarro has a small orbital inclination of $i=1.4^\circ$, thus we neglect the orbital inclination and find the obliquity using $\varepsilon = 90^\circ - \beta_{ecl}$. Although the uncertainties are large for β_{ecl} , our data suggest the spin axis of 133P/Elst-Pizarro is highly inclined, having an obliquity as large as 75° .

As described in §5.3.1, `convexinv` simultaneously solves for the shape, spin and scattering model of an asteroid. However, we derive the pole orientation for 133P/Elst-Pizarro using a set of `convexinv` pole solutions for a range of periods. To address this issue, we run `convexinv` while holding the initial input pole values constant for a rotation period of 3.47112 hours. The resulting shape model for an spin pole orientation of $\lambda_{ecl,1} = 103^\circ \pm 31^\circ$, $\beta_{ecl,1} = 12^\circ \pm 28^\circ$ is shown in Figure 5.3. It is important to note that changing the input period results in a largely different shape model, and more work will need to be done to assess the uncertainty of the shape model. Therefore the model we show here is for visualization purposes only and should not be interpreted as the proper shape model for 133P/Elst-Pizarro.

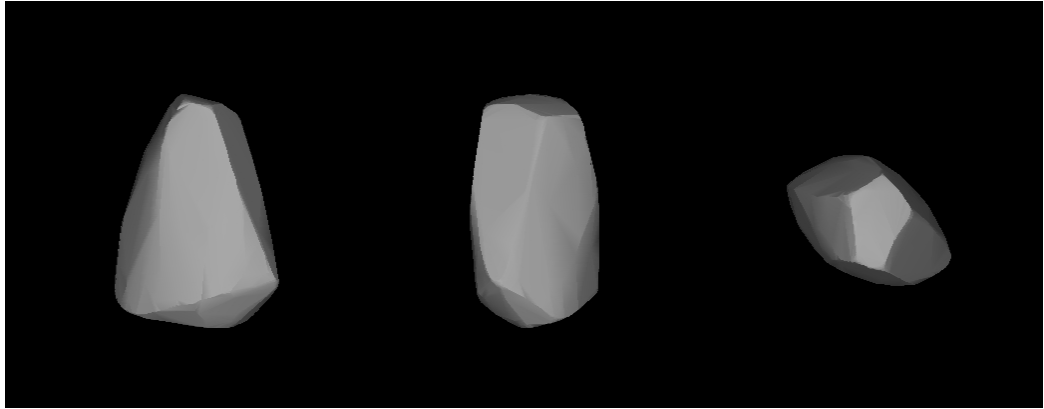


Figure 5.3 A shape model generated from `convexinv`. This model corresponds to the rotational spin pole solution of $\lambda_{ecl,1} = 103^\circ \pm 31^\circ$, $\beta_{ecl,1} = 12^\circ \pm 28^\circ$

5.3.4 Model calculations of ice loss

We use the many observational constraints available for 133P/Elst-Pizarro, such as obliquity (75°), rotation period (3.47112 hr), albedo (0.05), and its likely age (10 Myr), to study of the ice retreat in this MBC. Fanale & Salvail (1984) have pointed out that on extinct comets, ice may be accessible within 10 m of the surface. Schorghofer (2008) found that ice can be even nearer the surface, if the surface mantle consists of dust. Prialnik & Rosenberg (2009) found that after 4.6 Gyr ice can be expected at depths ranging from ~ 50 to 150 m. Here, we carry out model calculations for ice depth, using time steps that are small enough to resolve day-night temperature variations and long integration periods that correspond to the age of the body.

Thermal and vapor diffusion model

The model consists of two components, a thermal model that calculates surface and subsurface temperatures and an ice evolution model that follows the retreat of ice over time. These two models are coupled asynchronously, i.e., they use different time steps. The thermal model needs to resolve day-night cycles; we use 100 time steps for every solar day, i.e. the time step is about 2 minutes. The time steps for the ice evolution model are much larger and increase progressively with time. The thermal model is evolved for 5 orbits (period=5.6 years) to equilibrate and the time averages from the last orbit serve as input to the ice evolution model. The asynchronous coupling allows us to effectively integrate for up to 2 Gyr with time steps of 2 minutes.

The surface energy balance consists of direct incoming sunlight (insolation), blackbody emission (scaling as T^4 , where T is temperature in K), and heat conduction into the subsurface. Subsurface heat conduction is described by the one-dimensional heat equation. The heat equation is solved numerically with a Cranck-Nicholson scheme using geometrically spaced depths and at least six grid points within the rotational thermal skin depth. The heat flux from the interior is assumed to be zero and lateral heat transport is neglected in the model.

Table 5.5. Thermal and Vapor Model Parameters

Grain Size (mm)	D (140 K) (m ² /s)	A (W/mK)	B (W/mK ⁴)	Γ (140 K) (tiu)	δ (diurnal) (mm)	δ (seasonal) (m)
0.1	0.003	0.001	3.0×10^{-11}	23	3	0.36
1.0	0.029	0.003	1.5×10^{-10}	40	5	0.64
10.0	0.286	0.010	2.0×10^{-9}	85	12	1.40

Note. — Parametrization of vapor diffusivity D and thermal conductivity coefficients A and B in Eq. (5.10) for several grain diameters. The thermal inertia Γ and the thermal skin depth δ are nominal values for the dry material at a constant temperature of 140 K.

Water is lost to space after it diffuses through the already desiccated surface mantle. The model assumes that the regolith matrix stays in-place after the ice retreats. If instead, the ice/dust ratio is so high that the dry matrix collapses after the ice has retreated, the burial depths would be smaller than calculated here.

The equations for the vapor transport are based on Evans et al. (1961); Mason & Malinauskas (1983) and Mason et al. (1967). The diffusion coefficient is proportional to the mean thermal speed and to the mean free path of water molecules. The specific expressions for the vapor diffusivity D and the vapor flux \bar{J} are given in Schorghofer (2008), and they are nearly the same as in Fanale & Salvail (1984).

The equilibrium vapor pressure, p_s , of crystalline ice is well-known for temperatures above ~ 140 K, and at these temperatures any amorphous ice quickly transforms into crystalline ice (Jenniskens et al. 1998), so that all of the ice can be assumed to be crystalline.

The retreat rate of the ice is calculated by

$$\frac{dz}{dt} = -\frac{\bar{J}}{\Phi \rho_{\text{ice}}} = -\frac{D \bar{\rho}_s}{z \Phi \rho_{\text{ice}}} \quad (5.9)$$

where z is the depth of the ice table beneath the surface, t time (sec), Φ the porosity of the dry regolith matrix (assumed to be 0.5), $\rho_{\text{ice}} = 931 \text{ kg m}^{-3}$ is the density of ice at 140 K, and $\bar{\rho}_s$ is the time-averaged equilibrium vapor pressure of ice at the depth of the ice

table. For a detailed justification of the prefactor of $1/\Phi$ and the numerical treatment of the differential equation (5.9) see Schorghofer (2010).

Properties of the surface mantle

The physical properties of the surface layer are crucial for the modeling results, but unknown. Hence, we carry out calculations for a range of grain sizes. The grain diameter d (mm) is important for both the thermal conductivity and the vapor diffusivity of the mantle.

Thermal conductivity is modeled as a constant term that arises from the solid conduction and a temperature dependent term that represents radiative heat transfer,

$$k = A + BT^3 \quad (5.10)$$

(e.g., Cremers & Birkebak 1971; Schotte 1960). The parameters A and B are based on the laboratory measurements by Sakatani et al. (2012) and given in Table 5.5. These values are also consistent with measured values for fine lunar grain sizes (Cremers & Birkebak 1971). The coefficients A and B both increase with particle size. For 1 cm diameter grains, B is estimated as $4\sigma d$, where σ is the Stefan-Boltzmann constant. The conductivity values in Table 5.5 are significantly lower than what is listed for dust, sand, and gravel-sized particulate matter for terrestrial applications due to the significant role of interstitial air conductivity.

Extremely low thermal inertias have been suggested for asteroids ($15 \text{ J/m}^2/\text{K/s}^{0.5}$) by Spencer et al. (1989) and were measured on 9P/Tempel 1 ($<50 \text{ J/m}^2/\text{K/s}^{0.5}$) by Groussin et al. (2007), 21 Lutetia ($20\text{--}30 \text{ J/m}^2/\text{K/s}^{0.5}$) by Coradini et al. (2011) and on 67P/Churyumov-Gerasimenko ($\sim 10\text{--}50 \text{ J/m}^2/\text{K/s}^{0.5}$) by Gulkis et al. (2015). An IRAS (Infrared Astronomical Satellite) survey of main belt asteroids with diameters smaller than 100 km finds $15\text{--}400 \text{ J/m}^2/\text{K/s}^{0.5}$, where smaller bodies tend to have a larger thermal inertia (Delbo' & Tanga 2009). The thermal inertia of Elst-Pizarro is observationally

unconstrained, so we carry out model calculations for several grain sizes to derive estimates for 133P/Elst-Pizarro's thermal inertia.

Thermal inertia is defined by $\Gamma = \sqrt{k\rho c}$, where ρ is density and c heat capacity, and is reported in units of $\text{J/m}^2/\text{K/s}^{0.5}$. An expression for the temperature dependent heat capacity of silicates is provided by Winter & Saari (1969) (e.g. at 140 K, $c = 386 \text{ J/kgK}$). Thermal inertias for a temperature of 140 K are given in Table 5.5 for various grain sizes. The effective thermal inertia can be different because of its temperature dependence. We calculated time-averaged thermal inertias from the model calculations and found these to be nearly the same as those listed in Table 5.5. The density of the dry regolith is taken as $(1 - \Phi) \times 2400 \text{ kg m}^{-3}$. The thermal properties of the combined ice/soil matrix are determined by volumetric addition, using $k_{\text{ice}} = 4.6 \text{ Wm}^{-1}\text{K}^{-1}$ and $c_{\text{ice}} = 1145 \text{ J/kgK}$, as appropriate at 140 K (Lide 2003).

In addition to the thermal conductivity and inertia, we define the thermal skin depth as $\delta = \sqrt{kP/(\pi\rho c)}$, where P is the time period of temperature oscillations. The ice/regolith matrix is assumed to be completely filled with ice, i.e. it is assumed to have no void spaces. These assumptions simplify the model considerably, because no redistribution of ice takes place in the interior.

5.3.5 Ice Depth in 133P/Elst-Pizarro

The model scenario assumes that after breakup from the parent body, the ice in 133P/Elst-Pizarro initially extended all the way to the surface. The obliquity of the rotation axis and the eccentricity of the orbit are held constant while the angle between the perihelion and the body's equinox sweeps through the whole circle. Holding these parameters fixed leads to nearly symmetric burial depths on both hemispheres.

Figure 5.4 shows the ice depths after 10 Myr as a function of latitude, and as expected, the depth to the ice strongly depends on grain size. In addition, smaller pore spaces lead to lower vapor diffusivity (Table 5.5) and higher surface temperature amplitudes that cool the body due to T^4 -emission (Schorghofer 2008). Although there are differences in the depth

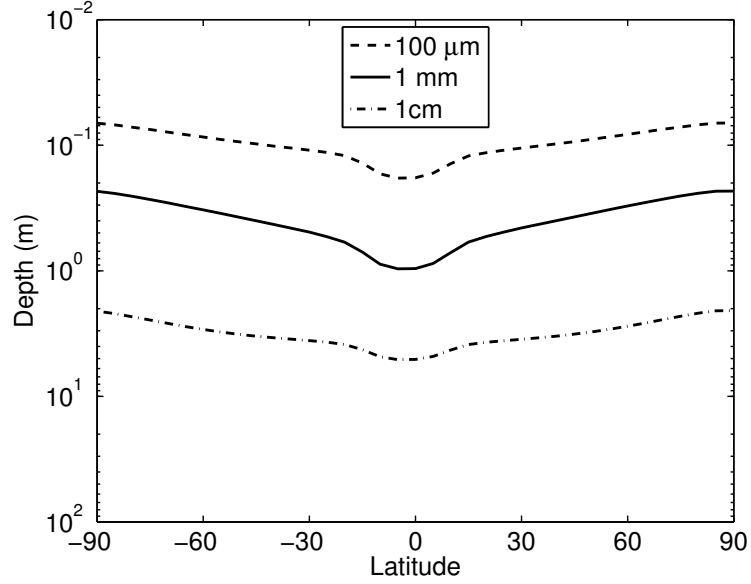


Figure 5.4 Depth to ice as a function of planetodetic latitude for 133P/Elst-Pizarro after 10 Myr, the estimated age of the Beagle family. The three lines represent different grain sizes for the surface mantle, which determine its thermal conductivity and vapor diffusivity.

between the equator and the poles, all depths are small compared to the radius of the body (~ 2 km). At $100 \mu\text{m}$ grain size, the depth to the ice is 0.07–0.18 m, whereas for 1 mm grains it is 0.23–0.97 m, and for 1 cm grains it is 2.1–5.1 m. The ice is the shallowest at the rotational poles, so even with a high obliquity, the mean temperatures at the poles are lower than in the equatorial regions.

For a prolate spheroid rotating around its major axis or an oblate spheroid rotating around its minor axis, the latitude is replaced by the planetodetic latitude. The planetodetic latitude of a point on the surface is the angle between the surface normal and the equatorial plane. Figure 5.5 shows mean, maximum, and minimum surface temperatures as a function of planetodetic latitude. The surface temperature amplitudes, which include the day-night as well as seasonal cycles, are large. Since 133P/Elst-Pizarro has a high obliquity, most latitudes experience polar winter and reach very low minimum surface temperatures. The mean surface temperature is highest at the equator, but significantly colder than the effective surface temperature of 155 K, because radiative cooling is proportional to T^4 .

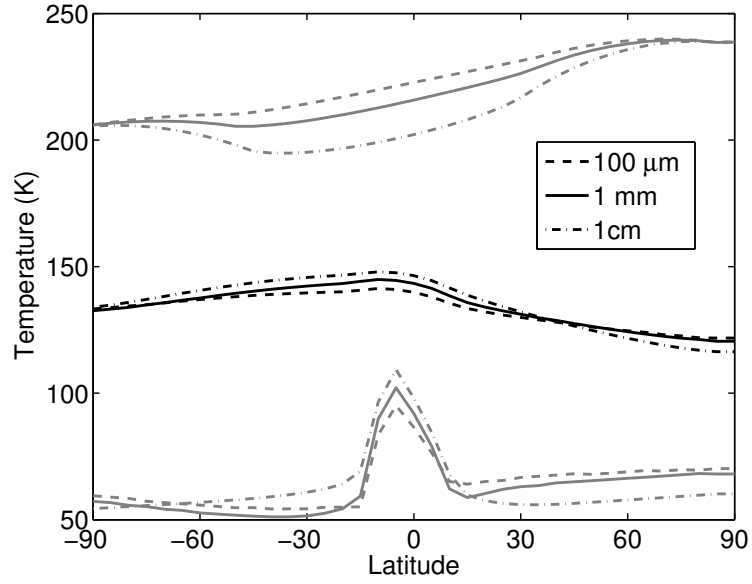


Figure 5.5 Maximum (top curves), mean (middle curves), and minimum (bottom curves) surface temperature as a function of planetodetic latitude for 133P/Elst-Pizarro.

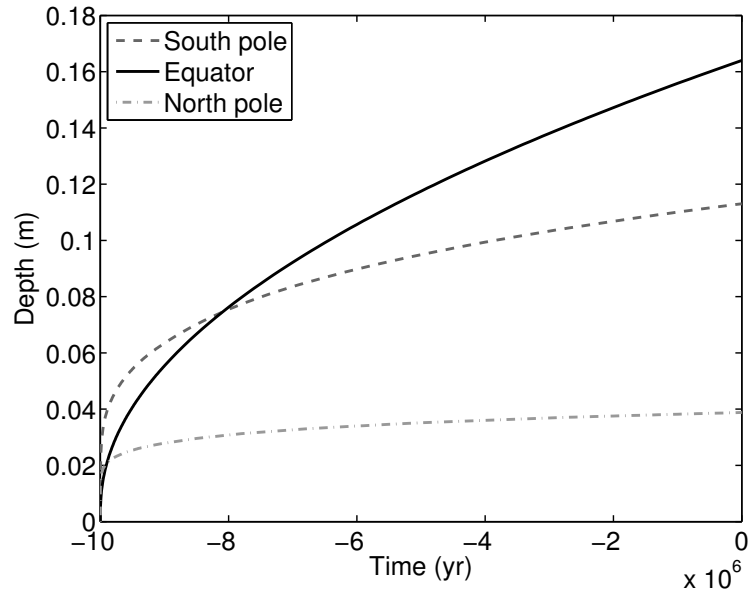


Figure 5.6 Burial depth of ice as a function of time for 133P/Elst-Pizarro at the equator and the two rotational poles. Assumed grain size is $100 \mu\text{m}$.

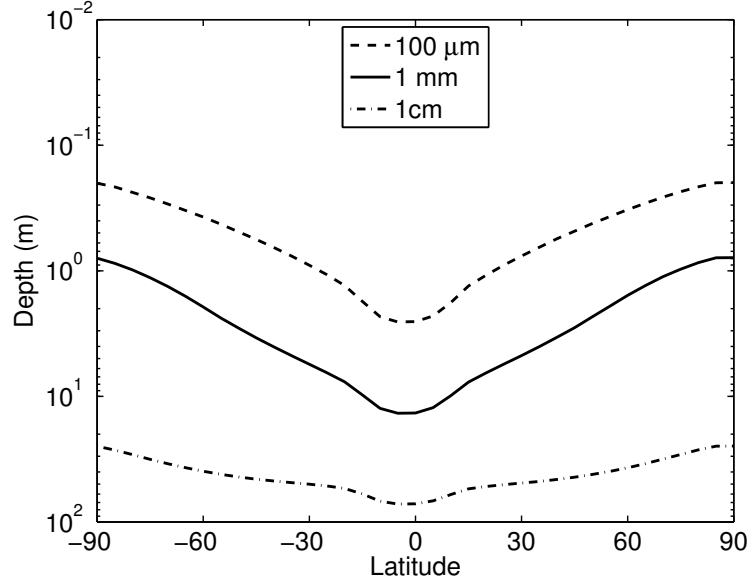


Figure 5.7 Depth to ice as in Fig. 5.4 but for 2 Gyr, the estimated age of the Themis parent body breakup.

The model uses the surface temperature to calculate the thermal evolution of 133P/Elst-Pizarro with time. Figure 5.6 shows the thermal evolution of 133P/Elst-Pizarro for a dust mantle and constant orbital parameters. The ice retreats rapidly initially, and then more gradually as the thickness of the diffusion barrier increases and the temperature amplitudes decay with depth.

Figure 5.7 shows ice depths after 2 Gyr, which would be applicable if 133P/Elst-Pizarro were a direct fragment of the Themis parent body rather than the Beagle parent body. For grain sizes of $100\ \mu\text{m}$, the depth to the ice is 0.20–2.6 m. For the 1 mm grain size, the depth to the ice is 0.8–14 m, and for 1 cm, 25–72 m. The season skin depth is 0.36 m (Table 5.5), which is consistent with the model predictions by Schorghofer (2008). For large grain sizes, the depths to ice are much greater and consistent with the burial depths calculated by Prialnik & Rosenberg (2009). The latitudinal differences in depth to ice are more pronounced after 2 Gyr than after 10 Myr (compare Figs. 5.4 and 5.7), because differences in retreat rate have had more time to evolve.

5.4 Discussion

5.4.1 Spin State of 133P/Elst-Pizarro

Lightcurve inversion is a powerful technique that can simultaneously solve for the spin and pole of an asteroid. We have applied this technique to data collected from 2002 - 2011 for the MBC 133P/Elst-Pizarro, resulting in a precise rotation period and strong constraints on the obliquity of this MBC. Delahodde et al. (2004) use a dense data set (that was not used in our analyses) within a single epoch to derive a precise rotation period for 133P/Elst-Pizarro. We use a much more sparse data set over a much longer baseline to derive a period of 3.47112 ± 0.00011 h. Thus our rotation period is consistent with the Delahodde et al. (2004) estimate, but not as precise. The consistency between our rotation period and the Delahodde et al. (2004) estimate suggests that the spin state of 133P/Elst-Pizarro is not notably affected by its cometary nature and is relatively stable.

In this paper, we find two degenerate spin pole orientations of 133P/Elst-Pizarro are $\lambda_{ecl,1} = 103^\circ \pm 31^\circ$, $\beta_{ecl,1} = 12^\circ \pm 28^\circ$ and $\lambda_{ecl,2} = 284^\circ \pm 30^\circ$, $\beta_{ecl,2} = 14^\circ \pm 28^\circ$. The lightcurve inversion model produces solutions in units of ecliptic coordinates (longitude and latitude) that are defined with respect to the orbit of 133P/Elst-Pizarro. The inclination of 133P/Elst-Pizarro's orbit is small, $i=1.4^\circ$, so the inclination can be disregarded for our solutions, and we find that the obliquity of 133P/Elst-Pizarro is constrained to $\varepsilon \geq 75^\circ$.

Toth (2006) used modeled light curves to constrain the pole of 133P/Elst-Pizarro using a single 2002 epoch obtained from Hsieh et al. (2004). He suggests four possible pole orientations of $\lambda_{1,2} = 140^\circ$, $\beta_{1,2} = \pm 60^\circ$ and $\lambda_{3,4} = 220^\circ$, $\beta_{3,4} = \pm 60^\circ$. Toth (2006) attempts to remove the degeneracy by considering 133P/Elst-Pizarro's activity is seasonally modulated and assuming the angular momentum vector behaves asymptotically to suggest the spin pole is orientated towards that aphelion direction of 133P/Elst-Pizarro's orbit. Therefore, Toth (2006) constrain their pole orientation estimates to $\lambda_{1,2} = 140^\circ$, $\beta_{1,2} = \pm 60^\circ$, but do not provide errors estimates on these solutions. Using the same assumptions to remove the degeneracy in our solutions would result in a rotational spin axis of $\lambda_{ecl,1} =$

$103^\circ \pm 31^\circ$, $\beta_{ecl,1}=12^\circ \pm 28^\circ$ for 133P/Elst-Pizarro. In contrast to Toth (2006), our data indicates the rotational spin pole of 133P/Elst-Pizarro is highly inclined, confirming the predictions made by Schorghofer (2008); Prialnik & Rosenberg (2009), and Hsieh et al. (2010).

Schorghofer (2008) found that ice in the shallow subsurface of asteroids can have a longevity comparable to the lifetime of the solar system. The model predicts asteroids with high obliquities can maintain low mean annual surface temperatures, and MBCs are likely to be highly inclined. In a separate study, Prialnik & Rosenberg (2009) have analyzed the longevity of ice for this object using a detailed 3-D thermal evolutionary calculation of heat transport in the nucleus. They find that only crystalline water ice (other species are too volatile) can survive in the nucleus at depths ranging from ~ 50 to 150 meters. The Prialnik & Rosenberg (2009) study also finds that the long-term survivability of crystalline water ice depends on the spin tilt angle, and they predict that the spin axis of 133P/Elst-Pizarro will have a large obliquity.

Although we have used an extensive set of data from 2002 through 2011, there are rather large uncertainties for 133P/Elst-Pizarro’s ecliptic latitude, and we are unable to state the true obliquity of 133P/Elst-Pizarro. The large uncertainties are likely due to the small size of 133P/Elst-Pizarro, making it difficult to obtain high signal to noise ratio observations. Hsieh et al. (2010) performed lightcurve projections for various pole orientations and demonstrate that some pole orientations produce small variations in lightcurve amplitude between different epochs. The lightcurve amplitudes from our observations are shown in Table 5.3. The small changes in amplitude variation imply that differentiating between obliquities requires high signal to noise ratio data, and is likely the reason we are unable to derive a highly accurate obliquity.

5.4.2 Water Ice in 133P/Elst-Pizarro

Asteroid parent bodies are hypothesized to have undergone heating through the radioactive decay of ^{26}Al (Grimm & McSween 1989; Wilson et al. 1999; Cohen & Coker 2000; Brearley

2006). Models suggest heating begin in the cores of asteroid parent bodies and depending on the various physical properties of the body, aqueous alteration can spread as far as the surface Wilson et al. (1999); Cohen & Coker (2000). 133P/Elst-Pizarro is dynamically associated with the Beagle family, a sub-family of the Themis asteroids (Hsieh et al. 2006; Nesvorný et al. 2008). As discussed in Chapters 3 and 4, spectroscopic observations of the Themis and Beagle families show a large fraction of members with aqueously altered mineral absorption features. However, our models suggests that ice is likely near the surface of 133P/Elst-Pizarro and the recurrent activity suggests that the ice reservoir is relatively large (Hsieh et al. 2004; Hsieh 2009). These data suggest that while the Themis parent body clearly experienced aqueous alteration, the Beagle family originated from a portion of Themis/Beagle parent body where water ice was preserved.

5.4.3 Detecting New MBCs

Extending the insights we have presented here on 133P/Elst-Pizarro to other MBCs, small, dynamically old (a few billion years) asteroids will likely have depths to ice much greater than younger asteroids of a similar size. This hypothesis has important implications on the detection of MBCs. Collisional impacts is a possible mechanism that initiates the sublimation of volatiles in main belt comets (Hsieh et al. 2004; Hsieh & Jewitt 2006; Jewitt 2012). However, the material ejected during impacts is related to the size of the impactor and due to the size distribution of objects in the main asteroid belt, large impacts will occur much less frequently than small impacts (Jewitt 2012, and references within). Although the details are beyond the scope of this dissertation, assuming a volatile-rich asteroid formed initially with ice extending all the way to the surface, our models imply that small, dynamically old asteroids are able to preserve subsurface ice for long time spans, but they are likely to have larger dust mantles covering the buried ice. Thus, dynamically old MBCs may be less likely to become activated as they will require larger impacts than dynamically young MBCs and are likely to be rare. In contrast, dynamically young asteroids will have ice closer to their surfaces and may have a higher probability of becoming activated.

Other asteroids are likely to be MBCs, but as of this time, have been difficult to find. With large scale surveys such as PanSTARRS and LSST, there will soon be a large data set for which lightcurve inversion can be used to compute the spin and pole of thousands of asteroids. Understanding the commonalities among the MBCs and their physical characteristics will help to determine if these active asteroids have distinct characteristics that can be used to identify as of yet undiscovered MBCs.

5.5 Summary

Using photometric lightcurves of 133P/Elst-Pizarro obtained from 2002 through 2011 and lightcurve inversion, we have attempted to characterize the nucleus of this main belt comet. In particular,

1. We have determined the rotation period of $P = 3.47112 \pm 0.00011$ hrs, consistent with Delahodde et al. (2004) estimate.
2. We have constrained the pole orientation to $\lambda_{1,2} = 140^\circ$, $\beta_{1,2} = \pm 60^\circ$ and $\lambda_{3,4} = 220^\circ$, $\beta_{3,4} = \pm 60^\circ$, corresponding to an obliquity of $\sim 75^\circ$.
3. The high obliquity pole is consistent with models for survivability of ice over the age of the solar system.
4. We find the mean depth to ice ranges from 0.07-0.18 m, 0.23-0.97 m, and 2.1-5.1 m for 100 μm , 1 mm, and 1 cm grain sizes, respectively, when using a young dynamical age (~ 10 Myr for the Beagle asteroids). The depth to increase to 0.2-2.6 m, 0.8-14 m, and 25-72 m for 100 μm , 1 mm, and 1 cm grain sizes, respectively, when using an older dynamical age (2 Gyr for the Themis family).

References

- Boehnhardt, H., Schulz, R., Tozzi, G. P., Rauer, H., & Sekanina, Z. 1996, IAU Circ., 6495, 2
- Brearley, A. J. 2006, *The Action of Water*, ed. Lauretta, D. S. & McSween, H. Y., 584–624
- Cohen, B. A. & Coker, R. F. 2000, *Icarus*, 145, 369
- Coradini, A., Capaccioni, F., Erard, S., Arnold, G., De Sanctis, M. C., Filacchione, G., Tosi, F., Barucci, M. A., Capria, M. T., Ammannito, E., Grassi, D., Piccioni, G., Giuppi, S., Bellucci, G., Benkhoff, J., Bibring, J. P., Blanco, A., Blecka, M., Bockelee-Morvan, D., Carraro, F., Carlson, R., Carsenty, U., Cerroni, P., Colangeli, L., Combes, M., Combi, M., Crovisier, J., Drossart, P., Encrenaz, E. T., Federico, C., Fink, U., Fonti, S., Giacomini, L., Ip, W. H., Jaumann, R., Kuehrt, E., Langevin, Y., Magni, G., McCord, T., Mennella, V., Mottola, S., Neukum, G., Orofino, V., Palumbo, P., Schade, U., Schmitt, B., Taylor, F., Tiphene, D., & Tozzi, G. 2011, *Science*, 334, 492
- Cremers, C. J. & Birkebak, R. C. 1971, in *Lunar and Planetary Science Conference Proceedings*, Vol. 2, Lunar and Planetary Science Conference Proceedings, 2311
- Delahodde, C. E., Hainaut, O. R., Dotto, E., & Campins, H. 2004, in *Bulletin of the American Astronomical Society*, Vol. 36, AAS/Division for Planetary Sciences Meeting Abstracts #36, 1148
- Delbo', M. & Tanga, P. 2009, *Planet. Space Sci.*, 57, 259

- Durech, J., Kaasalainen, M., Warner, B. D., Fauerbach, M., Marks, S. A., Fauvaud, S., Fauvaud, M., Vugnon, J.-M., Pilcher, F., Bernasconi, L., & Behrend, R. 2009, *A&A*, 493, 291
- Durech, J., Sidorin, V., & Kaasalainen, M. 2010, *A&A*, 513, A46+
- Evans, III, R. B., Watson, G. M., & Mason, E. A. 1961, *J. Chem. Phys.*, 35, 2076
- Fanale, F. P. & Salvail, J. R. 1984, *Icarus*, 60, 476
- Grimm, R. E. & McSween, Jr., H. Y. 1989, *Icarus*, 82, 244
- Groussin, O., A’Hearn, M. F., Li, J.-Y., Thomas, P. C., Sunshine, J. M., Lisse, C. M., Meech, K. J., Farnham, T. L., Feaga, L. M., & Delamere, W. A. 2007, *Icarus*, 187, 16
- Gulkis, S., Allen, M., von Allmen, P., Beaudin, G., Biver, N., Bockelée-Morvan, D., Choukroun, M., Crovisier, J., Davidsson, B. J. R., Encrenaz, P., Encrenaz, T., Frerking, M., Hartogh, P., Hofstadter, M., Ip, W.-H., Janssen, M., Jarchow, C., Keihm, S., Lee, S., Lellouch, E., Leyrat, C., Rezac, L., Schloerb, F. P., & Spilker, T. 2015, *Science*, 347, 709
- Hsieh, H. H. 2009, *A&A*, 505, 1297
- Hsieh, H. H., Hainaut, O., Novaković, B., Bolin, B., Denneau, L., Fitzsimmons, A., Haghighipour, N., Kleyna, J., Kokotanekova, R., Lacerda, P., Meech, K. J., Micheli, M., Moskovitz, N., Schunova, E., Snodgrass, C., Wainscoat, R. J., Wasserman, L., & Waszczak, A. 2015, *ApJ*, 800, L16
- Hsieh, H. H. & Jewitt, D. 2006, *Science*, 312, 561
- Hsieh, H. H., Jewitt, D., Lacerda, P., Lowry, S. C., & Snodgrass, C. 2010, *MNRAS*, 403, 363
- Hsieh, H. H., Jewitt, D., & Pittichova, J. 2006, *IAU Circ.*, 8704, 3
- Hsieh, H. H., Jewitt, D. C., & Fernández, Y. R. 2004, *AJ*, 127, 2997

- Hsieh, H. H., Meech, K. J., & Pittichová, J. 2011, *ApJ*, 736, L18
- Jenniskens, P., Blake, D. F., & Kouchi, A. 1998, in *Astrophysics and Space Science Library*, Vol. 227, *Solar System Ices*, ed. B. Schmitt, C. de Bergh, & M. Festou, 139
- Jewitt, D. 2012, *AJ*, 143, 66
- Jewitt, D., Ishiguro, M., Weaver, H., Agarwal, J., Mutchler, M., & Larson, S. 2014, *AJ*, 147, 117
- Kaasalainen, M. & Torppa, J. 2001, *Icarus*, 153, 24
- Kaasalainen, M., Torppa, J., & Muinonen, K. 2001, *Icarus*, 153, 37
- Krot, A. N., Hutcheon, I. D., Brearley, A. J., Pravdivtseva, O. V., Petaev, M. I., & Hohenberg, C. M. 2006, *Timescales and Settings for Alteration of Chondritic Meteorites*, ed. Lauretta, D. S. & McSween, H. Y., 525–553
- Lide, D. R. 2003, *CRC Handbook of Chemistry and Physics*, 84th edn., ed. D. R. Lide (CRC Press)
- Mason, E. A. & Malinauskas, A. P. 1983, *Chemical Engineering Monographs*, Vol. 17, *Gas Transport in Porous Media: The Dusty-Gas Model* (Amsterdam: Elsevier)
- Mason, E. A., Malinauskas, A. P., & Evans, III, R. B. 1967, *J. Chem. Phys.*, 46, 3199
- Nesvorný, D., Bottke, W. F., Vokrouhlický, D., Sykes, M., Lien, D. J., & Stansberry, J. 2008, *ApJ*, 679, L143
- Novaković, B., Hsieh, H. H., & Cellino, A. 2012, *MNRAS*, 424, 1432
- Prialnik, D. & Rosenberg, E. D. 2009, *MNRAS*, 399, L79
- Sakatani, N., Ogawa, K., Iijima, Y., Honda, R., & Tanaka, S. 2012, in *Lunar and Planetary Science Conference*, Vol. 43, *Lunar and Planetary Science Conference*, 2000
- Schorghofer, N. 2008, *ApJ*, 682, 697

Schorghofer, N. 2010, *Icarus*, 208, 598

Schotte, W. 1960, *AIChE Journal*, 6, 63

Spencer, J. R., Lebofsky, L. A., & Sykes, M. V. 1989, *Icarus*, 78, 337

Toth, I. 2006, *A&A*, 446, 333

Wilson, L., Keil, K., Browning, L. B., Krot, A. N., & Bourcier, W. 1999, *Meteoritics and Planetary Science*, 34, 541

Winter, D. F. & Saari, J. M. 1969, *ApJ*, 156, 1135

Chapter 6

Conclusion

Our ability to interpret remote sensing data greatly influences our effectiveness in assessing the compositions of solar system bodies. C-complex asteroids are low-albedo, primitive asteroids that despite the presence of opaques, which are known to mask spectral features (Clark 1981), have several visible and NIR absorption features (Lebofsky et al. 1981; Vilas & Gaffey 1989; Vilas 1994) associated with aqueously altered minerals (Rivkin et al. 2015, and references within). These features provide a means to characterize the mineralogies of main belt asteroids, which in comparison to other small solar system bodies (e.g. Trojan asteroids), places important constraints on where C-complex asteroids formed. Thus, the spectral features of C-complex asteroids provide key insights into the initial distribution and transport of volatiles in the solar system. In addition, the spectral features of aqueously altered minerals, which form through reactions of silicate minerals and liquid water, are an important tool to assess the water content and thermal histories of asteroid parent bodies (e.g. Castillo-Rogez & Schmidt 2010). This dissertation combines experimental and observational data to study space weathering effects on visible and NIR spectral features of C-complex asteroids in addition to the longevity of water ice in collisional disruption fragments of C-complex asteroid parent bodies.

6.1 Results from space weathering experiments

In Chapter 2, we present experiments that simulate the micrometeorite bombardment of aqueously altered minerals. We show that the response of lizardite and a mixture of cronstedtite, pyrite and siderite to laser induced space weathering is varied even within this small subset of aqueously altered minerals. Lizardite, a Mg-end member phyllosilicate, shows an increase in spectral slopes at visible wavelengths, but a slight decrease at NIR wavelengths. In contrast, the mixture, which is dominated by the Fe-end member phyllosilicate cronstedtite, initially experiences an increase in spectral slopes, but after a short period of irradiation, the slope trends reverse and instead decrease with increased irradiation (in both the visible and NIR). Our data are the first to show that non-organic minerals also experience bluer spectral slopes in response to simulated space weathering. Furthermore, although the spectral trends are varied, our experimental data show that total dehydration of phyllosilicates is not necessary for space weathering processes to be effective (i.e. produce npFe^0 and/or Britt-Pieters particles).

The petrographic and chemical characterizations of aqueously altered meteorites show that phyllosilicates evolve from Fe-rich cronstedtite to Mg-rich serpentines with progressive aqueous alteration (Rubin 2007; Howard et al. 2009, 2011). If cronstedtite is the mineral responsible for the bluer spectral slopes seen in the cronstedtite, pyrite and siderite mixture, then our data show a potential space weathering trend that depends on the degree of aqueous alteration experienced by asteroid parent bodies.

6.2 Results from visible and near-infrared observations

In Chapter 3, we use visible spectroscopic data and WISE derived albedo data to compare the albedo and spectral trends of the Themis and Beagle asteroid families. These two C-complex asteroid families originated from the same parent body and thus have a unique relationship that allows us to study space weathering trends on C-complex asteroids where the effects of mineralogical differences are minimized. Comparisons of the spectral

and albedo data suggest C-complex asteroids with Themis and Beagle-type mineralogies experience slope reddening and darkening in response to space weathering. In addition, we found $\sim 60\%$ (13 of 22) of Themis asteroids and $\sim 80\%$ (20 of 23) of Beagle asteroids have B-type taxonomies.

In Chapter 4, we present visible and NIR spectrophotometry data of the Themis and Beagle asteroid families. Our data show no significant differences between the two families and suggest space weathering processes on C-complex asteroids (with Themis and Beagle-type mineralogies) have a negligible effect at NIR wavelengths as compared to visible wavelengths. In addition, almost all of the asteroids show prominent absorption features centered near 1.0-1.5 μm . The large fraction of NIR absorption features, along with the high fraction of B-type taxonomies in the Themis and Beagle asteroids, and the association of this taxonomic type with aqueously altered minerals (Clark et al. 2010; Yang & Jewitt 2010), suggests the Themis and Beagle parent body experienced extensive aqueous alteration. These data place important constraints on geophysical models (Castillo-Rogez & Schmidt 2010) that explore the formation time and starting composition of the Themis and Beagle parent body.

In contrast to our NIR data, the visible spectra of the Themis and Beagle asteroids show few phyllosilicate features, however, our visible spectroscopic data show a high fraction of phyllosilicate features in the Veritas asteroids. Although more observations of the Veritas asteroids are needed, Ziffer et al. (2008) and Chapman et al. (2009) see no NIR absorption features in the Veritas asteroids. Thus, although NIR wavelengths appear to be a better region to assess the mineralogy of the Themis and Beagle asteroids, the Veritas spectral features indicate that both visible and NIR data are both necessary to assess mineralogy in C-complex asteroids. In addition, the differences in spectral features as well as the contrasting albedos between the similarly aged Beagle and Veritas asteroid families suggest the Veritas asteroids have a different composition than the Beagle and Themis asteroids. Therefore, our data emphasize the importance of accounting for mineralogy when studying space weathering trends among the broad C-complex class.

6.3 Results from photometric studies of the MBC 133P/Elst-Pizarro

In Chapter 5, we present visible wavelength photometry data of the main belt comet 133P/Elst-Pizarro, which is dynamically associated with the Themis and Beagle asteroid families. Using data collected from 2002 through 2011 along with light curve inversion, we constrain the rotational spin axis to two degenerate solutions: $\lambda_{ecl,1} = 103^\circ \pm 31^\circ$, $\beta_{ecl,1} = 12^\circ \pm 28^\circ$ and $\lambda_{ecl,2} = 284^\circ \pm 30^\circ$, $\beta_{ecl,2} = 14^\circ \pm 28^\circ$. Therefore our data suggest the spin axis of 133P is highly inclined, having an obliquity as large as 75° .

Although the uncertainties are large for β , we assume an obliquity of $\sim 75^\circ$ for use in our thermal and ice evolution models. Assuming the ice in 133P/Elst-Pizarro extended all the way to its surface following the break up of the Beagle parent body, over a time period of 10 Myr the ice is expected to retreat to depths of 0.07-5.1 m. If assuming 133P/Elst-Pizarro instead originated from the break up of the Themis parent body, then the ice is shown to retreat to depths of 0.2-72 m. The depth to the ice is strongly dependent on the grain sizes used in the model, however, it appears that water ice is able to survive within the interior of asteroids over the age of the solar system (Schorghofer 2008; Prialnik & Rosenberg 2009).

6.4 Summary

In this dissertation, we have used visible and NIR wavelength observations of the Beagle and Themis families, visible wavelength photometric data and thermal models of an MBC associated with these two families, and space weathering experiments on aqueously altered minerals to conduct a comprehensive study on the evolution of water in the carbonaceous asteroids.

Our Themis and Beagle spectroscopic data along with the space weathering experiments provide valuable insights into the trends we expect to see among C-complex asteroids. In agreement with the trends observed by Lazzarin et al. (2006), our Themis and Beagle asteroid observations suggest C-complex asteroids become spectrally redder at visible

wavelengths as they age. Furthermore, when comparing the Beagle and Veritas asteroid observations, it appears the decrease in visible spectral slopes observed by Nesvorný et al. (2005) among C-complex asteroid families is a result of mineralogical differences. However, there is still a diversity in the spectral trends of experimentally space weathered CC meteorites where some meteorites become spectrally redder (Moroz et al. 2004; Vernazza et al. 2013) and others show a decrease in spectral slopes (e.g. Hiroi et al. 2004). Our space weathering experiments focused upon the spectral behavior of phyllosilicates, which are abundant in several CC meteorite groups (Cloutis et al. 2011), to investigate what components of CCs cause the observed discrepancy in CC meteorite space weathering experiments. More experiments are needed to establish the contribution of phyllosilicates on the space weathering trends of CCs and therefore C-complex asteroids. However if the response of phyllosilicates are found to dominate the spectral trends of CCs, our experiments suggest that some C-complex asteroid families should show bluer spectral slopes as they age.

Perhaps the best tool to assess the compositions of asteroids is linking them with meteorites. However, the varied mineralogy of C-complex asteroids along with complex space weathering trends observed in meteorites (e.g. Hiroi et al. 2004; Vernazza et al. 2013) make the compositions of C-complex asteroids difficult to constrain. However, our data suggest space weathering trends may be able to differentiate between asteroids that have experienced varying degrees of aqueous alteration. Therefore space weathering may prove to be a tool that we can use to better assess the compositions of C-complex asteroids through remote sensing data. Additionally, our NIR observations suggest NIR wavelength observations may be an effective way to assess C-complex asteroid compositions while avoiding the complications of space weathering and/or regolith processes that manifest in visible wavelength data.

We show that simultaneous visible/NIR photometry is a powerful tool to assess the aqueous alteration histories of small, C-complex asteroids for which spectroscopy is not viable. Thus, when using NIR wavelength data on asteroid families dynamically associated

with MBCs, geophysical models such as that developed by Castillo-Rogez & Schmidt (2010) can be used to constrain formation times and thermal histories of icy C-complex parent bodies.

In conclusion, we show the strength of combining observational data, experimental data and model data and the effectiveness of such a comprehensive data set in providing valuable insights on the thermal and aqueous evolution of carbonaceous main belt asteroids.

References

- Castillo-Rogez, J. C. & Schmidt, B. E. 2010, *Geophys. Res. Lett.*, **37**, L10202
- Chapman, C. R., Enke, B., Merline, W. J., Nesvorný, D., Tamblyn, P., & Young, E. F. 2009, in *Lunar and Planetary Science Conference*, Vol. 40, Lunar and Planetary Science Conference, 2258
- Clark, B. E., Ziffer, J., Nesvorny, D., Campins, H., Rivkin, A. S., Hiroi, T., Barucci, M. A., Fulchignoni, M., Binzel, R. P., Fornasier, S., DeMeo, F., Ockert-Bell, M. E., Licandro, J., & Mothé-Diniz, T. 2010, *Journal of Geophysical Research (Planets)*, **115**, 6005
- Clark, R. N. 1981, *J. Geophys. Res.*, **86**, 3074
- Cloutis, E. A., Hiroi, T., Gaffey, M. J., Alexander, C. M. O. ., & Mann, P. 2011, *Icarus*, **212**, 180
- Hiroi, T., Pieters, C. M., Rutherford, M. J., Zolensky, M. E., Sasaki, S., Ueda, Y., & Miyamoto, M. 2004, in *Lunar and Planetary Inst. Technical Report*, Vol. 35, Lunar and Planetary Science Conference, ed. S. Mackwell & E. Stansbery, 1616
- Howard, K. T., Benedix, G. K., Bland, P. A., & Cressey, G. 2009, *Geochimica et Cosmochimica Acta*, **73**, 4576
- Howard, K. T., Benedix, G. K., Bland, P. A., & Cressey, G. 2011, *Geochimica et Cosmochimica Acta*, **75**, 2735

- Lazzarin, M., Marchi, S., Moroz, L. V., Brunetto, R., Magrin, S., Paolicchi, P., & Strazzulla, G. 2006, *ApJ*, 647, L179
- Lebofsky, L. A., Feierberg, M. A., Tokunaga, A. T., Larson, H. P., & Johnson, J. R. 1981, *Icarus*, 48, 453
- Moroz, L. V., Hiroi, T., Shingareva, T. V., Basilevsky, A. T., Fisenko, A. V., Semjonova, L. F., & Pieters, C. M. 2004, in *Lunar and Planetary Science Conference*, Vol. 35, *Lunar and Planetary Science Conference*, ed. S. Mackwell & E. Stansbery, 1279
- Nesvorný, D., Jedicke, R., Whiteley, R. J., & Ivezić, Ž. 2005, *Icarus*, 173, 132
- Prialnik, D. & Rosenberg, E. D. 2009, *MNRAS*, 399, L79
- Rivkin, A. S., Campins, H., Emery, J. P., Howell, E. S., Licandro, J., Takir, D., & Vilas, F. 2015, *ArXiv e-prints*
- Rubin, A. E. 2007, in *Lunar and Planetary Science Conference*, Vol. 38, *Lunar and Planetary Science Conference*, 1230
- Schorghofer, N. 2008, *ApJ*, 682, 697
- Vernazza, P., Fulvio, D., Brunetto, R., Emery, J. P., Dukes, C. A., Cipriani, F., Witasse, O., Schaible, M. J., Zanda, B., Strazzulla, G., & Baragiola, R. A. 2013, *Icarus*, 225, 517
- Vilas, F. 1994, *Icarus*, 111, 456
- Vilas, F. & Gaffey, M. J. 1989, *Science*, 246, 790
- Yang, B. & Jewitt, D. 2010, *AJ*, 140, 692
- Ziffer, J., Campins, H., Howell, E. S., Licandro, J., Walker, M., Deshpande, R., & Hargrove, K. 2008, in *Bulletin of the American Astronomical Society*, Vol. 40, *AAS/Division for Planetary Sciences Meeting Abstracts #40*, 509

Chapter 7

Future Work

Following the completion of my dissertation, I will be taking a postdoctoral researcher position with Dr. Paul Lucey and Dr. Jeffrey Gillis-Davis at the Hawaii'i Institute of Geophysics and Planetology. As a postdoctoral researcher, I will continue to characterize main belt asteroids as well as conducting more space weathering experiments.

7.1 Space Weathering Experiments

In Chapter 2, we found that laser induced space weathering of a cronstedtite, pyrite and siderite mixture results in decrease in spectral slopes. Our goal was to test the spectral response of cronstedtite, however, we were unable to isolate the mineral from the siderite and pyrite components. Therefore, I will be conducting several more space weathering experiments to study the response of pyrite and siderite. My goal is to determine if either of these two minerals exhibit a decrease in spectral slopes and cause the bluer spectral slopes seen in the mixture although they comprise a small fraction of the cronstedtite, pyrite and siderite mixture. In contrast to cronstedtite, pyrite and siderite are more common and easier to secure pure mineral samples. I will be working with Dr. Jeffrey Gillis-Davis, who has already acquired a sample of siderite to study simulated space weathering effects on these aqueously altered minerals.

In addition, we also are planning space weathering experiments on carbonaceous chondrite meteorites, for which only a limited set of experiments (e.g. Moroz et al. 2004;

Hiroi et al. 2003). Our goal is to space weathering CM and CI meteorites over a range of petrologic grades to search for correlations in space weathering trends and the degree of aqueous alteration in these meteorites. Understanding how space weathering trends vary as a function of petrologic grade and mineralogy could allow space weathering effects to be a powerful tool to assess asteroid mineralogies remotely. However, observational studies are necessary to assess the role of regolith formation and evolution on asteroids to gain a comprehensive understanding of the regolith processes that affect spectral features in addition to space weathering.

7.2 Observations

7.2.1 Spectral trends as function of diameter

In Chapter 3, we noted trends in albedo variations with diameter, which appear to be related to previously observed variations in absorption feature frequencies on asteroids as a function of diameter (Jones et al. 1990; Vilas & Sykes 1996; Florczak et al. 1999; Fornasier et al. 2014). I plan to conduct a targeted set of observations to search for variations in absorption band depths across a range of diameters for several main belt asteroid families. Studying diameter related trends in both young and old asteroid families can provide us with valuable insight on regolith formation and evolution processes.

In Chapter 4, we find that comparison of small diameter Themis members with large diameter members suggests there may also be size related trends in the NIR regions. In contrast to the trends presented in Chapter 3, where smaller asteroids have a smaller fraction of members with phyllosilicate features, the NIR absorption band depths appear to increase with decreasing diameter. Therefore another future project is to conduct a series of observations to investigate whether diameter trends also occur at the NIR wavelengths.

7.2.2 Mineralogical maps of main belt asteroids

In conjunction with Dr. Lucey, I will be using DAWN spacecraft data to look at the variation in mineralogy across the surface of the main belt asteroid 4/Vesta. We will be using radiative transfer models along with data from the VIR spectroscopic instrument to produce mineralogical maps for Vesta. This project is an ideal extension of the studies I conducted during graduate school, as it will provide me with an amazing opportunity to combine and further develop the modeling and observational skills I have gained as a graduate student.

References

- Clark, R. N. 1999, Manual of Remote Sensing, Volume 3, Remote Sensing for the Earth Sciences, ed. A. Rencz, Vol. 3 (John Wiley and Sons), 3–58
- Florczak, M., Lazzaro, D., Mothé-Diniz, T., Angeli, C. A., & Betzler, A. S. 1999, A&AS, 134, 463
- Fornasier, S., Lantz, C., Barucci, M. A., & Lazzarin, M. 2014, Icarus, 233, 163
- Hiroi, T., Moroz, L. V., Shingareva, T. V., Basilevsky, A. T., & Pieters, C. M. 2003, in Lunar and Planetary Science Conference, Vol. 34, Lunar and Planetary Science Conference, ed. S. Mackwell & E. Stansbery, 1324
- Jones, T. D., Lebofsky, L. A., Lewis, J. S., & Marley, M. S. 1990, Icarus, 88, 172
- Moroz, L., Baratta, G., Strazzulla, G., Starukhina, L., Dotto, E., Barucci, M. A., Arnold, G., & Distefano, E. 2004, Icarus, 170, 214
- Vilas, F. & Sykes, M. V. 1996, Icarus, 124, 483

Appendix A

Complete Set of Chapter 2 Figures and Tables

The figures in this appendix show the full set of reflectance, normalized reflectance and continuum removed spectra for each experiment conducted as described in Chapter 2. In addition, the figures also show each of the reflectance, slope and band depth measurements for each experiment. The measurements are also presented in a table format for future use.

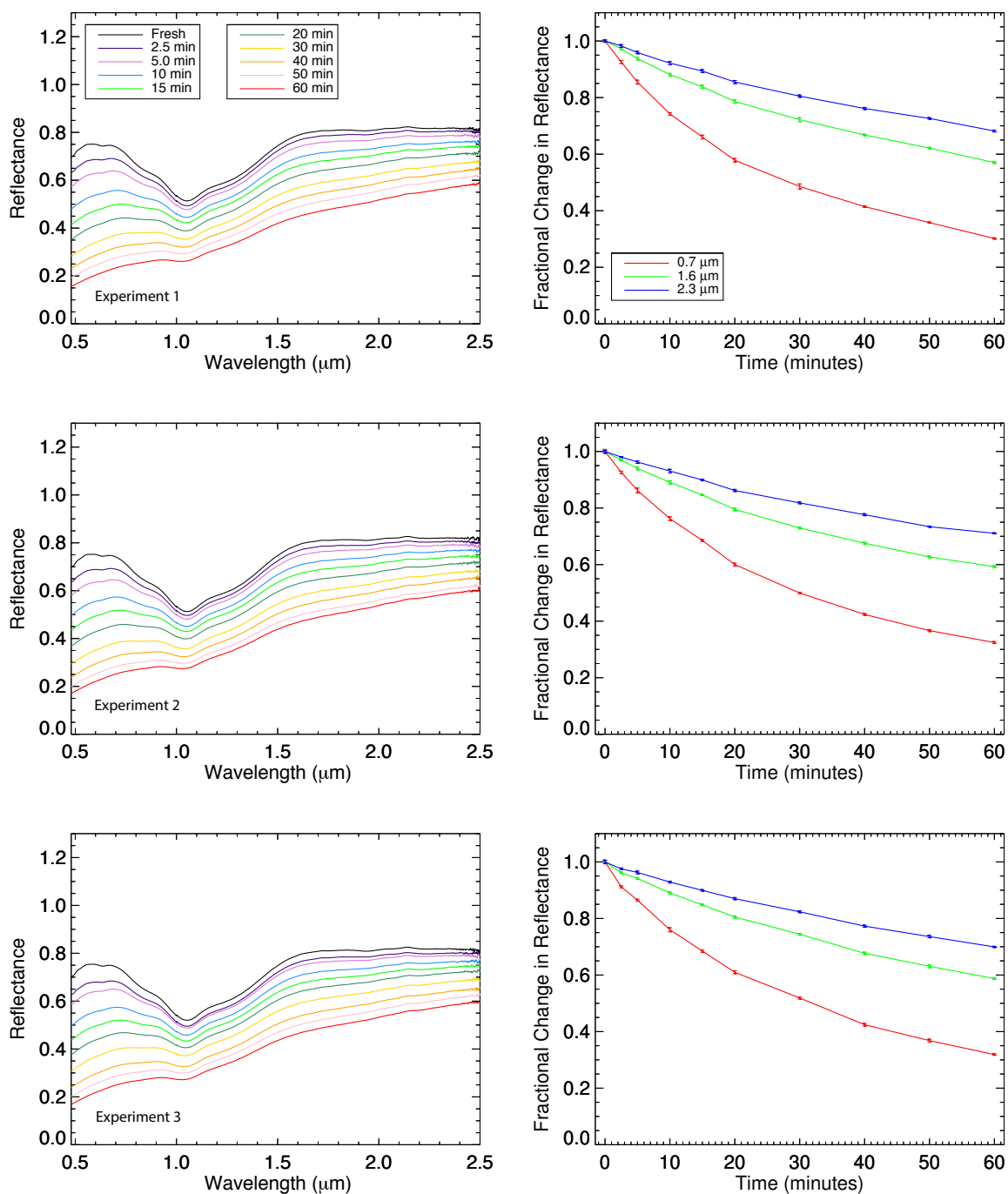


Figure A.1 *Left:* Olivine reflectance spectra as a function of irradiation time. *Right:* Reflectance variations as a function of irradiation time for visible and NIR wavelengths. Data have been normalized to the reflectance value of the fresh, non-irradiated spectrum. Each row corresponds to a different experiment.

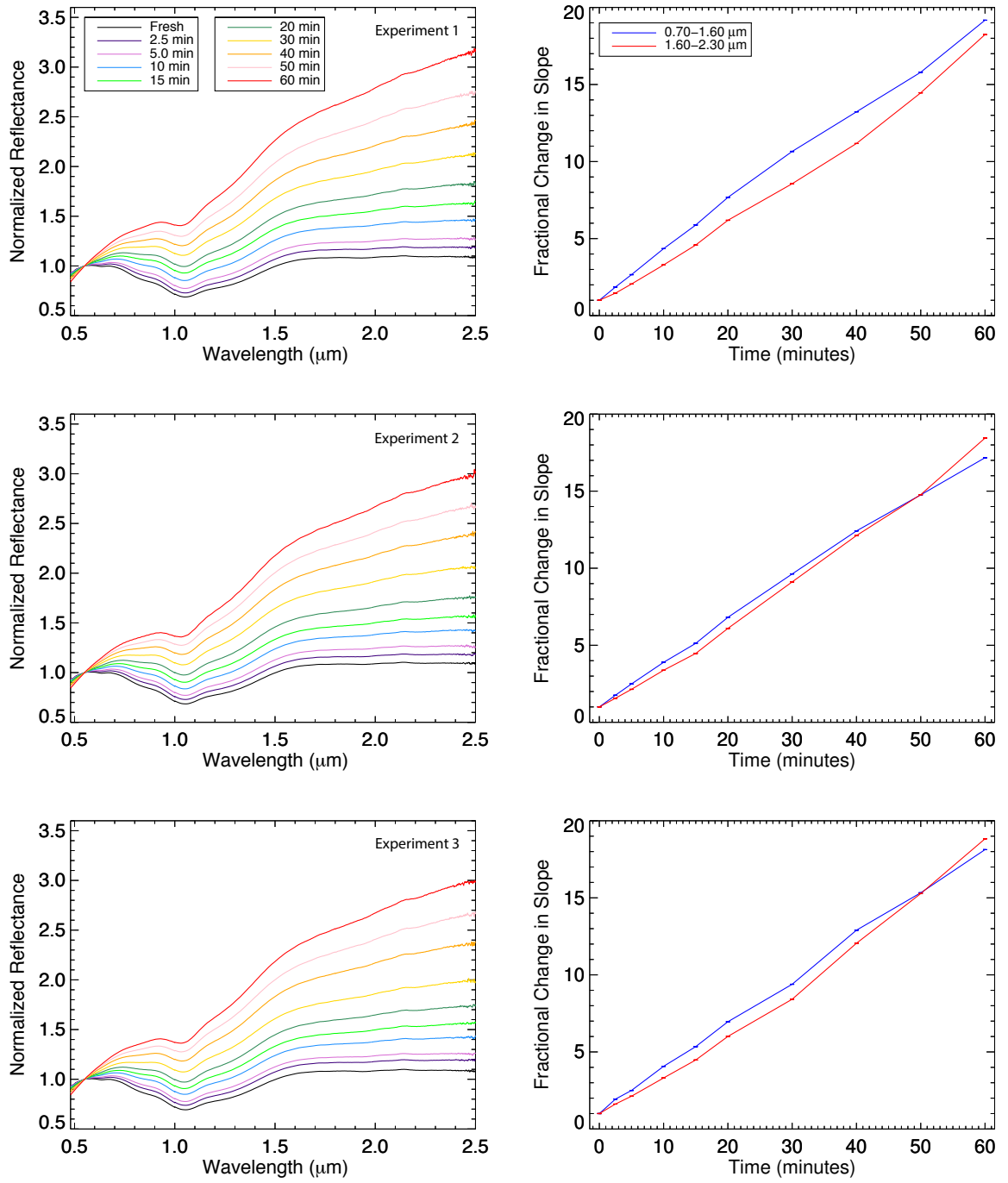


Figure A.2 *Left:* Olivine slope changes as a function of irradiation time. Spectra have been normalized to $0.55\mu\text{m}$. *Right:* Visible and NIR slope variations as a function of increased irradiation time. Data have been normalized to the slope value of the fresh, non-irradiated spectrum. Each row corresponds to a different experiment.

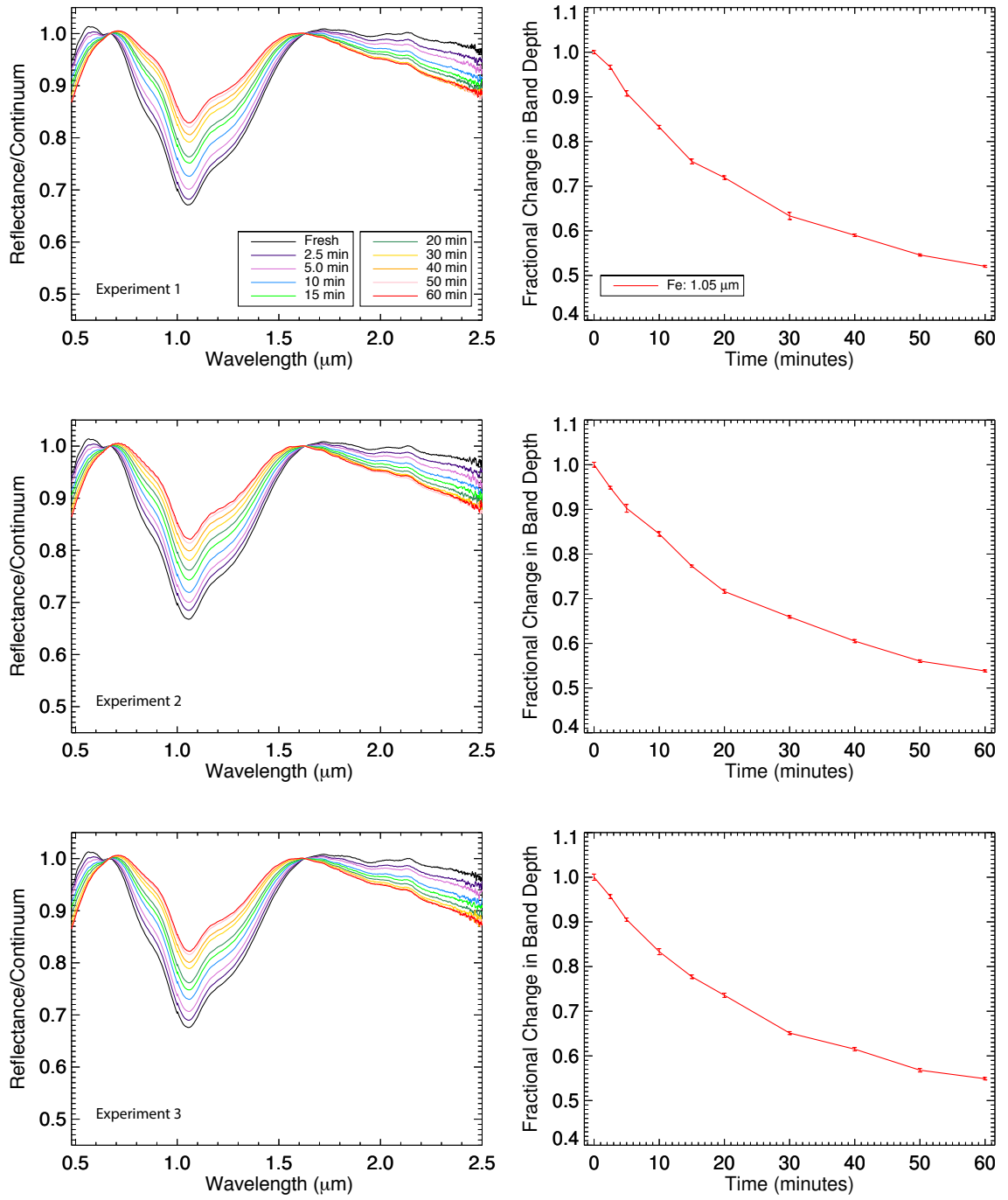


Figure A.3 *Left:* Continuum removed spectra of olivine as a function of irradiation time. *Right:* Visible and NIR band depth variations as a function of increased irradiation time. Data have been normalized to the band depth value of the fresh, non-irradiated spectrum. Each row corresponds to a different experiment.

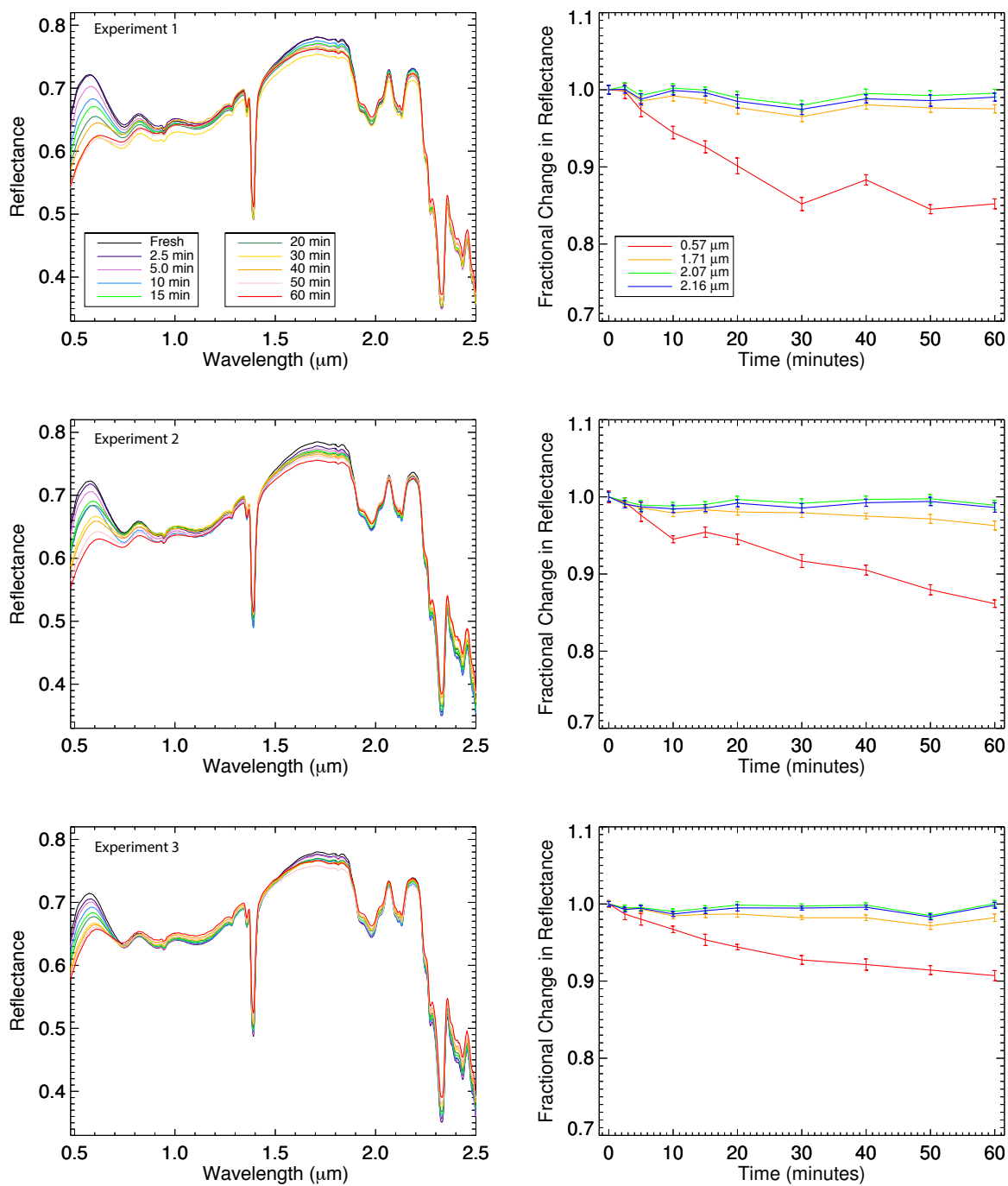


Figure A.4 *Left:* Lizardite reflectance spectra as a function of irradiation time. *Right:* Reflectance variations as a function of irradiation time for visible and NIR wavelengths. Data have been normalized to the reflectance value of the fresh, non-irradiated spectrum. Each row corresponds to a different experiment.

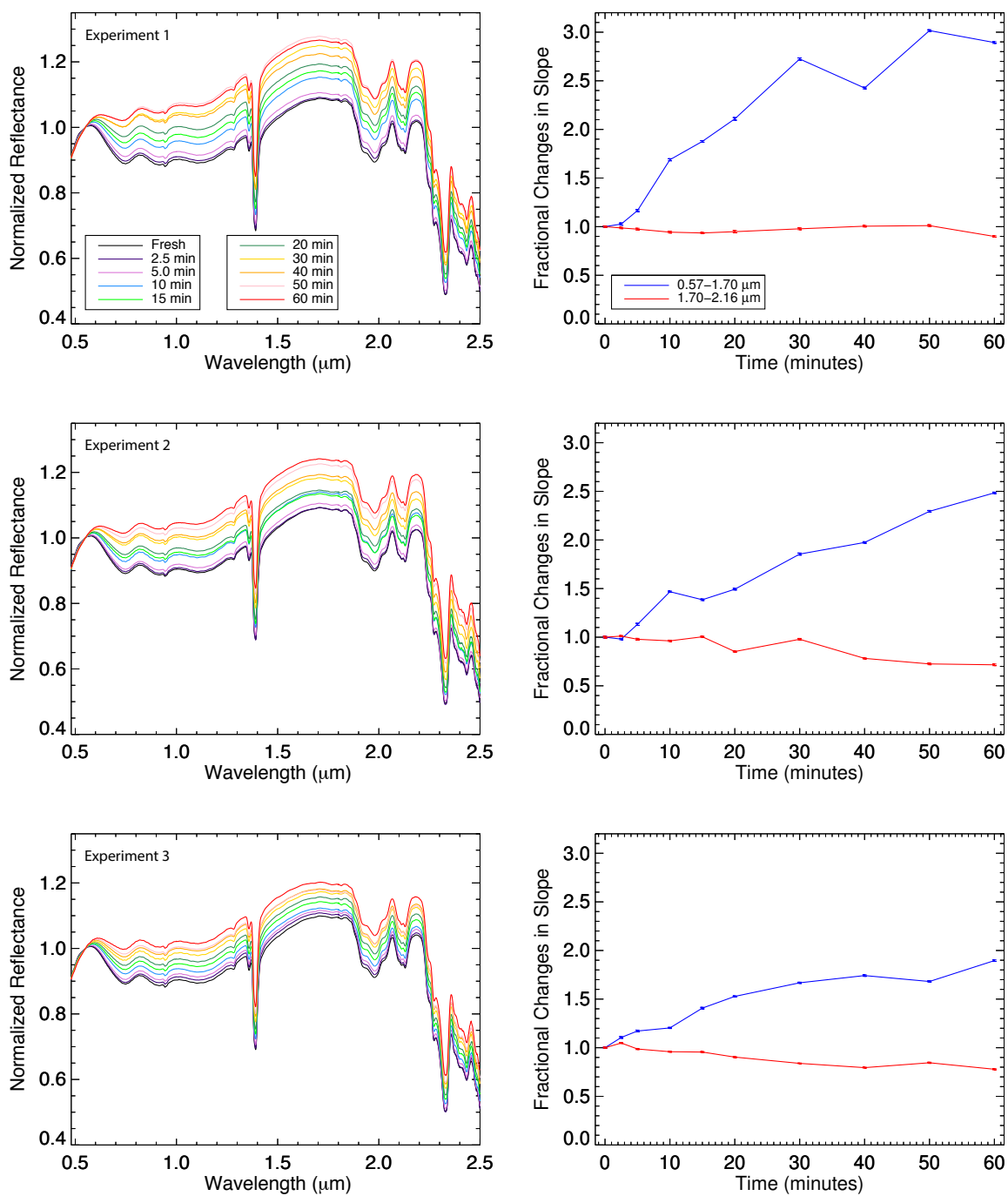


Figure A.5 *Left:* Normalized lizardite spectra as a function of irradiation time. Spectra have been normalized to 0.55 μm . *Right:* Visible and NIR slope variations as a function of increased irradiation time. Data have been normalized to the slope value of the fresh, non-irradiated spectrum. Each row corresponds to a different experiment.

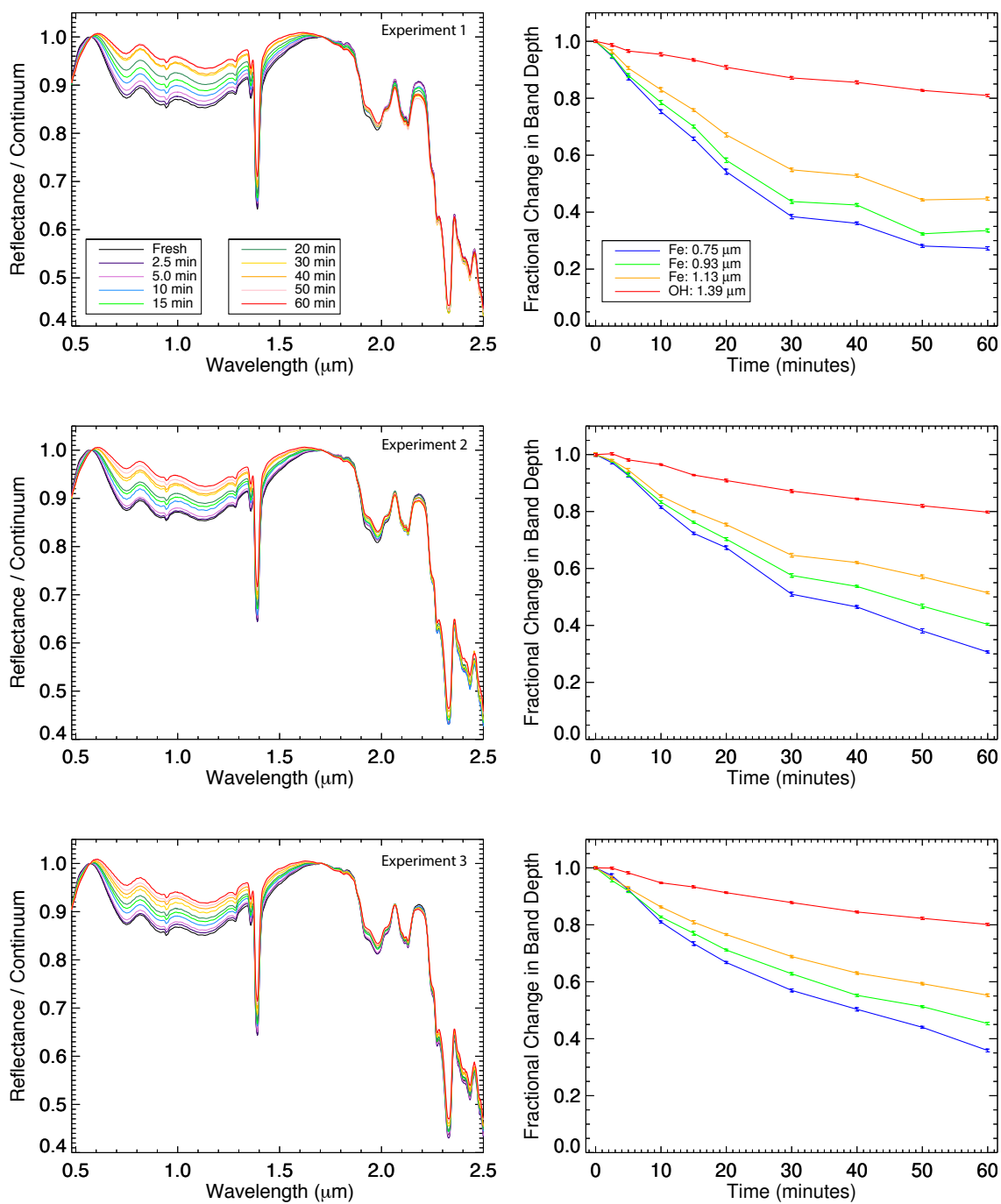


Figure A.6 *Left:* Continuum removed spectra of lizardite as a function of irradiation time. *Right:* Visible and NIR band depth variations as a function of increased irradiation time. Data have been normalized to the band depth value of the fresh, non-irradiated spectrum. Each row corresponds to a different experiment.

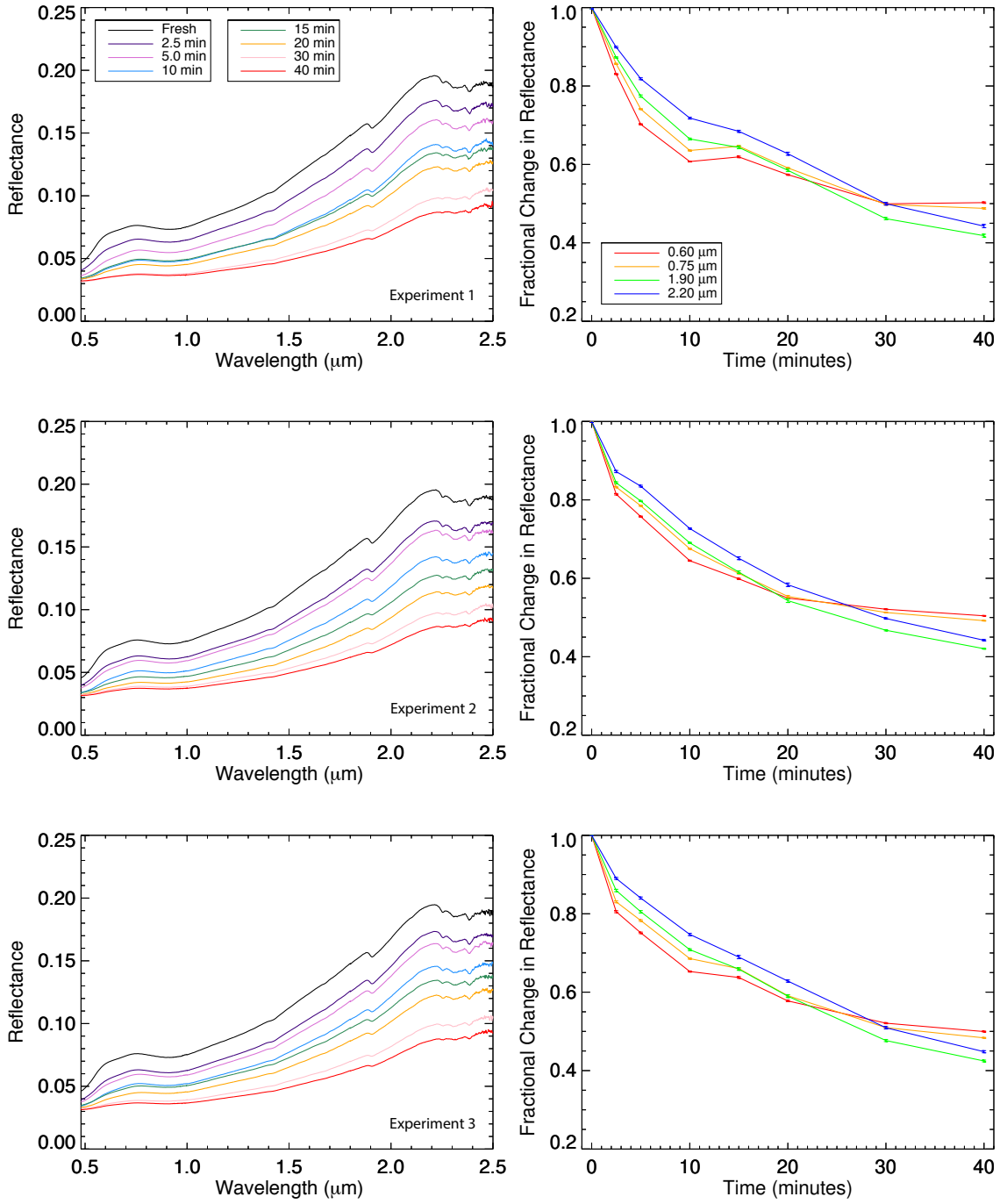


Figure A.7 *Left:* Cronstedtite reflectance spectra as a function of irradiation time. *Right:* Reflectance variations as a function of irradiation time for visible and NIR wavelengths. Data have been normalized to the reflectance value of the fresh, non-irradiated spectrum. Each row corresponds to a different experiment.

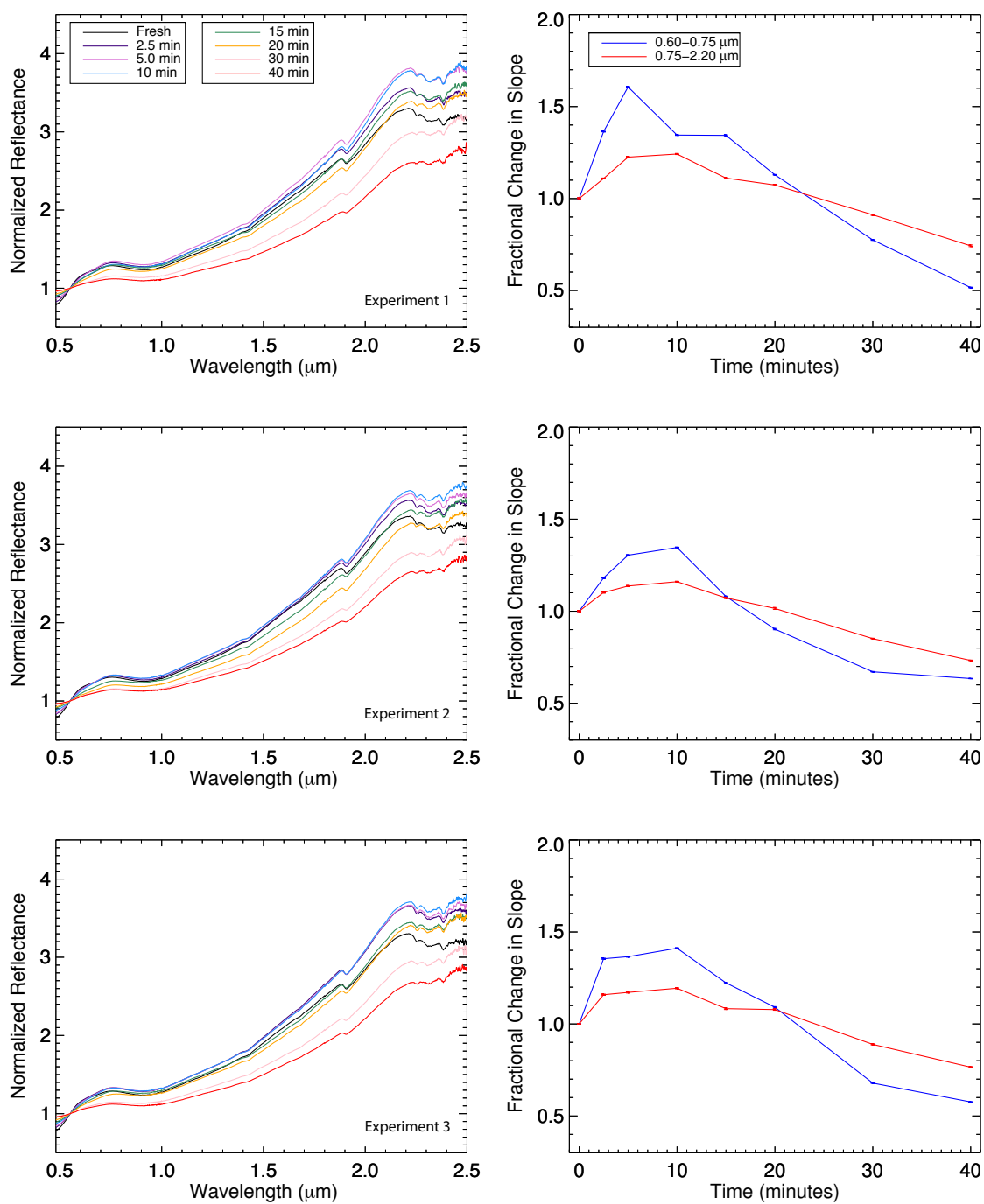


Figure A.8 Normalized constedtite spectra as a function of irradiation time. Spectra have been normalized to $0.55\mu\text{m}$. *Right:* Visible and NIR slope variations as a function of increased irradiation time. Data have been normalized to the slope value of the fresh, non-irradiated spectrum. Each row corresponds to a different experiment.

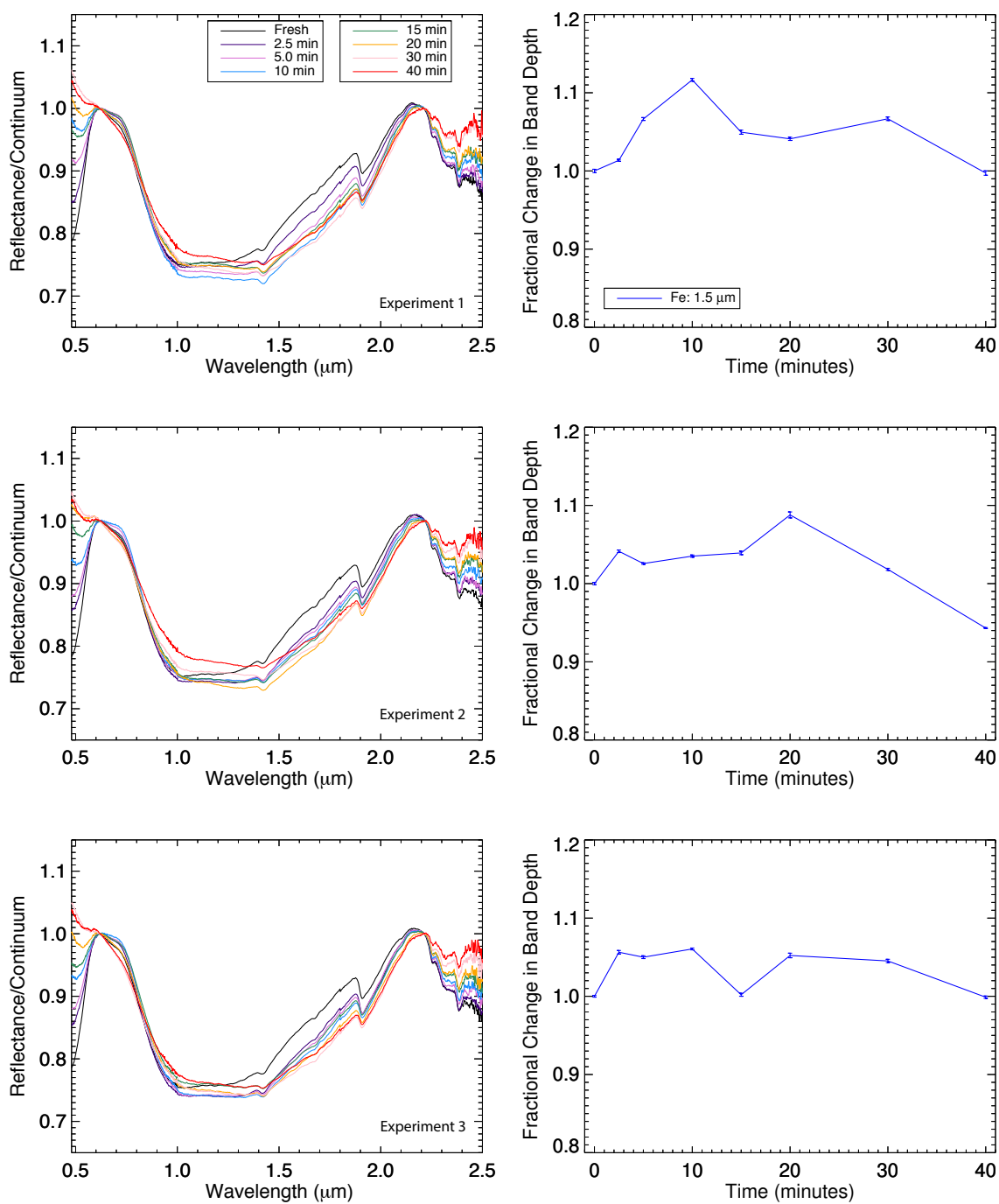


Figure A.9 *Left:* Continuum removed spectra of cronstedtite as a function of irradiation time. *Right:* Band depth variations as a function of increased irradiation time. Data have been normalized to the band depth value of the fresh, non-irradiated spectrum. Each row corresponds to a different experiment.

Table A.1. Spectral Slope Measurements

Irradiation Time (min)	Sample 1 %/μm	Sample 2 %/μm	Sample 3 %/μm	Mean %/μm
<i>Cronstedtite (Vis)</i>				
0	0.771 ± 0.003	0.821 ± 0.002	0.790 ± 0.001	0.79 ± 0.03
2.5	1.051 ± 0.002	0.970 ± 0.002	1.070 ± 0.003	1.03 ± 0.05
5.0	1.238 ± 0.002	1.071 ± 0.002	1.079 ± 0.003	1.13 ± 0.09
10.0	1.037 ± 0.002	1.106 ± 0.002	1.115 ± 0.002	1.09 ± 0.04
15.0	1.035 ± 0.003	0.887 ± 0.002	0.967 ± 0.003	0.96 ± 0.07
20.0	0.870 ± 0.002	0.742 ± 0.003	0.862 ± 0.003	0.82 ± 0.07
30.0	0.597 ± 0.002	0.551 ± 0.002	0.536 ± 0.002	0.56 ± 0.03
40.0	0.398 ± 0.003	0.521 ± 0.001	0.455 ± 0.002	0.46 ± 0.06
Total				-42% ± 5%
<i>Cronstedtite (NIR)</i>				
0	1.382 ± 0.004	1.409 ± 0.003	1.382 ± 0.001	1.39 ± 0.02
2.5	1.532 ± 0.002	1.553 ± 0.003	1.602 ± 0.004	1.56 ± 0.04
5.0	1.693 ± 0.003	1.602 ± 0.003	1.619 ± 0.003	1.64 ± 0.05
10.0	1.716 ± 0.003	1.635 ± 0.002	1.650 ± 0.003	1.67 ± 0.04
15.0	1.536 ± 0.003	1.511 ± 0.004	1.497 ± 0.005	1.51 ± 0.02
20.0	1.484 ± 0.004	1.430 ± 0.005	1.490 ± 0.004	1.47 ± 0.03
30.0	1.260 ± 0.004	1.199 ± 0.002	1.229 ± 0.003	1.23 ± 0.03
40.0	1.027 ± 0.004	1.032 ± 0.002	1.058 ± 0.003	1.04 ± 0.02
Total				-25% ± 2%
<i>Lizardite (Vis/NIR)</i>				
0	0.073 ± 0.008	0.076 ± 0.010	0.082 ± 0.006	0.077 ± 0.005
2.5	0.075 ± 0.011	0.075 ± 0.007	0.090 ± 0.008	0.080 ± 0.009
5.0	0.085 ± 0.010	0.087 ± 0.010	0.096 ± 0.009	0.089 ± 0.006
10.0	0.123 ± 0.010	0.112 ± 0.007	0.098 ± 0.006	0.111 ± 0.013

Table A.1—Continued

Irradiation Time (min)	Sample 1 %/μm	Sample 2 %/μm	Sample 3 %/μm	Mean %/μm
15.0	0.137 ± 0.009	0.106 ± 0.008	0.115 ± 0.008	0.119 ± 0.016
20.0	0.154 ± 0.013	0.114 ± 0.008	0.125 ± 0.005	0.131 ± 0.021
30.0	0.199 ± 0.011	0.142 ± 0.011	0.136 ± 0.006	0.159 ± 0.035
40.0	0.177 ± 0.009	0.151 ± 0.008	0.142 ± 0.008	0.157 ± 0.018
Total				103% ± 35%
50.0	0.220 ± 0.009	0.175 ± 0.009	0.137 ± 0.007	0.177 ± 0.042
60.0	0.211 ± 0.009	0.190 ± 0.007	0.155 ± 0.008	0.185 ± 0.028
Total				141% ± 50%
<i>Lizardite (NIR)</i>				
0	-0.149 ± 0.008	-0.140 ± 0.009	-0.122 ± 0.005	-0.137 ± 0.014
2.5	-0.147 ± 0.007	-0.142 ± 0.006	-0.128 ± 0.005	-0.139 ± 0.010
5.0	-0.145 ± 0.009	-0.137 ± 0.009	-0.120 ± 0.006	-0.134 ± 0.013
10.0	-0.140 ± 0.009	-0.135 ± 0.007	-0.117 ± 0.005	-0.131 ± 0.012
15.0	-0.139 ± 0.006	-0.141 ± 0.006	-0.117 ± 0.006	-0.132 ± 0.013
20.0	-0.141 ± 0.012	-0.119 ± 0.006	-0.110 ± 0.006	-0.123 ± 0.016
30.0	-0.145 ± 0.009	-0.137 ± 0.008	-0.102 ± 0.004	-0.128 ± 0.023
40.0	-0.149 ± 0.008	-0.110 ± 0.006	-0.097 ± 0.005	-0.119 ± 0.027
Total				13% ± 12%
50	-0.150 ± 0.009	-0.102 ± 0.008	-0.103 ± 0.006	-0.118 ± 0.027
60	-0.134 ± 0.007	-0.100 ± 0.008	-0.095 ± 0.006	-0.110 ± 0.021
Total				20% ± 9%
<i>Olivine (Vis/NIR)</i>				
0	0.069 ± 0.006	0.072 ± 0.008	0.068 ± 0.009	0.070 ± 0.002
2.5	0.128 ± 0.007	0.126 ± 0.005	0.132 ± 0.005	0.129 ± 0.003
5.0	0.183 ± 0.008	0.178 ± 0.009	0.171 ± 0.005	0.177 ± 0.006

Table A.1—Continued

Irradiation Time (min)	Sample 1 %/μm	Sample 2 %/μm	Sample 3 %/μm	Mean %/μm
10.0	0.299 ± 0.006	0.278 ± 0.008	0.278 ± 0.008	0.285 ± 0.012
15.0	0.405 ± 0.008	0.366 ± 0.004	0.365 ± 0.004	0.379 ± 0.023
20.0	0.528 ± 0.008	0.487 ± 0.006	0.475 ± 0.006	0.497 ± 0.028
30.0	0.734 ± 0.011	0.688 ± 0.004	0.641 ± 0.005	0.688 ± 0.047
40.0	0.910 ± 0.004	0.888 ± 0.005	0.880 ± 0.006	0.893 ± 0.016
Total				-1182% ± 44%
50.0	1.087 ± 0.004	1.055 ± 0.005	1.046 ± 0.007	1.063 ± 0.022
60.0	1.320 ± 0.004	1.228 ± 0.004	1.237 ± 0.004	1.262 ± 0.051
Total				-1713% ± 104%
<i>Olivine (NIR)</i>				
0	0.047 ± 0.005	0.042 ± 0.006	0.041 ± 0.008	0.043 ± 0.003
2.5	0.068 ± 0.007	0.066 ± 0.003	0.067 ± 0.004	0.067 ± 0.001
5.0	0.096 ± 0.006	0.091 ± 0.007	0.088 ± 0.006	0.092 ± 0.004
10.0	0.153 ± 0.007	0.143 ± 0.008	0.136 ± 0.005	0.144 ± 0.009
15.0	0.214 ± 0.007	0.189 ± 0.004	0.184 ± 0.004	0.196 ± 0.016
20.0	0.288 ± 0.008	0.258 ± 0.006	0.247 ± 0.005	0.264 ± 0.021
30.0	0.399 ± 0.008	0.386 ± 0.004	0.347 ± 0.005	0.377 ± 0.027
40.0	0.521 ± 0.005	0.513 ± 0.005	0.496 ± 0.005	0.510 ± 0.013
Total				-1080% ± 62%
50.0	0.674 ± 0.004	0.626 ± 0.004	0.629 ± 0.006	0.64 ± 0.027
60.0	0.850 ± 0.004	0.781 ± 0.003	0.775 ± 0.004	0.80 ± 0.042
Total				-1753% ± 41%

Note. — Measurements of the spectral slope in the visible and NIR for each mineral using continuum points described in the text. The total values represent the percentage change computed from initial (fresh) and final (40 or 60 minute) irradiation values.

Table A.2. Spectral Reflectance Measurements

Irradiation Time (min)	Sample 1 Reflectance	Sample 2 Reflectance	Sample 3 Reflectance	Mean
<i>Cronstedtite (0.6μm)</i>				
0	0.070 \pm 0.002	0.069 \pm 0.001	0.070 \pm 0.001	0.070 \pm 0.001
2.5	0.058 \pm 0.001	0.056 \pm 0.002	0.056 \pm 0.003	0.057 \pm 0.001
5.0	0.049 \pm 0.001	0.052 \pm 0.001	0.052 \pm 0.002	0.051 \pm 0.002
10.0	0.043 \pm 0.001	0.045 \pm 0.001	0.045 \pm 0.001	0.044 \pm 0.001
15.0	0.043 \pm 0.002	0.041 \pm 0.002	0.044 \pm 0.002	0.043 \pm 0.002
20.0	0.040 \pm 0.001	0.038 \pm 0.002	0.040 \pm 0.002	0.039 \pm 0.001
30.0	0.035 \pm 0.002	0.036 \pm 0.001	0.036 \pm 0.001	0.036 \pm 0.001
40.0	0.035 \pm 0.002	0.035 \pm 0.001	0.035 \pm 0.001	0.035 \pm 0.000
Total				50% \pm 0.4%
<i>Cronstedtite (0.75μm)</i>				
0	0.076 \pm 0.002	0.076 \pm 0.002	0.076 \pm 0.001	0.076 \pm 0.000
2.5	0.065 \pm 0.001	0.063 \pm 0.002	0.063 \pm 0.002	0.064 \pm 0.001
5.0	0.057 \pm 0.001	0.060 \pm 0.002	0.060 \pm 0.002	0.059 \pm 0.002
10.0	0.049 \pm 0.001	0.051 \pm 0.002	0.052 \pm 0.002	0.051 \pm 0.002
15.0	0.049 \pm 0.002	0.046 \pm 0.002	0.050 \pm 0.002	0.048 \pm 0.002
20.0	0.045 \pm 0.001	0.042 \pm 0.003	0.045 \pm 0.003	0.044 \pm 0.002
30.0	0.038 \pm 0.002	0.039 \pm 0.001	0.039 \pm 0.002	0.039 \pm 0.001
40.0	0.037 \pm 0.002	0.037 \pm 0.001	0.037 \pm 0.001	0.037 \pm 0.000
Total				51% \pm 0%
<i>Cronstedtite (1.9μm)</i>				
0	0.157 \pm 0.003	0.157 \pm 0.003	0.157 \pm 0.001	0.157 \pm 0.000
2.5	0.137 \pm 0.002	0.132 \pm 0.002	0.134 \pm 0.003	0.134 \pm 0.003
5.0	0.122 \pm 0.003	0.125 \pm 0.001	0.126 \pm 0.003	0.124 \pm 0.002
10.0	0.105 \pm 0.002	0.108 \pm 0.001	0.111 \pm 0.002	0.108 \pm 0.003

Table A.2—Continued

Irradiation Time (min)	Sample 1 Reflectance	Sample 2 Reflectance	Sample 3 Reflectance	Mean
15.0	0.101 ± 0.003	0.097 ± 0.003	0.103 ± 0.003	0.100 ± 0.003
20.0	0.092 ± 0.003	0.085 ± 0.005	0.092 ± 0.003	0.090 ± 0.004
30.0	0.073 ± 0.003	0.073 ± 0.002	0.075 ± 0.003	0.074 ± 0.001
40.0	0.066 ± 0.004	0.066 ± 0.001	0.066 ± 0.002	0.066 ± 0.000
Total				$58\% \pm 0\%$
<i>Cronstedtite (2.2μm)</i>				
0	0.196 ± 0.003	0.196 ± 0.003	0.195 ± 0.001	0.196 ± 0.001
2.5	0.176 ± 0.002	0.171 ± 0.003	0.173 ± 0.003	0.173 ± 0.003
5.0	0.160 ± 0.002	0.163 ± 0.002	0.164 ± 0.003	0.162 ± 0.002
10.0	0.141 ± 0.002	0.142 ± 0.002	0.146 ± 0.003	0.143 ± 0.003
15.0	0.134 ± 0.003	0.127 ± 0.004	0.134 ± 0.004	0.132 ± 0.004
20.0	0.123 ± 0.004	0.114 ± 0.004	0.122 ± 0.003	0.120 ± 0.005
30.0	0.098 ± 0.003	0.097 ± 0.002	0.099 ± 0.003	0.098 ± 0.001
40.0	0.087 ± 0.004	0.086 ± 0.002	0.087 ± 0.003	0.087 ± 0.001
Total				$56\% \pm 0.4\%$
<i>Lizardite (0.57μm)</i>				
0	0.722 ± 0.006	0.723 ± 0.008	0.714 ± 0.004	0.720 ± 0.005
2.5	0.721 ± 0.010	0.718 ± 0.006	0.705 ± 0.007	0.715 ± 0.009
5.0	0.703 ± 0.009	0.706 ± 0.008	0.700 ± 0.008	0.703 ± 0.003
10.0	0.682 ± 0.008	0.683 ± 0.005	0.691 ± 0.004	0.685 ± 0.005
15.0	0.668 ± 0.008	0.690 ± 0.007	0.681 ± 0.007	0.680 ± 0.011
20.0	0.651 ± 0.010	0.683 ± 0.007	0.675 ± 0.003	0.670 ± 0.017
30.0	0.615 ± 0.009	0.663 ± 0.008	0.663 ± 0.006	0.647 ± 0.028
40.0	0.637 ± 0.007	0.654 ± 0.006	0.658 ± 0.007	0.650 ± 0.011
Total				$10\% \pm 2\%$

Table A.2—Continued

Irradiation Time (min)	Sample 1 Reflectance	Sample 2 Reflectance	Sample 3 Reflectance	Mean
50.0	0.610 \pm 0.006	0.636 \pm 0.007	0.653 \pm 0.006	0.633 \pm 0.022
60.0	0.615 \pm 0.006	0.623 \pm 0.005	0.648 \pm 0.007	0.629 \pm 0.017
Total				13% \pm 3%
<i>Lizardite (1.71μm)</i>				
0	0.781 \pm 0.005	0.785 \pm 0.006	0.780 \pm 0.004	0.782 \pm 0.003
2.5	0.781 \pm 0.005	0.778 \pm 0.004	0.776 \pm 0.004	0.778 \pm 0.003
5.0	0.770 \pm 0.006	0.774 \pm 0.007	0.775 \pm 0.004	0.773 \pm 0.003
10.0	0.775 \pm 0.007	0.769 \pm 0.005	0.768 \pm 0.004	0.771 \pm 0.004
15.0	0.771 \pm 0.004	0.772 \pm 0.004	0.770 \pm 0.004	0.771 \pm 0.001
20.0	0.763 \pm 0.008	0.770 \pm 0.004	0.770 \pm 0.004	0.768 \pm 0.004
30.0	0.754 \pm 0.006	0.769 \pm 0.006	0.766 \pm 0.003	0.763 \pm 0.008
40.0	0.766 \pm 0.006	0.765 \pm 0.004	0.766 \pm 0.004	0.766 \pm 0.001
Total				2% \pm 0%
50.0	0.763 \pm 0.006	0.763 \pm 0.006	0.758 \pm 0.005	0.761 \pm 0.003
60.0	0.762 \pm 0.005	0.756 \pm 0.006	0.766 \pm 0.005	0.761 \pm 0.005
Total				3% \pm 1%
<i>Lizardite (2.07μm)</i>				
0	0.726 \pm 0.005	0.732 \pm 0.006	0.733 \pm 0.003	0.730 \pm 0.004
2.5	0.729 \pm 0.005	0.728 \pm 0.004	0.730 \pm 0.003	0.729 \pm 0.001
5.0	0.721 \pm 0.006	0.724 \pm 0.006	0.730 \pm 0.004	0.725 \pm 0.005
10.0	0.728 \pm 0.006	0.723 \pm 0.005	0.726 \pm 0.003	0.726 \pm 0.003
15.0	0.726 \pm 0.004	0.725 \pm 0.004	0.729 \pm 0.004	0.727 \pm 0.002
20.0	0.719 \pm 0.008	0.729 \pm 0.004	0.732 \pm 0.004	0.727 \pm 0.007
30.0	0.712 \pm 0.006	0.726 \pm 0.006	0.731 \pm 0.003	0.723 \pm 0.010
40.0	0.723 \pm 0.006	0.729 \pm 0.004	0.732 \pm 0.003	0.728 \pm 0.005

Table A.2—Continued

Irradiation Time (min)	Sample 1 Reflectance	Sample 2 Reflectance	Sample 3 Reflectance	Mean
Total				0% \pm 0%
50.0	0.721 \pm 0.006	0.730 \pm 0.005	0.722 \pm 0.004	0.724 \pm 0.005
60.0	0.723 \pm 0.005	0.724 \pm 0.006	0.734 \pm 0.004	0.727 \pm 0.006
Total				0% \pm 1%
<i>Lizardite (2.16μm)</i>				
0	0.731 \pm 0.006	0.737 \pm 0.006	0.739 \pm 0.003	0.736 \pm 0.004
2.5	0.731 \pm 0.005	0.730 \pm 0.005	0.734 \pm 0.003	0.732 \pm 0.002
5.0	0.722 \pm 0.007	0.727 \pm 0.006	0.735 \pm 0.004	0.728 \pm 0.007
10.0	0.730 \pm 0.006	0.725 \pm 0.005	0.730 \pm 0.003	0.728 \pm 0.003
15.0	0.728 \pm 0.004	0.726 \pm 0.005	0.733 \pm 0.004	0.729 \pm 0.004
20.0	0.720 \pm 0.009	0.731 \pm 0.005	0.735 \pm 0.004	0.729 \pm 0.008
30.0	0.712 \pm 0.007	0.726 \pm 0.006	0.735 \pm 0.003	0.724 \pm 0.012
40.0	0.722 \pm 0.005	0.731 \pm 0.005	0.736 \pm 0.003	0.730 \pm 0.007
Total				1% \pm 0%
50.0	0.720 \pm 0.007	0.732 \pm 0.005	0.727 \pm 0.004	0.726 \pm 0.006
60.0	0.724 \pm 0.005	0.726 \pm 0.006	0.738 \pm 0.004	0.729 \pm 0.008
Total				1% \pm 1%
<i>Olivine (0.7μm)</i>				
0.0	0.746 \pm 0.005	0.747 \pm 0.007	0.750 \pm 0.007	0.748 \pm 0.002
2.5	0.690 \pm 0.005	0.692 \pm 0.004	0.683 \pm 0.004	0.688 \pm 0.005
5.0	0.637 \pm 0.007	0.644 \pm 0.008	0.648 \pm 0.003	0.643 \pm 0.006
10.0	0.554 \pm 0.004	0.570 \pm 0.006	0.570 \pm 0.007	0.565 \pm 0.009
15.0	0.493 \pm 0.007	0.512 \pm 0.003	0.513 \pm 0.004	0.506 \pm 0.011
20.0	0.431 \pm 0.006	0.448 \pm 0.005	0.457 \pm 0.005	0.445 \pm 0.013
30.0	0.362 \pm 0.009	0.373 \pm 0.003	0.389 \pm 0.004	0.375 \pm 0.014

Table A.2—Continued

Irradiation Time (min)	Sample 1 Reflectance	Sample 2 Reflectance	Sample 3 Reflectance	Mean
40.0	0.309 ± 0.003	0.317 ± 0.003	0.318 ± 0.005	0.315 ± 0.005
Total				58% ± 1%
50.0	0.267 ± 0.002	0.274 ± 0.004	0.276 ± 0.005	0.272 ± 0.005
60.0	0.225 ± 0.002	0.242 ± 0.003	0.239 ± 0.003	0.235 ± 0.009
Total				69% ± 1%
<i>Olivine (1.6μm)</i>				
0.0	0.790 ± 0.004	0.794 ± 0.004	0.795 ± 0.006	0.793 ± 0.003
2.5	0.769 ± 0.004	0.769 ± 0.002	0.764 ± 0.003	0.767 ± 0.003
5.0	0.741 ± 0.005	0.746 ± 0.005	0.748 ± 0.003	0.745 ± 0.004
10.0	0.697 ± 0.004	0.707 ± 0.005	0.707 ± 0.004	0.704 ± 0.006
15.0	0.662 ± 0.005	0.672 ± 0.002	0.674 ± 0.003	0.669 ± 0.006
20.0	0.621 ± 0.006	0.631 ± 0.004	0.640 ± 0.004	0.631 ± 0.010
30.0	0.570 ± 0.007	0.579 ± 0.003	0.591 ± 0.003	0.580 ± 0.011
40.0	0.528 ± 0.003	0.536 ± 0.003	0.538 ± 0.004	0.534 ± 0.005
Total				33% ± 0%
50.0	0.491 ± 0.003	0.498 ± 0.003	0.501 ± 0.005	0.497 ± 0.005
60.0	0.451 ± 0.003	0.471 ± 0.003	0.467 ± 0.003	0.463 ± 0.011
Total				42% ± 1%
<i>Olivine (2.3μm)</i>				
0.0	0.818 ± 0.004	0.821 ± 0.004	0.819 ± 0.005	0.819 ± 0.002
2.5	0.803 ± 0.005	0.804 ± 0.002	0.799 ± 0.003	0.802 ± 0.003
5.0	0.784 ± 0.004	0.790 ± 0.004	0.789 ± 0.005	0.788 ± 0.003
10.0	0.754 ± 0.006	0.764 ± 0.006	0.761 ± 0.003	0.760 ± 0.005
15.0	0.731 ± 0.005	0.738 ± 0.003	0.737 ± 0.003	0.735 ± 0.004
20.0	0.699 ± 0.005	0.707 ± 0.004	0.713 ± 0.004	0.706 ± 0.007

Table A.2—Continued

Irradiation Time (min)	Sample 1 Reflectance	Sample 2 Reflectance	Sample 3 Reflectance	Mean
30.0	0.658 ± 0.004	0.671 ± 0.003	0.675 ± 0.003	0.668 ± 0.009
40.0	0.623 ± 0.004	0.637 ± 0.004	0.633 ± 0.003	0.631 ± 0.007
Total				$23\% \pm 1\%$
50.0	0.594 ± 0.003	0.602 ± 0.002	0.603 ± 0.004	0.600 ± 0.005
60.0	0.558 ± 0.003	0.583 ± 0.002	0.573 ± 0.002	0.571 ± 0.013
Total				$30\% \pm 1\%$

Note. — Total values represent percentage changes computed from initial (fresh) and final (40 or 60 minute) irradiation values.

Table A.3. Spectral Band Depth Measurements

Irradiation Time (min)	Sample 1 Band Depth	Sample 2 Band Depth	Sample 3 Band Depth	Mean
<i>Lizardite (0.75μm)</i>				
0.0	0.127 ± 0.004	0.125 ± 0.006	0.127 ± 0.005	0.126 ± 0.001
2.5	0.120 ± 0.008	0.122 ± 0.004	0.123 ± 0.006	0.122 ± 0.002
5.0	0.111 ± 0.008	0.116 ± 0.006	0.117 ± 0.006	0.115 ± 0.003
10.0	0.096 ± 0.007	0.102 ± 0.004	0.103 ± 0.004	0.100 ± 0.004
15.0	0.084 ± 0.006	0.091 ± 0.004	0.093 ± 0.006	0.089 ± 0.005
20.0	0.069 ± 0.009	0.084 ± 0.006	0.085 ± 0.004	0.079 ± 0.009
30.0	0.049 ± 0.008	0.064 ± 0.007	0.072 ± 0.005	0.062 ± 0.012
40.0	0.046 ± 0.005	0.058 ± 0.005	0.064 ± 0.006	0.056 ± 0.009
50.0	0.036 ± 0.005	0.048 ± 0.008	0.056 ± 0.004	0.047 ± 0.010
60.0	0.035 ± 0.006	0.038 ± 0.004	0.046 ± 0.005	0.040 ± 0.006
Total				$69\% \pm 4\%$
<i>Lizardite (0.9μm)</i>				
0.0	0.141 ± 0.004	0.140 ± 0.006	0.143 ± 0.005	0.141 ± 0.002
2.5	0.134 ± 0.007	0.137 ± 0.004	0.137 ± 0.005	0.136 ± 0.002
5.0	0.124 ± 0.006	0.130 ± 0.006	0.132 ± 0.006	0.129 ± 0.004
10.0	0.111 ± 0.007	0.117 ± 0.005	0.119 ± 0.003	0.116 ± 0.004
15.0	0.099 ± 0.005	0.107 ± 0.003	0.110 ± 0.006	0.105 ± 0.006
20.0	0.082 ± 0.008	0.099 ± 0.005	0.102 ± 0.003	0.094 ± 0.011
30.0	0.062 ± 0.006	0.081 ± 0.007	0.090 ± 0.004	0.078 ± 0.014
40.0	0.060 ± 0.005	0.075 ± 0.004	0.079 ± 0.004	0.071 ± 0.010
50.0	0.046 ± 0.004	0.066 ± 0.007	0.073 ± 0.004	0.062 ± 0.014
60.0	0.047 ± 0.005	0.057 ± 0.003	0.065 ± 0.005	0.056 ± 0.009
Total				$60\% \pm 6\%$
<i>Lizardite (1.1μm)</i>				

Table A.3—Continued

Irradiation Time (min)	Sample 1 Band Depth	Sample 2 Band Depth	Sample 3 Band Depth	Mean
0.0	0.147 \pm 0.004	0.146 \pm 0.006	0.149 \pm 0.004	0.147 \pm 0.002
2.5	0.142 \pm 0.006	0.143 \pm 0.003	0.144 \pm 0.005	0.143 \pm 0.001
5.0	0.133 \pm 0.005	0.139 \pm 0.006	0.138 \pm 0.006	0.137 \pm 0.003
10.0	0.122 \pm 0.007	0.125 \pm 0.004	0.129 \pm 0.003	0.125 \pm 0.004
15.0	0.112 \pm 0.004	0.117 \pm 0.003	0.121 \pm 0.006	0.117 \pm 0.005
20.0	0.099 \pm 0.008	0.110 \pm 0.005	0.114 \pm 0.003	0.108 \pm 0.008
30.0	0.081 \pm 0.006	0.095 \pm 0.007	0.103 \pm 0.004	0.093 \pm 0.011
40.0	0.078 \pm 0.006	0.091 \pm 0.003	0.094 \pm 0.004	0.088 \pm 0.009
50.0	0.065 \pm 0.004	0.084 \pm 0.007	0.088 \pm 0.004	0.079 \pm 0.012
60.0	0.066 \pm 0.005	0.075 \pm 0.004	0.082 \pm 0.005	0.074 \pm 0.008
Total				50% \pm 5%
<i>Lizardite (1.4μm)</i>				
0.0	0.358 \pm 0.004	0.355 \pm 0.004	0.357 \pm 0.003	0.357 \pm 0.002
2.5	0.353 \pm 0.005	0.356 \pm 0.004	0.356 \pm 0.004	0.355 \pm 0.002
5.0	0.346 \pm 0.005	0.349 \pm 0.004	0.350 \pm 0.004	0.348 \pm 0.002
10.0	0.341 \pm 0.005	0.343 \pm 0.003	0.338 \pm 0.003	0.341 \pm 0.003
15.0	0.334 \pm 0.004	0.330 \pm 0.002	0.333 \pm 0.004	0.332 \pm 0.002
20.0	0.325 \pm 0.006	0.323 \pm 0.004	0.326 \pm 0.003	0.325 \pm 0.002
30.0	0.312 \pm 0.005	0.310 \pm 0.005	0.313 \pm 0.003	0.312 \pm 0.002
40.0	0.306 \pm 0.005	0.300 \pm 0.003	0.301 \pm 0.003	0.302 \pm 0.003
50.0	0.296 \pm 0.003	0.291 \pm 0.005	0.293 \pm 0.004	0.293 \pm 0.003
60.0	0.290 \pm 0.004	0.283 \pm 0.003	0.286 \pm 0.004	0.286 \pm 0.004
Total				20% \pm 1%
<i>Olivine (1.05μm)</i>				
0.0	0.329 \pm 0.004	0.332 \pm 0.005	0.324 \pm 0.007	0.328 \pm 0.004

Table A.3—Continued

Irradiation Time (min)	Sample 1 Band Depth	Sample 2 Band Depth	Sample 3 Band Depth	Mean
2.5	0.318 ± 0.005	0.315 ± 0.003	0.310 ± 0.004	0.314 ± 0.004
5.0	0.299 ± 0.006	0.300 ± 0.009	0.293 ± 0.004	0.297 ± 0.004
10.0	0.274 ± 0.004	0.281 ± 0.005	0.270 ± 0.007	0.275 ± 0.006
15.0	0.248 ± 0.005	0.257 ± 0.002	0.252 ± 0.004	0.252 ± 0.005
20.0	0.237 ± 0.004	0.238 ± 0.004	0.238 ± 0.005	0.238 ± 0.001
30.0	0.208 ± 0.008	0.219 ± 0.003	0.211 ± 0.003	0.213 ± 0.006
40.0	0.194 ± 0.003	0.201 ± 0.003	0.199 ± 0.004	0.198 ± 0.004
50.0	0.180 ± 0.002	0.186 ± 0.003	0.184 ± 0.004	0.183 ± 0.003
60.0	0.171 ± 0.002	0.179 ± 0.002	0.178 ± 0.003	0.176 ± 0.004
Total				$46\% \pm 2\%$

Note. — Total values represent percentage changes computed from initial (fresh) and final (40 or 60 minute) irradiation values.